Fermilab Library
1160 0004134 7

Study of Weak Neutral and Charged Current Interactions in Deuterium

A Dissertation presented

by

Steven Eugene Sommars

to

The Graduate School

in partial fulfillment of the requirements

for the degree of

Doctor of Philosophy

in

Physics

State University of New York

at

Stony Brook

August, 1980

FCE
LAB
S

Abstract of the Dissertation

Study of Weak Neutral and Charged Current Interactions in Deuterium

by

Steven Eugene Sommars

Doctor of Philosophy

in

Physics

State University of New York at Stony Brook

1980

This thesis deals with the first analyses coming from a high energy neutrino-deuterium bubble chamber experiment. The Fermi National Accelerator Laboratory's 15 foot bubble chamber (with an external muon identifier) served as both target and detector. The ratio of the number of neutrino-neutron charged current events to the number of proton target interactions was found to be 1.92+/-0.17. A smaller sample of antineutrino induced events was used to measure the neutron to proton ratio, 0.65+/-0.09. These two results are compatible with the simple quark parton model.

FERMILAB
LIBRARY

Monte Carlo corrections were used to extract the Bjorken x distribution from data. The x distribution of neutrons was observed to be wider than that of protons as expected from electroproduction data. Bjorken y distributions from both targets were flat. Evidence of scaling violation was exhibited by the data.

Neutral current coupling constants were deduced by measuring the neutral to charged current cross section ratio in neutrino-neutron and neutrino proton collisions separately. The proton target ratio, 0.50+/-0.08, was consistent with previous results. Neutron target events gave a ratio of 0.21+/-0.03, the first measurement of that quantity. Neutral current coupling constants were deduced to be U_L^2 = 0.20 +/- 0.08, D_L^2 = 0.11 +/- 0.07, a result consistent with the Weinberg Salam model.

This is dedicated

to my

parents

who have always helped

and encouraged me

Table of Contents

	Abstract	iii
	Dedication Page	v
	Table of Contents	vi
	List of Figures	viii
	Acknowledgements	xii
I.	Introduction	1
I.1	Charged Currents and the Quark Parton Model	4
I.2	Neutral Currents	12
II.	Description of Experiment	16
II.1	Experimental Apparatus	16
II.2	Scan	20
II.3	Measurement	24
II.4	Software	26
II.5	Deuterium	27
II.6	Rescattering	29
II.7	Contamination of Proton Distributions	33
II.8	Experimental Cuts	34
III.	Charged Current Interactions	37
III.1	Kinematic Method of Selecting Charged Current Events	37
III.2	Ratio of Neutron to Proton Cross Sections	38
III.3	Uncorrected Distributions in Lepton Variables	42
III.4	Corrected x and y Distributions	45

IV.1 Neutral Currents 56

IV.2 Experimental Cuts for Neutral Current Analysis 56

IV.3 Neutral to Charged Current Cross Section Ratio 58

IV.3.1 Identification of Events 60

IV.3.2 Cut on P_t^H to Reduce Incoming Hadrons 63

IV.3.3 Electron Neutrino Background 64

IV.3.4 Experimental Cross Section Ratio 66

IV.4 Extracting of Neutral Current Coupling Constants 71

Tables 83

Appendix A. External Muon Identifier 87

A.1 Electronic Construction of Chambers 87

A.2 Calibration of MWPC locations 90

A.3 EMI Acceptance 91

A.4 Efficiency and Background in the EMI 93

A.5 Muon Selection Criteria 95

A.6 Internal Picket Fence 102

Appendix B. Monte Carlo 103

B.1 Beam, Outgoing Lepton and Target 104

B.2 Outgoing Hadrons 107

B.3 Resolution in Kinematical Variables 109

B.4 Comparison of Monte Carlo Features with Data 112

References 114

List of Figures

Fig.	Page	
1	118	Fermilab accelerator and neutrino beam line.
2	119	Neutrino event energy spectrum. The solid histogram is the spectrum observed from charged current data (Chapter 3), while the dots are Monte Carlo predictions.
3	120	Template used for selecting neutrino candidates. (i)Curvature template to determine whether a track is fast. (ii)Sixty degree template used to determine if a track is backward. (iii)Ninety degree template used to determine if a track is forward.
4	121	Momentum distribution of backward, stopping protons. The curve represents the expected distribution from the deuteron wave function.
5	122	Rescattering in deuterium as a function of total beam-nucleon cross section. The data proton and pion beam data are from Reference 14, while the box represents the rescattering fraction from the analysis (Reference 15) of a photon-deuterium experiment.
6	123	Definition of P_{tr}.
7	124	P_{tr} distribution for (i) neutrino charged current interactions, (ii)neutral current interactions, and (iii) antineutrino charged current interactions as predicted by the Monte Carlo. Here H represents the vector sum of all particles other than the negative track with the highest transverse momentum. In (i), P_{tr} extends to much larger values than (ii) or (iii).
8a	125	Distribution in the Bjorken x variable from neutron and from proton target events (uncorrected), for events with P_{tr}>1.0 GeV/c and Evis > 10 GeV.
8b	126	The data of Figure 8a are shown again, but the proton distribution is normalized to the area of the neutron distribution.

9 127 Distribution in the Bjorken y variable from neutron and from proton target events (uncorrected), for the same data sample as Figure 8.

10 128 Average ν as a function of neutrino energy, for the same data sample as Figure 8. The lines represent the predictions of the Field-Feynman and Buras-Gaemers structure functions.

11 129, 130 a) Q^2 and b) W distributions, for the data sample of Figure 8. The peaks in the W distributions are due to quasielastic reactions $\nu n \rightarrow \mu^- p$, and $\nu p \rightarrow \mu^- \Delta^{++}$. The shaded region contains those events where the missing transverse momentum is less than 200 MeV/c.

12 131 Energy distribution of events coming from $\nu n \rightarrow \mu^- p$. The curve is the neutrino energy spectrum.

13 132 Kinematically allowed region after making Q^2, W cuts. A line is drawn at E_ν=100 GeV since few neutrino events have a higher energy.

14 133 Delta x, error in estimatation of Bjorken x, from Monte Carlo.

15 134 Differential correction curve for Bjorken x distribution. This particular curve is for the set of cuts: Evis>10 GeV, P_{tr}> 1 GeV/c, Q^2>1.5 $(GeV/c)^2$, W>1.5 GeV/c^2, x>0.05, y<0.90.

16 135 Differential correction curve for the Bjorken y distribution. This curve is for the same cuts as the previous figure.

17 136 Corrected distributions in the Bjorken x variable for deep inelastic neutrino interactions. The data is subject to the cuts of Figure 15. The curves are predictions from the quark parton model. The solid curve comes from using the Field-Feynman parameterizations, the dashed curve comes from using Buras-Gaemers.

18 137 Corrected distributions in x. The data of the previous figure are replotted to show that the neutron (solid line) distribution is wider than the proton (dashed line) distribution.

19 138 The Monte Carlo prediction of Figure 17 (Buras + Gaemers), is reploted to show sea and valence quark contributions separately.

20 139 Corrected x distributions for two different neutrino energy ranges. The data is subject to the cuts of Figure 15.

21 140 Corrected distributions in the Bjorken y variable for deep inelastic neutrino interactions. The data is subject to the cuts of Figure 15.

22 141 Transverse momentum of the visible hadrons (P_t^H) in typical neutral and charged current events. P_{tr} can be seen to be typically large in charged current events and much smaller in neutral current events. The total visible momentum P_t transverse to the neutrino direction is also shown.

23 142 P_{tr} distribution for deuterium target events. Only the cuts of Chapter 2 are applied to the data.

24 143 Apparent neutral to charged current cross section ratios as a function of P_t^H cut for deuterium target events.

25 144 P_{tr} distribution after making P_t^H cut for deuterium target events.

26 145 P_{tr} distribution after making P_t^H cut for neutron target events.

27 146 P_{tr} distribution after making P_t^H cut for proton target events.

28 147 u_L^2 vs d_L^2 as determined in this experiment. Also shown in the prediction of the Weinberg-Salam model.

29 148 Bubble chamber and external muon identifier.

30 149 Sketch of the internal construction of a single EMI proportional wire chamber.

31 150-153 EMI acceptance vs a)momentum, b)Bjorken x, c)Bjorken y, d)P_{tr}. In each figure, the upper solid line is the first plane acceptance while the lower dotted line is the geometrical acceptance for the combined two planes.

32 154 IPF efficiency versus charged multiplicity of the charged current event.

33 155 Definition of variables used in neutrino energy estimate.

34 156 Resolution in neutrino energy, E_ν(calc.)/E_ν(gen.).

35 157 Distribution of longitudinal momentum of the outgoing hadrons in charged current interactions. The variable z= (energy of individual hadron)/(total hadronic energy) is used. The solid curve represents the z distribution predicted by the Monte Carlo.

36 158 Distribution of transverse momentum of individual hadrons with respect to the total hadronic direction for charged current interactions. The solid curve is the distribution generated by the Monte Carlo program.

Acknowledgements

I would like to express my appreciation to Professor Roderich Engelmann for being my advisor. He has helped me throughout all stages of my work in high energy physics.

Dr. Tomas Kafka has contributed much to this experiment through his thorough analysis and useful suggestions. I thank Dr. James Hanlon for showing me many of the tricks of the trade, and especially for his assistance in early stages of the analysis.

To all other members of the E545 collaboration at Illinois Institute of Technology, the University of Maryland, Tohoku University, and Tufts University I express my appreciation for the good communication and cooperation which are so necessary in a large group.

At Fermilab, there are several people who I would like to thank: Dr. James Wolfson, who served as liason physicist, Chuck Mangene, who kept the Lab A Mezzanine working, Gordon Koizumi and the other neutrino crew chiefs, Wes Smart and George Mullholland and the crew of the 15' bubble chamber, and the accelerator and support staff at Fermilab who made my stay both enjoyable and profitable.

I acknowledge the work of the Berkeley-Hawaii collaboration for building the external muon identifier and express my thanks for their help in making it useful in our experiment.

At Stony Brook, I want to thank our scanning staff whose rapid and careful work made my task much easier: Russ Maier, Mike Marcinak, Liz Palmer, Chris Remek, Jean Vergopia, Lucretia Winters, and also to Roy Small who kept our scanning and measuring equipment operational. I appreciate the speed with which Chuck Wrigley and Venke Ganapathi drafted the figures.

The staff of the Stony Brook computer center has been very friendly and helpful during all the time I spent processing and analyzing data.

Professors Robert Shrock and Jack Smith gave valuable assistance through several discussions.

Finally, I would like to thank my wife, Arlene, for all the encouragement she has given me and for being so patient and understanding.

I. Introduction

The existence of the neutrino was inferred in the 1930's from studies of nuclear beta decay; undetected light particles were necessary for energy and momentum to be conserved. It was not until 1959 that Reines and Cowan (Reference 1) first detected such particles by investigating interactions of antineutrinos emerging from a nuclear reactor with a target consisting of cadmium chloride and water.

There are three broad classes of neutrino interactions with matter:

purely leptonic	$\nu e \rightarrow \nu e$
semi-leptonic elastic	$\nu p \rightarrow \nu p$
semi-leptonic inelastic	$\nu p \rightarrow$ anything except νp

In purely leptonic events, neutrinos interact only with other leptons, such as electrons or muons. Semi-leptonic elastic events [illegible] neutrinos interacting with non-leptons elastically, which

means that the same particles exit the reaction that entered it. Only the third type, semi-leptonic inelastic, is dealt with here.

The first high energy neutrino reactions studied were those of the charged current variety:

$$\nu + \text{target} \rightarrow \mu^- + \text{anything}$$

"Charged current" refers to the exchange of charge between the incoming lepton (ν) and the outgoing lepton (μ).

In 1967, Weinberg and Salam (Reference 2) predicted that another type of neutrino interaction existed. This-as of then unseen-reaction had no charge exchanged between incoming and outgoing leptons, so it was called a weak neutral current:

$$\nu + \text{target} \rightarrow \nu + \text{anything}.$$

In 1973, the first examples of weak neutral current events were found in experiments at Cern and Fermilab (Reference 3).

The neutrino is the only known particle which undergoes exclusively weak interactions. By studying inelastic neutrino-nucleon charged current collisions, details of the internal nucleon structure are probed. In addition to what is already known, with the measurement of weak neutral-current interactions, constraints on the form of the weak force and its unification with the well understood electromagnetic interaction are developed. This experiment, Fermilab E545, was the first done at high energies in which neutrino-proton and neutrino-neutron collsions could be analyzed simultaneously and separately. Previous work has been on either a hydrogen target or on a target composed of complex nuclei which made separation of neutron and proton target events difficult.

This thesis deals with the weak charged current as a tool to study details of nucleon structure when interpreted through the quark-parton model. In addition, the less understood weak neutral current is investigated. Properties of hadrons produced in neutrino-deuterium interactions are subject of a separate investigation.

I.1 Charged Current Interactions and the Quark Parton Model

The general form of the differential cross section for neutrino-nucleon collision, assuming a vector-axial vector (V-A) form for the weak current, is:

$$\frac{d^2\sigma}{dxdy} = G_F^{\,2}\frac{ME}{\pi}\nu\left[(1-y)F_2+\frac{y^2}{2}2xF_1+y(1-y)xF_3\right] \qquad (1.1)$$

If the interaction is symbolically represented by:

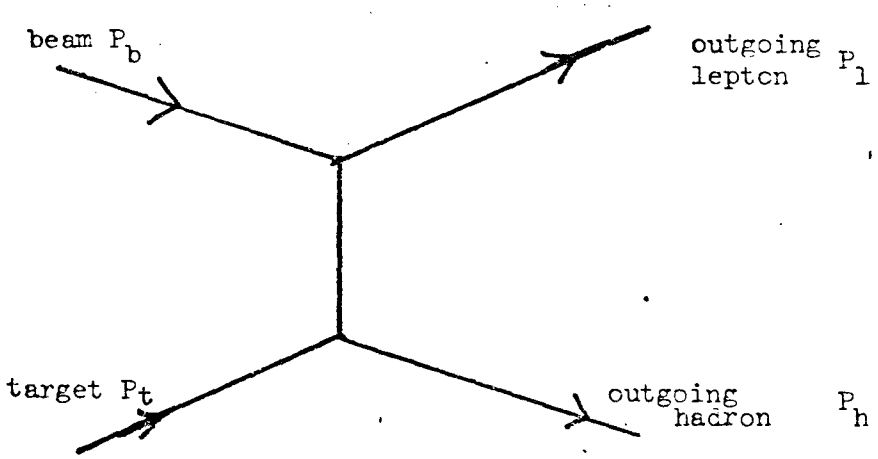

then the variables are defined as:

G_F = Fermi coupling constant

M = nucleon mass

E_ν = energy of the incoming neutrino

Q^2 = four-momentum transfer between incoming and outgoing lepton$=(P_b-P_l)^2$

ν = energy transfer between incoming and outgoing lepton$=E_b-E_l=E_h-E_t$

y = fraction of energy transferred from incoming to outgoing lepton$=(1-E_l/E_b)$

$x = Q/2M\nu$

F_1, F_2, F_3 are functions of Q^2 and ν only. The assumption is made that the outgoing lepton has negligible mass.

Bjorken predicted (Reference 5) that, at high energies, the unknown functions F_1, F_2 and F_3 would depend not on ν and Q^2 separately, but on the dimensionless ratio x. This may be thought of as the lack of a mass scale when the neutrino interacts with a pointlike target. "Bjorken scaling" also implies that the total neutrino-nucleon cross section is a linear function of E_ν. At extremely high energies, that dependence must fail because the

total cross section cannot exceed the bound set by unitarity. The hypothesized intermediate vector boson $W^{\pm}$ would not provide a mechanism for this limit to be followed, without cancellations from higher order interactions such as are implied by the renormalizable theory of quantum chromodynamics (QCD). For this experiment, however, the effects of an intermediate vector boson with the expected mass of about 70 GeV/c^2 are negligible.

A source of deviation from Bjorken scaling could be gluon bremsstrahlung as predicted by QCD. Previous neutrino experiments have seen evidence for nonscaling (Reference 6), but these effects were not large and are neglected for most of the analysis presented here.

If the neutrino scatters from an object of spin 1/2 at rest, the Callan-Gross relation (Reference 4) holds:

$$2xF_1 = F_2 \tag{1.2}$$

This analysis assumes the validity of (1.2).

For a charged lepton scattering from a nucleon, which is due primarily to electromagnetic interactions, the general form of the deep inelastic cross section is given by:

$$\frac{d^2\sigma}{dxdy} = \frac{4\pi\alpha^2}{Q^4} 2ME \left[(1-y)F_2 + \frac{y^2}{2} 2xF_1 \right] \tag{1.3}$$

The form of this cross section is very similar to that for the case of neutrino scattering. Since parity is conserved in electromagnetic interactions, there are two structure functions instead of three as in the neutrino case. If the Callan-Gross relation holds, the two unknown functions are reduced to one. There are two separate probes to study the nucleon structure, charged leptons and neutrinos.

In the quark parton model (Reference 7), Feynman developed the description of nucleons consisting of pointlike objects called partons. The assumption is usually made that the partons are quarks and gluons. Only quarks (Reference 8) interact directly with neutrinos. A charged current reaction is described as a change of quark type. Nucleons are composed primarily of three valence quarks. Additionally, a varying number of sea quarks are present. The four types of quarks which are considered here are listed below along with their quantum numbers:

	Charge	Spin	Isospin	Charm	Strangeness
U (or Up)	2/3	1/2	1/2	0	0
D (or Down)	-1/3	1/2	-1/2	0	0
S (or Strange)	-1/3	1/2	0	0	-1
C (or Charmed)	2/3	1/2	0	1	0

In a neutron, the valence quarks are two D-quarks and one U-quark. A proton contains the opposite, one D-quark and two U-quarks.

Since the quarks confined within a nucleon, they are not at rest, but carry amounts of internal momentum which vary according to a probability distribution which is a function of the variable x. Now, x has a physical interpretation. In the very high momentum reference frame, which moves with large velocity with respect to the laboratory, where all partons travel in the same direction, x is interpreted to be the fraction of the nucleon momentum which the quark carries. The U-quark distribution function, u(x), is then the probability for finding an Up quark with a fractional momemtum x between x and x + dx. An SU(2) symmetry between protons and neutrons means that the quark

structure functions are related by the following isospin rotation:

Proton	Neutron
$u(x)$	$d(x)$
$d(x)$	$u(x)$
$s(x)$	$s(x)$
$c(x)$	$c(x)$

Similar relations hold for the antiquarks.

Rather than having a subscript representing proton or neutron, by convention, the structure function symbols used are those for a proton, and the SU(2) relations are invoked whenever neutron structure functions are used; thus, $d_n(x)=u_p(x)=u(x)$, etc. A subscript is used, however, to differentiate quarks from the sea from the valence quarks. To aid in distinguishing between symbols for quarks and their distribution functions, the quarks themselves are denoted by capital letters while lower case symbols are used for the structure functions. Quark structure function

symbols with no subscript represent the sum of sea and valence quarks:

$$u(x) = u_v(x) + u_s(x)$$

In the version of the quark parton model due to Glashow, Iliopoulous and Maiani (Reference 10), neutrinos couple to D, S, anti-U, and anti-C, while antineutrinos couple to anti-D, anti-S, U, and C. This is because in neutrino charged current interactions, one positive unit of charge is given up by the neutrino to a quark which changes from, for example, a D-quark with charge -1/3 to a U-quark with charge +2/3. A neutrino cannot interact with a U-quark since no charge +5/3 quark exists in the model.

Using the quark parton model, the unknown functions F_2 and F_3 can be expressed in terms of the quark structure functions. Setting the Cabbibo angle to zero (see Appendix B for the more general form), and neglecting the small amounts of strange and charmed quarks present in the sea, the resulting differential cross section for neutrino-proton scattering is:

$$\frac{d^2\sigma}{dxdy} = \frac{2G_F^2 xME_\nu}{\pi} \left[d(x) + (1-y)^2\bar{u}(x)\right] \tag{1.4}$$

And for charged lepton-proton scattering:

$$\frac{d^2\sigma}{dxdy} = \frac{8\pi\alpha^2 MEx}{Q^4} \left[\frac{1+(1-y)^2}{2}\right]\left[\frac{4}{9}(u+\bar{u}) + \frac{1}{9}(d+\bar{d})\right] \tag{1.5}$$

The fractions in equation (1.5) appear since the photon-quark coupling is proportional to the square of the quark charge. In equation (1.4), however, the coupling is the same for all quark types. The two reactions can be diagramatically represented:

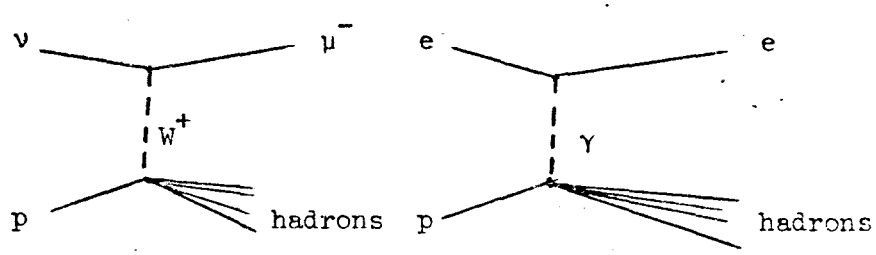

Parameterizations of the quark structure functions deduced from data on e+p and e+n deep inelastic scattering have been published (Reference 9). Using the quark parton model, these can be used to predict the shapes of differential neutrino-nucleon cross sections.

I.2 Neutral Currents

Neutral currents are a relatively new phenomenon. The theoretical understanding of the subject is not nearly as advanced as that for charged currents. Any analysis done now has a good deal of model dependence built into it since the experiments are very difficult. An incoming neutrino of poorly known energy interacts with a nucleon. There is an outgoing neutrino with unknown energy and direction. Furthermore, only some of the hadrons produced are detected.

The theory of Weinberg and Salam, based on the SU(2)xU(1) symmetry, which unifies theories of the weak and electromagnetic interactions, is a promising basis on which to interpret

experimental results. In this theory, there is an isotriplet and an isosinglet of vector bosons:

W^+, W°, W^- Isotriplet

B° Isosinglet

The two neutral bosons mix to form the physically observed particles:

$$\gamma = -\sin(\theta)W^\circ + \cos(\theta)B^\circ$$

$$Z^\circ = \cos(\theta)W^\circ + \sin(\theta)B^\circ$$

The charged W bosons mediate the weak charged current interaction, while the neutral γ is the ordinary photon which mediates the electromagnetic interaction. The Z° is a newly predicted particle, which is the intermediary of the weak neutral current that has been studied by experiments (Reference 3) in the last six years. An important feature of this model is that the quark struck by the Z° does not change its flavor in weak neutral current interactions. The coupling between the Z° and the struck

quark may depend upon quark type.

The neutral current differential cross section, omitting strange and charmed sea, can be written (Reference 36):

$$\frac{d^2\sigma}{dxdy} = \frac{2G_F^2 ME_\nu x}{\pi}\left\{\bar{u}_v\left[u_L^2+u_R^2(1-y)^2\right]+d_v\left[d_L^2+d_R^2(1-y)^2\right] + \left[u_s(u_L^2+u_R^2)+d_s(d_L^2+d_R^2)\right]\left[1+(1-y)^2\right]\right\} \quad (1.6)$$

The four coupling constants are related in this model by one free parameter, the Weinberg angle:

$$\begin{aligned} u_L^2 &= (1/2 - 2/3\sin^2\theta_W)^2 \\ d_L^2 &= (1/2 - 1/3\sin^2\theta_W)^2 \\ u_R^2 &= (2/3\sin^2\theta_W)^2 \\ d_R^2 &= (1/3\sin^2\theta_W)^2 \end{aligned} \quad (1.7)$$

Experimentally detecting a neutral current signal of known magnitude is difficult. In order to minimize experimental uncertainties, the common practice has been to measure ratios of

neutral to charged current cross sections. The Weinberg angle can be inferred from such a measurement. Since there are both proton and neutron targets in deuterium, two independent measurements of the cross section ratio can be made. The left handed coupling constants can be measured separately, without assuming a specific theory, and serve as a test of the Weinberg-Salam model.

II. Description of Experiment

II.1 Experimental Apparatus

This experiment was carried out at Fermi National Accelerator Laboratory in the fall of 1978. Five institutions cooperated in the data taking and analysis. There were experimenters from the State University of New York at Stony Brook, Illinois Institute of Technology, University of Maryland, Tohoku University and Tufts University.

The production of a beam of neutrinos and the detection of products of neutrino-deuterium interactions required the use of a large amount of apparatus.

Figure 1 shows the arrangement for the production of the neutrino beam. In the main ring, protons were accelerated to an energy of 350 GeV. Typically, 1.0×10^{13} protons were in the accelerator at this time. Over a one millisecond period, the protons were ejected from the ring and struck a target of beryllium oxide. Many secondary particles, including pions and kaons, were produced in that collsion. They were focused, that is, their angular divergence lessened, by means of a single magnetic horn (Reference 11) which was operated with a current of

5000 amps. All positively charged secondary particles were focused without momentum selection.

The unstable mesons passed through an evacuated pipe where some of them decayed into charged particles and neutrinos. At the end of the decay pipe, the remaining charged particles included a large number of undesired muons which were filtered out by means of a long mound of earth called a berm. Charged particles lost energy by passing through the dirt and were stopped there. The neutral neutrinos, with their very small interaction probability, passed through the berm unhindered and reached the bubble chamber. Approximately every seven seconds, the entire process, which produced a beam of neutrinos, was repeated.

The energy distribution of neutrinos interactions is shown in Figure 2. This spectrum represents a wide-band neutrino beam. Kinematically identified (Chapter 3.1) charged current events form the solid histogram. Monte Carlo predictions, shown as dots, and the energy distribution of quasielastic events (Chapter 3.2) are both consistent with the data. Due to the relative branching ratios for the meson decay, most of the beam was composed of muon neutrinos with about 1 percent coming from electron neutrinos. A more important contaminant to the beam came from the decay of negative pions and kaons which produce antineutrinos. The amount of this contaminant was found to be small, about 10 percent, and is used to measure a cross section ratio in Chapter 3.

In order to study interactions of the neutrino beam with matter, a large detector, the Fermilab 15' bubble chamber, was used. The chamber was filled with liquid deuterium, which had a negligible contamination of tritium to eliminate a cause of unacceptable bubbling.

In order to keep the deuterium liquid, it was kept at a temperature of about 30 degrees Kelvin and at a pressure of 80 psi.

This fill had a nuclear collision length of 3.2 meters, which meant that only a small fraction of the outgoing hadrons interacted in the bubble chamber. Muons could not be simply identified as particles that do not interact, as many hadrons also exit the bubble chamber without scattering.

The deuterium radiation length is long compared to a more dense bubble chamber liquid, about nine meters. Only about ten percent of the outgoing photons can therefore be detected. Photons come from the decay of neutral pions which represent about one third of the particles created in the neutrino interaction. A significant fraction of the hadronic energy was therefore not seen.

Pure deuterium has an equal number of neutrons and protons. There was, however, some contamination to the bubble chamber fill. A sample of the bubble chamber liquid, which was analyzed at Argonne National Laboratory, showed the main

components to be

H-H	2.1	molar-percent
H-D	1.5	molar-percent
D-D	96.4	molar-percent

Therefore, the fill contained 49.3 percent neutrons and 50.7 percent protons. This small difference is neglected.

The neutrino-deuterium interactions were recorded on photographic film in three views to allow for stereo reconstruction. Superconducting Helmholtz coils created a magnetic field of about 30 kG inside the chamber to make charged momentum determination possible. Approximately 328,000 triads were taken with a total number of protons on target of 4.9×10^{18}. This thesis is based on an analysis of one third of the total exposure and represents a flux of 1.57×10^{18} protons.

In order to aid in the identification of particles originating from neutrino-deuterium interactions, external electronic detectors were used. The external muon identifier (EMI) served to identify muons coming from charged current interactions. The detector consisted of two planes of multi-wire proportional chambers (MWPC). The first and second plane were

separated from the bubble chamber by 4 and 9 pion absorption lengths of zinc, concrete and lead. This device is described in greater detail in Appendix A. Another detector, the internal picket fence (IPF) was partially installed for the run. Some of its performance characteristics are given in Appendix A, but the device is not used in the present analysis.

II.2 Scan

Two independent visual scans of the film were made to locate and characterize the events. Scanning was done on tables which magnified the film images by a factor of 10. Locating neutrino interactions was difficult in this experiment since there were no beam tracks to follow. In addition, since the source of the wide-band neutrino beam was far from the deuterium, the events were located nearly uniformly throughout the bubble chamber. The entire picture had to be carefully scanned to locate candidate neutrino interactions.

Possible neutrino candidates were searched for by requiring that there were no charged incoming beam tracks, and that there were at least tracks of two charged secondary particles (prongs) emerging from the primary interaction. The presence of a charged incoming beam track was signaled by a track which had an angle of greater than 120 degrees with respect to the neutrino direction and which had a momentum greater than 1.5 GeV/c, both of which were determined at the time of the scan by using a template (Figure 3). All neutrino charged current interactions fit into the category of having at least two charged tracks. There is a loss of neutral current interactions with zero or one charged prong and a loss of antineutrino charged currents events with one charged prong.

Because there was a large flux of low energy neutral hadrons which decayed or interacted inside the bubble chamber, special rules were devised to eliminate such background events at scanning time. Two and three prong candidate neutrino events were required to have at least one of the following properties:

(a)A near kink (sudden change in track curvature) on one of the tracks

(b)An associated neutral particle

(c)One or more fast, forward tracks, where curvature is determined by means of a template (Figure 3). (Fast means momentum greater than 1.5 GeV/c and forward means having an angle of 90 degrees or less with respect to the neutrino beam.)

To eliminate high energy photons, two prong candidates had to have a non-zero opening angle between the two tracks. This caused a negligible loss of true neutrino interactions.

The efficiency for locating events was a function of topology, the number of charged tracks which were outgoing from the neutrino interaction. High multiplicity events were easy to locate while two prong events could be missed more easily. The efficiency to locate two and three prong events was 0.90 and 0.96 respectively, and 1.00 for more than three prongs. To account for this effect, multiplicity dependent weights were assigned to events used in the analysis.

Once the candidate event had been located, it was sketched on paper and additional information noted. Neutral strange particles and photons which were possibly associated with the interaction were searched for and recorded. The charged multiplicity was carefully studied since it is used to separate neutron and proton target events. Short stopping tracks are a signature of a spectator proton. Neutrino interactions which occurred upstream of the candidate event inside the bubble chamber and in the wall of the chamber were recorded. These 'wall-on' interactions represented a possible source of contaminating neutral hadrons. Candidate neutrino events are required, later in the analysis, not to point toward any upstream interaction.

Each prong was followed along its visible trail and its eventual fate recorded with a label. For this experiment, track labels were used for the following:

(a) Interacting tracks

(b) Electrons or positrons

(c) Kinks

(d) Pion decay

(e) Muon decay

(f) Stopping tracks

Due to the condiditions under which the bubble chamber operated, the size of bubbles was high. Identification of slow protons by their high ionization energy loss was difficult and in general, not done.

II.3 Measurement

All tracks were measured using a film plane digitization system. For measurement, a magnification of either 24 or 60 times the film size was used, depending upon the institution. In each of the three views, six fiducial points of known location inside the bubble chamber were measured to aid in track reconstruction. One of two methods was used so that the same track was identified in each view: (i)tracks were matched by measurers who noted the unique characteristics of each track in an event, or (ii)a computer program served to matching tracks. Little difference has been found in the results from the two methods, except for the highest multiplicity events, where matching by measurers was

superior.

The digitized points were reconstructed into momenta using the program TVGP, Three View Geometry Program, (Reference 13) as modified at Tohoku University. For an event to be successfully measured, all tracks were required to pass geometric reconstruction, or the entire event was remeasured. After repeated measurements, some tracks failed to reconstruct. In general the events with failed tracks tended to be events of higher multiplicity. A multiplicity dependent weight is assigned to each event to remove the bias.

There was an error on the measurement of momenta which is a function of both the momentum and length of the track. Generally the slower and longer a track was, the better its momentum measurement would be. These errors were small (See Section III.4) in comparision to the large error in the kinematic variables introduced by the poor knowledge of incoming neutrino energy.

II.4 Software

Tracks with momentum greater than 2 GeV/c were extrapolated to the EMI using the XTRAP and EMIKE programs written at the University of Hawaii and the University of California at Berkeley. A more strict cut on momentum is applied later in the analysis. Reference 41 contains a description of the software used in the EMI analysis.

Since many neutral secondary particles were not observed in this experiment, the energy of the incoming neutrino is not known, although its direction is well specified. Appendix B describes a Monte Carlo program which simulates this loss of information. Several methods of estimating the energy of the incoming neutrino in charged current interactions were investigated. The Bonn method (Reference 12) was chosen.

The analysis of charged current events requires the identification of outgoing muons, which can be done using the EMI or by kinematical methods. (The kinematic identification method is described in Chapter 3.)

II.5 Deuterium

The deuteron is the simplest nucleus which contains a neutron. The binding energy of the deuteron is only 2.2 MeV, which is a very small amount when compared to an incoming neutrino's energy. In the impulse approximation, the neutrino sees the deuteron as if it were composed of a neutron and a proton at rest with respect to each other and it interacts with one nucleon only. The non-participating nucleon, the 'spectator', flies off with its residual Fermi momentum.

In order to count the number of interactions on neutron and proton targets separately, several factors had to be taken into account. All events with an even number of charged prongs were taken to be neutron target events where the track of the spectator proton is too short to be seen. Because the range of a proton in deuterium is an increasing function of proton momentum, an slow spectator proton would be unseen. Some odd prong interactions also occured from neutron targets since sometimes the spectator protons had enough momentum to be seen in the bubble chamber. When the spectator proton moved toward the incoming neutrino direction, it could be easily located and identified: it appears as a short stub. A forward going spectator proton could

have been easily missed among other tracks, especially slow protons coming from the inelastic neutrino-neutron collision. To avoid this loss, forward spectator protons were not identified. Due to linearly varying cross section and to the Moeller flux factor, the number of forward and backward spectator protons is not the same. In its rest frame, a target which is moving towards the oncoming beam sees both the neutrino energy and the number of neutrinos passing by it per unit time increasing when compared to a target which is stationary in the laboratory. The backward moving spectator protons are assigned a weight:

$$\text{Weight} = 1 + \left(\frac{E_s - P_s \cos\theta_s}{E_s + P_s \cos\theta_s} \right)^2 \qquad (2.1)$$

Es and Ps are the energy and momentum of the spectator proton and

θ_s is its angle with respect to the neutrino direction.

This weight is only give to visible spectator protons with momentum greater than 140 MeV/c. The motivation for setting the cut can be seen in Figure 4. The solid histogram is the momentum spectrum of backward, stopping protons. From the Hulthen deuteron wave function, the curve, normalized to the total number of

neutron target events, represents the expected distribution. Stopping protons with momentum less than 100 MeV/c are short and therefore difficult to visually locate, especially in the 15' bubble chamber. Due to the weighting procedure described above, the results of this work have very little dependence on the exact value of the momentum cut, provided that it is greater than about 100 MeV/c.

II.6 Rescattering

In experiments with hadronic beams, the phenomenon of rescattering, or double scattering, from a deuterium target has been observed. A would-be spectator proton moves out of the spectator category by an interaction with the beam or target fragments. This causes a depletion of apparent neutron target events and a contamination of the proton target sample. Rescattering has been observed to be independent of the momentum of the incident beam particle, but varying with the total beam-nucleon cross section (Reference 14). It is assumed that

this rescattering does not influence the dynamics of the interaction nor appreciably change the kinematic variables of the outgoing lepton.

Rescattering also occurs from a spectator neutron, but that interaction would not change the visible charge of the event. It is assumed, however, that the probability for rescattering from a spectator neutron is the same as for a spectator proton.

If s is defined to be the fraction of events with a spectator proton (corrected for events with unidentified forward going spectator protons), and if d is the fraction of events in which double scattering occurred, then the observed number of neutron target events N_{nobs} is given by:

$$N_{nobs} = (1-d)\, N_n = s\, N \tag{2.2}$$

Here N is the total number of deuterium target events and N_n is the true number of events from a neutron target. Letting N_p be the true number of events from a proton target, this equation can be rewritten:

$$(1-d)/s = (N_p + N_n)/N_n \tag{2.3}$$

If r is the ratio (Chapter III) of the true number of events from neutron targets to the number of events from proton targets, it follows that:

$$r = s/(1-s-d) \tag{2.4}$$

Since a spectator could scatter from either beam or target fragments, it is reasonable to parameterize d as the sum of two terms: one of which does not depend upon the beam and one which is proportional to the beam-nucleon cross section, σ_t . This linear dependence can then be written:

$$d = a + b\ \sigma_t\ . \tag{2.5}$$

Available hadronic beam data (Reference 14) were analyzed to determine d at various values of beam-nucleon total cross section. These points were fitted with a least squares straight

line (Figure 5) and extrapolated to the neutrino-nucleon total cross section, which gave an estimate of the double scatter fraction:

$$d = 0.094 \pm 0.035 \tag{2.6}$$

In addition, an attempt (Reference 15) to determine d from a photon-deuterium experiment (Reference 16) was made. A complication arose in the analysis since a photon in a nucleus has hadronic characteristics. It was not clear how to define σ_t for the interaction, and even if it were, that cross section has not been measured. An effective total cross section of 10-17 mb was chosen for photon-deuterium. This region is plotted on Figure 5 and has a rescattering fraction consistent with the straight line extrapolation.

II.7 Contamination of Proton Distributions

Proton target distributions have an inherent contamination from neutron target events when extracted from deuterium targets. There are two sources for this contamination. First, if a spectator proton in a neutron target event rescatters, as mentioned in the previous section, that event has the topology of a proton target event. Second, if a spectator proton is faster than 140 MeV/c (which occurs in 6% of all neutron target events) and is in the forward hemisphere, it is not possible to distinguish it from protons which might have been produced by the inelastic collision.

These two sources combine to cause 15 percent of the neutron target events to end up in proton target distributions. This loss is unbiased in the kinematic variables, so the depletion in neutron distributions does not cause distortion of their shapes. Proton distributions have no loss, but they are contaminated. To correct for this, whenever a proton target distribution is made, 15 percent of the corresponding neutron target distribution is differentially subtracted.

II.8 Experimental Cuts

As a preliminary step in isolating a sample of neutrino interactions, preliminary cuts were applied to all events. No more than one track, in any single event, could fail to reconstruct. A TVGP failed track had either a poor momentum measurement, $\Delta p/p > 0.5$, or the reconstructed trajectory did not fit the measured points well, FRMS > 40. Because of the importance of charged current background in the neutral current analysis, only events which had no track failures were accepted for the determination of neutral current coupling constants.

The location of the vertex of the primary interaction was required to be inside a fiducial volume of 15.6 cubic meters. (In Section III.4, a smaller volume of 12.4 cubic meters is used to allow for better measurement of momentum.) The fiducial volume consisted of a sphere of radius 163 cm which had its top and bottom cut off by horizontal planes with a separation of 220 cm. This was designed to make most of the events visible in all three camera views. The mass of the deuterium, with density 0.14 gm/cubic centimeter, inside this region was 2.2 metric tons.

In order to eliminate low energy hadronic background, a cut was made on the visible longitudinal momentum, along the beam direction, at the primary vertex , called Evis. All events in this work have Evis greater than 5 GeV. This is more severe than the cut made by template at scanning time. Any event which was eliminated by using the template would also have been eliminated with the Evis cut at 5 GeV. A higher cut on Evis at 10 GeV is used for the charged current analysis.

Special cuts were made on two prong candidates to eliminate background from photon conversion and neutral particle decays: (i)All two prong events were required to have an opening angle in the laboratory of greater than one degree; and, (ii) the invariant mass of two prong events was required not to be that of a neutral kaon or lambda, within a window of +/- 10 MeV/c^2.

III. Charged Current Interactions

III.1 Kinematic Method of Selecting Charged Current Events

In the quark parton model, a neutrino interacts via charged currents only with negatively charged quarks or antiquarks. Neglecting sea quarks, the proton contains only one negatively charged quark, a D-quark, while the neutron has two D-quarks. Naively, in deuterium, the ratio of the number of events on neutron targets to the number of events which occured on proton targets would then be 2/1.

As a first step, a sample of charged current events must be defined. To obtain the largest possible sample, kinematically identified events are used. For this selection,the visible energy, Evis, is required to be greater than 10 GeV, which reduces the number of incoming low energy neutral hadrons. Experimental cuts described in Section II.8 were also applied.

The variable P_{tr} was chosen to aid in selecting charged current events; Figure 6 shows how it is defined. First, the negative track with the largest momentum transverse to the

neutrino direction is selected as the muon candidate, then all other tracks are added together to form a vector sum. P_{tr} is defined as that component of the selected negative track's momentum which is transverse to the direction of the vector sum. In neutrino charged current interactions, the outgoing muon usually has a large momentum transverse to the neutrino direction. P_{tr} is large since the other tracks tend to be on the opposite side of the neutrino axis from the muon. Various backgrounds, such as neutral current and antineutrino interactions illustrated in Figure 7, tend to have low values of P_{tr} because the algorithm selects an outgoing hadron which is not well separated (in transverse momentum) from the rest of the tracks in the event. To reduce contamination due to neutral hadrons and neutrino induced neutral current events, the variable P_{tr} is required to be larger than 1 GeV/c. In addition, this cut largely eliminates antineutrino neutral and charged current events. Any antineutrino charged current event which is detected by the EMI is explicity discarded from the neutrino charged current sample.

The kinematic event selection chooses the correct track as the muon in over 99 percent of the events. Monte Carlo predictions and EMI analysis confirm this.

By Monte Carlo estimate, there is a small residual contamination of the data from events other than neutrino charged current interactions. The background is estimated to consist of

three percent neutral current interactions and one percent antineutrino interactions. Total contamination, including interactions from incoming neutral hadrons, is estimated to be five percent.

III.2 Ratio of Neutron to Proton Cross Sections

Part of the data is not in the deep inelastic kinematic region where equation (1.4) is expected to be valid. But, for a quick look at the neutron-proton comparison, this detail is neglected. In Section III.4 where differential distributions are investigated, more stringent cuts are applied to assure that the data is in the deep inelastic region.

The experimental result is just the ratio of the number of events from neutron to the number of events from proton targets. A total of 3581 (3277 before processing weights) events are in the data sample. The overall ratio does not depend upon the resolution of kinematic variables since the result is an inclusive one, integrated over all values of Bjorken x,y and neutrino energy. The value obtained in this experiment is then:

$$R(n/p) = 1.92 \pm 0.17 \ (\pm 0.22 \text{ systematic}) \qquad (3.1)$$

This is the first measurement of R at high energy from a deuterium target. The estimated systematic error exists due to the uncertainty in the rescattering fraction.

There were also several measurements of R at low energy:

Ratio	Target	Neutrino Energy			
1.95 +/- 0.21	Deuterium	1.5-6	GeV	ANL	Ref. 17
1.48 +/- 0.17	Deuterium	< 10	GeV	BNL	Ref. 18
		(no rescattering correction)			
2.08 +/- 0.15	Propane-freon	1-10	GeV	GGM	Ref. 19

In addition, there was a measurement at high energy from a track sensitive target (TST) which used a bubble chamber containing hydrogen in one section and neon in another. The neutron to proton cross section ratio was extracted by comparing the number of events in the two regions. The result from that experiment was:

1.94 +/- 0.35	H2-Neon	TST	> 6	GeV	BEBC	Ref. 20

Since there are sea quarks in the nucleons, the neutron to proton ratio is expected to deviate from 2.00. If the number of sea quarks in the neutron and proton are similar, the cross section ratio would become less than 2.00 .

The quark structure functions, including contributions from the quark sea, have been parameterized (Reference 9) using data obtained by scattering charged leptons from nucleons. The functions, as given by Field and Feynman, depend on x only. The ratio using that parameterization and equation 1.4 is predicted to be 1.88.

Buras and Gaemers incorporated violation of scaling into their functions, so that the quark structure functions depend upon both x and Q^2. Integrating the functions given in their paper over the observed energy spectrum gives a cross section ratio of 1.75.

The neutron to proton cross section ratio was studied as a function of energy, using the Bonn method (Reference 12) to estimate the neutrino energy. No statistically significant variation of the neutron to proton cross section ratio as a function of neutrino energy is observed. Even though the Buras and Gaemers cross sections change with energy, the energy

dependence for both targets is similar and cancels to a large degree when taking the neutron to proton ratio. The ratio measured in this experiment, therefore, cannot distinguish between the scaling and non-scaling parameterizations.

The EMI has a good acceptance for the outgoing muon from antineutrino charged current events. A sample of 269 (131 without processing and EMI weights) events is identified as coming from antineutrino interactions using this detector. Kinematic identification of antineutrino charged current events would be plagued by background from the much more numerous neutrino interactions. From this sample, the neutron to proton cross section ratio is found to be:

$$R(n/p)(\text{antineutrino}) = 0.65 \pm 0.09 \qquad (3.2)$$

Here, the dominant error is statistical since the sample is small. An error in the EMI efficiency (Appendix A) would cancel in this ratio. The systematic error is estimated to be +/- 0.04. This is just the result expected from the quark parton model since the antineutrino interacts (via charged currents) with U-quarks instead of D-quarks. Neutrons have one U-quark, while protons have two, the ratio should then be roughly 1/2.

III.3 Uncorrected Distributions in Lepton Variables

For the first time at high energies, the differential distribution of the lepton variables in neutrino-neutron and neutrino-proton interactions can be shown separately. The distributions are shown first without any corrections for experimental resolution and losses. In the next section, the x and y distributions are unfolded.

The data sample for this section is exactly the same as for the cross section ratio analysis. Illustrating gross features of the data does not require the imposition of more severe cuts.

Differential distributions, as opposed to overall results like the ratio of numbers of neutron and proton target events, require that each neutrino interaction be assigned a value of the kinematic variables. In order to evaluate the Bjorken x and y variables (see Section I.2), the energy of the incoming neutrino is needed. Since the uncharged neutrino leaves no trail in the bubble chamber, its momentum cannot be measured directly. Because some of the particles which are products of the neutrino-nucleon collision escape detection, the energies of the secondary particles cannot be simply added. An estimate of the neutrino energy can be made, however, by using the fact that all outgoing hadrons in neutrino-nucleon collisions tend to exit the

interaction in nearly the same direction. The Bonn method (Reference 12 and Appendix B) is one algorithm for making this estimate.

Figure 8a shows the distribution of events in the Bjorken x variable. As expected from electroproduction data, the x distribution in the neutron is wider than that in the proton. This is seen more clearly in Figure 8b in which the proton and neutron distributions are normalized to the same area.

Figure 9 shows that the y distribution is essentially flat in both neutron and proton target events. This is expected if the neutrino interacts primarily with quarks rather than antiquarks. The sharp dropoff at high y is a distortion in the distribution due to the P_{tr} cut imposed on the data.

To check for possible violations of scaling, the average value of v, which is $x*y$, as a function of neutrino energy is plotted in Figure 10. As equation B.9 shows, this variable is independent of the neutrino energy. The two curves are the predictions of the parameterizations (Reference 9) by Field and Feynman (scaling) and of Buras and Gaemers (non scaling). Experimental resolution and the effects of cuts on the data have been incorporated into the curves. As the highest energy data points show, the non scaling model is in better agreement with the data. Most of the events however, are in the low energy region (for example, 70 percent are below 50 GeV) where both

parameterizations give adequate agreement with the data. Violation of Bjorken scaling is not a serious complication in the unfolding of the x and y distributions from the raw data.

Figure 11 shows the distributions in the four momentum transfer squared, Q^2, and in the invariant mass of the final hadronic state W. The W distribution for neutrons has a peak at the mass of the neutron (.938 GeV/c^2). This is due to the quasielastic interaction:

$$\nu n \rightarrow \mu^- p \tag{3.3}$$

Proton target events have a peak in the W distribution at a mass of 1.23 GeV/c^2 due to the reaction:

$$\nu p \rightarrow \mu^- \Delta^{++} \tag{3.4}$$

(To show the existence of the peaks more clearly, the shaded region contains those events where the missing transverse momentum is less than 200 MeV/c. Quasielastic events should satisfy this requirement since they lack outgoing neutrals.) Above an energy

of a few GeV, the cross sections for these exclusive reactions have been found (Reference 21) to be independent of energy. The events which came from reaction (3.3) are plotted in four energy bins in Figure 12. This quasielastic signal has low background, but only 65 events. On the figure, the modified (see appendix B) neutrino energy spectrum is seen to be consistent with the distribution of quasielastic events. The data and the neutrino spectrum are normalized at the 20-30 GeV energy bin. It should be noted that this figure is different in shape from Figure 2 in that this represents the number of incident neutrinos at a given energy, while Figure 2 represents the number of neutrino events at a particular energy.

III.4 Corrected x and y Distributions

Contamination of the data by non-charged current interactions has already been highly reduced by cuts on P_{tr} and Evis. In order to examine the x and y distributions in the deep inelastic region, additional restrictions must be applied to the data.

The peaks at low masses in the W distributions are due to quasielastic interactions in which the neutrino interacts with the nucleon, rather than with the individual quarks. To make sure that this analysis is probing the constituents of the nucleons, a cut on W is necessary. Therefore, the minimum value of W accepted is:

$$W > 1.5 \text{ GeV}/c^2 \tag{3.5}$$

Electroproduction data (Reference 22) showed that the structure functions were dependent on x only, not on x and Q^2 separately, for Q^2 above 1-2 $(\text{GeV}/c)^2$. For this analysis, the Q^2 cut is selected to be:

$$Q^2 > 1.5 \ (\text{GeV}/c)^2 \tag{3.6}$$

Of the set Q^2, W, x, y, E_ν, only three are independent variables. By making the cuts on Q^2 and W, the x and y distributions are distorted. Q^2 and W can be expressed in terms of x, y, E_ν:

$$Q^2 = 2MxyE_\nu \qquad (3.7)$$
$$W^2 = M^2 + 2ME_\nu y(1-x)$$

Thus, the cut on Q^2 causes a preferential loss of events at low x and y. Low y and high x events are lost by the W cut.

The shape of the kinematically allowed region of the x, Q^2 plane is illustrated in Figure 13. Of the three boundaries shown, two of them, the $W = 1.5$ GeV/c^2 and the $Q^2 = 1.5$ $(\text{GeV}/c)^2$, come directly from equation (3.7). At 100 GeV, there is an effective E_ν boundary since above that value, very few neutrino events are observed. There are a negligible number of events with $Q^2 > 100$ $(\text{GeV}/c)^2$, in fact, most of neutrino interactions have $Q^2 < 30$ $(\text{GeV}/c)^2$.

Since the muon identification efficiency is poor for slow muons, an explicit cut is made on the range of y used:

$$y < 0.9 \qquad (3.8)$$

If kinematic muon selection is used, there is a larger chance to misidentify the outgoing muon for low x. Also as Figure 13 shows, the lowest x values are not accessible. An explicit cut in x is

used:

$$x > 0.05 \tag{3.9}$$

A study was made of the effects of poor momentum measurement on differential distributions. The momentum direction is a well measured quantity, but its magnitude has an error associated with it. In general, the greater the distance that a track is visible in the bubble chamber, the better determined its momentum will be. Momentum error is larger for fast tracks, but since the neutrino energy spectrum is concentrated at low energies, below 50 GeV, most tracks are slow. In charged current events, the fastest tracks tend to be the outgoing muons. To investigate the effect of measurement on the muon tracks, the Monte Carlo was employed using the method of Reference 23 to simulate measurement errors. This technique, which parameterizes the momentum error as a function of length and momentum, was used in an antineutrino-proton experiment in the same bubble chamber with almost identical optical characteristics. By reducing the fiducial volume (Section II.8) in the front half of the bubble chamber, the minimal path length for momentum measurement is increased. With the original 15.6 cubic meter volume, 16% of the

muons had a momentum measurement error greater than 20%. Increasing the minimum path length to 60cm, from the original 30cm, reduced the number of muons with measurement error above 20% by half. This 60cm path length, corresponding to a smaller fiducial volume of 12.4 cubic meters, is a value which was used in a previous experiment (Reference 24) in the 15' bubble chamber. An indication that this reduction decreased distortions in the y distributions was observed. With the original fiducial volume, the low y region, where the muons are fastest, was depleted more than was expected from the effects of the Q^2 and W cuts. Increasing the minimum path length to 60cm, or greater, removed this effect. Here, the 12.4 cubic meter fiducial volume is used to minimize distortion of experimental distributions. No explicit correction is made for any residual measurement errors.

After making all cuts, the data sample, consisting of 2550 events (2318 before processing weights), is biased. To correct for the distortion of distributions by cuts and to correct for the effects of the poor knowledge of neutrino energy, Monte Carlo (Appendix B) calculations are performed. Events were generated according to equation 1.4. Experimental cuts are made on these simulated events and a correction factor defined:

Correction = Observed distribution/Generated distribution

This correction is calculated bin by bin for each distribution.

Quark structure functions from Buras and Gaemers serve as input to the Monte Carlo program. To observe how sensitive the correction factors were to the input parameterizations, Field and Feynman quark functions were also used and a correction calculated. A difference of less than two percent (over most of the x range) in the corrected distributions resulted from the change of input structure functions.

Generally, the more severe the W and Q^2 cuts applied to the data were, the larger the corrections became. For these cuts, the distortions in the distributions are almost entirely due to the cuts alone, the smearing in kinematic variables from the neutrino energy estimate leads to only small corrections. The resolution in x is +/- 0.03 within this sample, as is shown in Figure 14.

Because of the statistical nature of the corrections, differential distributions require the Monte Carlo generation of a large number of neutrino interactions. Computer overhead, however, restricts the generation of an arbitrarily large number of events. To smooth out the scatter of values due to the limited number of events used in the Monte Carlo calculation, the

corrections are parameterized by a fourth degree polynomial in x or y.

Figures 15 and 16 show the correction curves for the Bjorken x and y distributions. Since no attempt is made in this work to determine absolute normalizations of structure functions, the verticle scales of the curves are not important. Only the shape matters. The same correction curve is used for neutron and proton target events.

The dominating error in the corrected distributions is due to the lack of statistics. Since the neutrino energy spectrum is fairly well known, uncertainties in it should not cause a large contribution to the systematic error in the correction factors. As a check of this, the correction factors were calculated with a modified neutrino energy spectrum. For this test, the original Mori spectrum (Reference 43, also see Appendix B.) was used instead of the experimentally observed flux. This substitution is characteristic of the degree of uncertainty in the spectrum. In comparing the two correction curves from the experimental and test neutrino energy spectrums, the corrections changed typically 3 percent. The largest modification, 5 percent, occured at low x where the corrections are most severe.

The neutrino energy estimate and measurement error smears the distributions by moving an event from its true x or y to a nearby value. For x less than 0.7, this causes less than a ten

percent distortion which is small compared to the total correction. Above x = 0.7, the distortion becomes more severe, but there is little data in that region.

Some events in the data include tracks which were unmeasureable. Results, obtained from a data sample which specifically excluded such events, did not differ from the distributions given below.

Figure 17 shows the corrected distributions in the Bjorken x variable. Curves from the Field + Feynman and Buras + Gaemers parametrizations of electroproduction data are both consistent with this data. The partons seen by virtual photons seem to be the same as those probed by the W boson. In Figure 18, the corrected distributions for the two curves are shown together, with total areas normalized. As observed in the previous section, the x distribution in the neutron is wider than that of the proton.

At large values of x, near x=1, there are several explanations (Reference 25) for the neutron and proton x distributions to have different shapes. Since this analysis is not sensitive to the large x region, an explanation for the difference in shapes for medium x is desired. One possibility (Reference 26), is that some fraction of the time a nucleon consists of a quark + diquark (a bound state of a U- and D-quark) combination. In such a model, the internal momentum of a nucleon

would be shared equally by the quark and diquark. The diquark constituents would each carry only half the momentum that the unbound quark carried, in other words, they are on the average at lower x. Since a neutrino interacts with the neutron's unbound D-quark (high <x>) or bound D-quark (low <x>), while the proton is only a bound D-quark (low <x>), the x distribution in the neutron should be wider than that of the proton.

The corrected x distribution is the sum of contributions from sea and valence quarks. In this experiment, the sea contribution cannot be determined separately. As an illustration of the shapes of the two components of the distribution, Figure 19 shows the Buras + Gaemers prediction (as in Figure 17) for the neutron's x distribution broken up into sea and valence contributions. Valence D-quarks dominate the x distribution, especially at high x.

The neutron to proton cross section ratio for the corrected distributions should be close to the value obtained in Section III.2. Below x = 0.05, the structure functions are not determined. A rough estimate is made that the value for the missing bin is equal to the value of the second bin of x, from 0.05 to 0.10. The ratio obtained by this method is:

$$R(n/p) = 1.97 \pm 0.20 \quad (\pm 0.22 \text{ systematic}) \qquad (3.10)$$

The systematic error coming from the correction factors should largely cancel in this ratio, but the systematic error coming from the estimated rescattering fraction is still present.

To examine possible changes in shape of distributions due to violation of Bjorken scaling, the corrected x distributions for two different neutrino energy ranges (above and below 40 GeV) are given in Figure 20. An average Q^2 of 6.8 $(GeV/c)^2$ and 21.0 $(GeV/c)^2$ is observed for the low and high energies respectively. Because the samples are small, only distributions from a deuterium target are shown. Corrections are calculated separately for the two histograms. The change of shape implies that nonscaling behavior exists in the data. As a more quantitative description of the amount of scaling violation observed, the average value of x is calculated, with statistical errors only, for the low and high energy distributions:

$$\langle x \rangle = .289 \pm 0.003 \quad \text{deuterium, for } E_\nu < 40 \text{ GeV} \qquad (3.11)$$

$$\langle x \rangle = .255 \pm 0.004 \quad \text{deuterium, for } E_\nu > 40 \text{ GeV}$$

This is consistent with the trend expected in the theory of QCD. When a quark is struck with a smaller probe (larger Q^2), it may be resolved into a quark and a gluon. This has the effect of

shifting the distribution to lower x.

Corrected Bjorken y distributions are given in Figure 21 for neutron and proton target events. As expected, the distributions are similar and approximately flat, except at the lower values of y, below y = 0.1, where there is a deviation. There are two possible reasons for this. First, the Q^2 and W cuts both deplete the region so that the number of passing events is small. The corresponding correction factors are large and hence less reliable than at larger values of y. Also, this is the region where radiative corrections may become important. Quantum electrodynamics (QED) describes this process where charged particles emit virtual photons thereby changing their momenta. Using the prescription found in Reference 27, radiative corrections are calculated and found to be small (less than 2-3 percent) for the y distribution, except for the lowest y bins where they become as large as 10 percent. Radiative processess would not distort the x distribution for x above 0.05.

IV.1 Neutral Currents

In a light liquid like deuterium, it is difficult to identify individual neutral current interactions. The number of neutral current events can, however, be measured with reasonable accuracy. Comparing the ratio of neutral current and charged current cross sections is one way of determining the strengths of the neutral current coupling constants. The Weinberg-Salam theory of weak interactions gives predictions for these constants. In the present Chapter, the method for measuring the ratio of cross sections is described and cuts on the data are discussed. The experimental ratio is used along with a Monte Carlo analysis to extract values of the coupling constants.

IV.2 Experimental Cuts for Neutral Current Analysis

It is desirable to measure the neutral current to charged current cross section ratio without applying any cuts to the data, but this is not possible. First, some neutral current events were

lost because they have fewer than two charged secondary tracks. (These events were not included in this analysis since they were extremely difficult to locate.) Also, there were incoming particles other than muon-neutrinos so that neutral hadrons and antineutrinos could have contaminated the data if no cuts were made.

In addition to eliminating events with zero or one charged secondary, a cut on the visible hadronic energy is made on the data sample used for this analysis, Evish has to be greater than 5 GeV. Incoming neutral hadrons were themselves products of neutrino interactions upstream of the bubble chamber. As such, they tended to have only a fraction of the energy of the neutrino which produced them. By making a cut on the visible hadronic energy, most of these slow contaminants are eliminated. A further cut is made on the total momentum of the visible hadrons transverse to the neutrino direction P_t^H. A reduction in the size of the charged current background and the contamination from incoming neutral hadrons is accomplished by this cut. Figure 22 illustrates the P_t^H variable in typical neutral and charged current events. The true P_t^H is, in general, nonzero for both types of events. If a charged current event is mistakenly called a neutral current event, the apparent P_t^H is then small and thus eliminated by the cut.

The momentum distribution of the incoming neutral hadrons is not well known. It would have been possible to use a Monte Carlo prediction for the momentum spectrum, but that would have had a large uncertainty in it. Instead, this analysis leaves the exact cut on P_t^H variable. When the P_t^H cut is high enough to eliminate the incoming hadrons, the neutral current to charged current cross section ratio should become independent of the P_t^H cut value. In addition, the value obtained in this experiment for the cross section ratio on deuterium is compared to the well-measured value on other isoscalar targets. This serves as a confirmation that the technique is valid.

IV.3 Measurment of Neutral to Charged Current Cross Section Ratios

In this section, the analysis is described for measuring the cross section ratio on a deuterium target, which fixes the values of the cuts used. The same technique is then used on neutron and proton targets separately.

Figure 23 shows the distribution of events in the variable P_{tr}. Also plotted on the histogram is the distribution of events which are identified by both planes of the EMI as charged current events, corrected for EMI inefficiency and acceptance. At low values of P_{tr}, these corrections become as large as a factor of three. The Monte Carlo prediction (dashed line) and the EMI measurement agree on the shape of the distribution for charged current events. The two plane EMI has a good acceptance for antineutrino charged current events since the outgoing muon is usually high in momentum. The antineutrino charged and neutral current component (see next section) is also illustrated in the figure. After subtracting the charged current and antineutrino signals from the total distribution, a neutral current signal of about 500 events is seen. This signal is almost totally in the first two bins of the histogram, below P_{tr}^2 of 2 $(GeV/c)^2$, as expected since the transverse momentum of the outgoing hadrons, with respect to the total hadronic vector, is known to be small from previous experiments (Reference 28). Since the negative track with the highest transverse momentum is just one of the hadrons, P_{tr} is small for neutral current events.

The neutral current signal is sitting on a rather sizeable background. To reduce the systematic error in extracting the neutral currents, a cut is made on P_t^H. In doing so, the P_{tr} distribution for charged current events is greatly suppressed at

low values of P_{tr} (See Figure 25). This reduction of background comes because a neutrino charged current event having a high P_t^H, tends to have a large P_{tr}. Even if they have a high P_t^H, neutral currents still occur mostly at low values of P_{tr}.

IV.3.1 Identification of Events

As can be seen from Figure 23, events with high values of P_{tr} are almost entirely charged currents, as expected from Monte Carlo analysis. By using this fact, the separation of neutral and charged current events is improved.

The charged current sample consists of the sum of three parts. First, all events with P_{tr}^2 greater that 5 $(GeV/c)^2$ are taken to be charged current. (This agrees with the EMI measurement as illustrated in Figure 23.) Second, charged current events with P_{tr}^2 less than 5$(GeV/c)^2$ and with muon momentum greater than 5 GeV/c are identified using the two plane EMI. (These are corrected for efficiency and for acceptance of the EMI.) Third, the remaining charged current events with muon momentum less than 5 GeV/c and with P_{tr}^2 less than 5 $(GeV/c)^2$ are

estimated by Monte Carlo. As can be seen in Table 1a, this is a small correction for the P_t^H cut used.

The raw neutral current sample consists of events with P_{tr}^2 less than 5 $(GeV/c)^2$ which are not identified by the EMI as either charged current neutrino or antineutrino events. The undetected neutrino charged current events are subtracted from the neutral current sample. Care must be taken to use the proper distributions in making corrections. A neutrino charged current event with low P_{tr} contributes to the neutral current background with kinematic variables P_t (total visible transverse momentum, see Figure 22) and Evis instead of just the momentum of the hadrons. The correction is made for muon momentum above 5 GeV/c by taking the identified charged current events, weighting by the known inefficiency and acceptance, and subtracting from the raw neutral current sample. A Monte Carlo estimate of the charged current background with muon momentum below 5 GeV/c is used to subtract those charged current events which the EMI could not detect.

Background from antineutrino charged current events is handled in the same manner as neutrino charged current events, but antineutrino neutral currents are indistinguishable from neutrino neutral currents. The observed number of antineutrino charged current events is used, along with the ratio of antineutrino neutral current to charged current cross section ratios, to

estimate the number of antineutrino neutral current events which must be subtracted from the raw neutrino neutral current sample. For isoscalar targets, the antineutrino neutral to charged current cross section ratio is well known (Reference 30):

0.380 +/- 0.014

When making the antineutrino neutral current subtraction on neutron and proton targets separately, the predictions of the Weinberg-Salam model are used for the antineutrino neutral to charged current cross section ratios:

0.45 for a neutron target

0.29 for a proton target

These predictions are consistent with the isoscalar value quoted above. The antineutrino neutral current subtractions are small, so the result of this analysis is not sensitive to the exact values of the above constants.

IV.3.2 Cut on P_t^H to Reduce Incoming Hadrons

No correction is made on the raw neutral current sample due to incoming neutral hadrons because this flux is not well known. Instead, the minimum value of P_t^H used in this analysis is high enough to reduce the incoming hadron fraction to a negligible amount. Figure 24 shows the ratio of neutral current to charged current cross sections as a function of this cut. The ratio decreases until the minimum P_t^H reaches 1.75 GeV/c. The flattening of the ratio above this point agrees with the hypothesis that neutral hadrons are primarily in the neutrino direction with low values of momentum transverse to the neutrino direction. Presently, it is felt that the incoming neutral hadrons do not contribute a significant background for P_t^H greater than 1.75 GeV/c. A further indication that the background is small comes from the observation that the cross section ratio for high P_t^H cuts agrees with the world average on other isoscalar targets (see IV.3.4).

The idea to use the cut on P_t^H to reduce hadron background has been checked using a sample of measured neutral strange particles. Their angular distribution is peaked in the forward direction and at low momentum. Using the geometry of the bubble chamber and upstream absorbers, an upper limit for hadron

background of 5 per cent on the final neutral current sample is estimated for the cuts given above.

IV.3.3 Electron Neutrino Background

The identification efficiency for outgoing electrons is poor in this experiment. An estimate on the possible background due to incoming electron neutrinos and electron antineutrinos needs be made. To do this, it is assumed that the kinematics of the muon neutrino and electron neutrino induced events are the same. This should be true at the high energies of this experiment where the mass of the outgoing lepton is negligible.

Neglecting the difference in neutrino energy spectrums, electron neutrino charged current events should populate the P_{tr} plot with the same distribution as muon neutrino charged current events. Similarly, the electron neutrino neutral current events fall mostly into the low P_{tr} bin. Since the flux (Reference 31) of electron neutrinos is estimated to be one percent of the flux of muon neutrinos, the background is small. Furthermore, if it is assumed that the ratio of neutral to charged current cross

sections is independent of whether the incoming neutrino is a muon or an electron neutrino, the method described here gives the correct result for any small electron neutrino background. This is because in the cross section ratio, both the numerator and denominator contain the same fraction of electron neutrino interactions.

Electron antineutrino neutral and charged current interactions are at an even smaller rate since their flux is less than that for muon neutrinos by a factor of 500. The electron antineutrino charged and neutral currents are negligible.

There is a very preliminary indication (Reference 32) which shows that the electron neutrino and antineutrino flux may differ from that calculated in Reference 31. The model is that some charmed F mesons are produced inside the beryllium oxide target and the hadronic beam dump (at the end of the decay pipe) and decay soon afterward with some number of electron neutrinos being produced. The estimated rates for this process is small enough that it does not influence the results given in this work.

IV.3.4 Experimental Cross Section Ratios

Table 1a gives the numbers of events which enter into the calculation of the cross section ratio. The charged current denominator has small corrections attached to it and the dependence on the EMI and on Monte Carlo calculations is not significant. Statistics dominate the error on this number. Figure 25 graphically shows how well the neutral and charged currents are separated. The kinematically identified and the EMI identified charged current distribution agree well.

The neutral current numerator has larger corrections attached to it, but they are much smaller than would be necessary without the cut on P_t^H (Figure 23). There is, of course, a price which is paid. The number of neutral current events is reduced from about 500 events to less than half that amount. But, the reduction of systematic errors is adequate compensation. In the shaded areas of Figure 25, it is shown that the corrections are much smaller than in the analysis without a P_t^H cut.

The result from this experiment for the ratio of neutral to charged current cross section ratios with the experimental cuts described above is then:

$$R_d = 0.29 +/- 0.03 \tag{4.1}$$

The error here is dominated by statistics. The systematic error is estimated to be +/- 0.01. This value can be compared with the world average (Reference 30) for the cross section ratio on isoscalar targets:

$$R = 0.301 +/- 0.007 \text{ (isoscalar targets)} .$$

The agreement is a confirmation of the validity of this method used in the calculation.

The analysis is then repeated for neutron and proton targets separately. Figures 26 and 27 illustrate the separation of neutral currents from charged currents for neutron and proton targets respectively. Tables 1b and 1c list the number of events in each category. For the cross section ratio on proton targets, the result is:

$$R_p = 0.50 +/- 0.08 \tag{4.2}$$

The neutral to charged current cross section ratio has been measured before in two previous proton target experiments:

$$R_p = 0.48 +/- 0.17 \quad \text{Reference 33 (Evish > 10 GeV)} \qquad (4.3)$$

$$R_p = 0.51 +/- 0.04 \quad \text{Reference 34 (Evish > 5 GeV, } P_t^H > 1.5 \text{ GeV/c)}.$$

All three experiments are consistent. The ratio is then calculated on neutron target events:

$$R_n = 0.21 +/- 0.03 \qquad (4.4)$$

This is the first measurement of the cross section ratio on neutron targets. The fact that the ratios are measured for both proton and neutron targets in a single experiment aids in reducing systematic errors for extracting the neutral current coupling constants which is done in the next section.

As was done for charged currents in Chapter III, it is possible to measure the neutral current neutron to neutral current proton cross section ratios. (This is the ratio of the number of corrected events from each target.) The neutron to proton cross section ratio for neutral currents measured in this experiment is:

$$R(n/p \text{ neutral current}) = 1.02 \pm 0.19 \tag{4.5}$$

The systematic error from the uncertainty in rescattering is +/- 0.07. The dominant error is statistical since there are only about 100 neutral current events from each target.

There has been a previous measurement of this ratio in a neutrino-neon experiment (Reference 35):

$$R(n/p \text{ neutral current}) = 1.27 \pm 0.36 \tag{4.6}$$

Counting the number of events from neutron and proton targets separately in neon is very difficult and was done by a statistical method. The two experiments are consistent.

Four ratios have now been measured: neutral current to charged current ratios for both neutron and proton targets, and neutron to proton ratios for neutral and charged current events. If the same data sample with the sample kinematic cuts were used to determine all four numbers, then they would not be experimentally independent. Only three of the four would be independent, the fourth ratio could be obtained from the other three. For example if the neutron to proton neutral current cross section ratio is divided by the neutron to proton charged current cross section ratio, that should be the same as if the neutral current to charged current cross section ratio for the neutron was divided by the neutral current to charged current cross section ratio for the proton. In actuality, neutral and charged currents are treated somewhat differently. The cut on P_t^H preferentially selects events at large x for the neutral current analysis. Ideally, one would do the analysis without this cut, or correct for the effects of the cuts. In the following section, the equivalent is done in order to extract the neutral current coupling constants.

IV.4 Extracting of Neutral Current Coupling Constants

Within the quark parton model the differential cross section for neutrino proton neutral current interactions can be written as:

$$\frac{d^2\sigma}{dxdy} = u_L^{\,2}\frac{d^2\sigma_1}{dxdy} + d_L^{\,2}\frac{d^2\sigma_2}{dxdy} + u_R^{\,2}\frac{d^2\sigma_3}{dxdy} + d_R^{\,2}\frac{d^2\sigma_4}{dxdy} \tag{4.7}$$

where

$$\begin{aligned}
\frac{d^2\sigma_1}{dxdy} &= \left(\frac{2G_F^{\,2}MEx}{\pi}\right)\left[u_v + (u_s+c_s)(1+(1-y)^2)\right] \\
\frac{d^2\sigma_2}{dxdy} &= \left(\quad '' \quad\right)\left[d_v + (d_s+s_s)(1+(1-y)^2)\right] \\
\frac{d^2\sigma_3}{dxdy} &= \left(\quad '' \quad\right)\left[u_v(1-y)^2 + (u_s+c_s)(1+(1-y)^2)\right] \\
\frac{d^2\sigma_4}{dxdy} &= \left(\quad '' \quad\right)\left[d_v(1-y)^2 + (d_s+s_s)(1+(1-y)^2)\right]
\end{aligned} \tag{4.8}$$

The u_L^2, d_L^2, u_R^2, and d_R^2 are the neutral current coupling constants in the notation of Sehgal (Reference 36). d_L^2 is the strength of the coupling between U or C quarks and the neutrino. u_L^2 gives the magnitude of the coupling between D or S quarks and the neutrino. If the interaction is of a pure V-A form, there should be only these left handed terms, u_R^2 and d_R^2 vanish. This more general formula (4.7) allows for right handed interactions. In Reference 36, a general expression for the neutral current Lagrangian is given:

$$\mathcal{L} = \frac{G_F}{\sqrt{2}} \overline{\psi}_\nu \gamma_\alpha (1+\gamma_5) \psi_\nu \left[\overline{\psi}_u \gamma_\alpha \left\{ u_L (1+\gamma_5) + u_R (1-\gamma_5) \right\} \psi_u + \overline{\psi}_d \gamma_\alpha \left\{ d_L (1+\gamma_5) + u_R (1-\gamma_5) \right\} \psi_u \right] \tag{4.9}$$

The charged current differential cross section for neutrino proton interactions is given in equation (B.1). The cross sections on a neutron target are obtained by an isospin rotation.

In the absence of any cuts, the ratio of the number of neutral current events to charged current events is given by the ratio of the integrals of the differential cross sections:

$$R_p = \frac{\int \frac{d^2\sigma nc}{dxdy}\, dxdy\, N(E_\nu)\, dE_\nu}{\int \frac{d^2\sigma cc}{dxdy}\, dxdy\, N(E_\nu)\, dE_\nu} \qquad (4.10)$$

$N(E_\nu)dE_\nu$ is the number of incoming neutrinos with energy betweeen E_ν and $E_\nu + dE_\nu$.

When experimental cuts are made, there are losses of both neutral and charged current events so that both the numerator and denominator are reduced. If $P_{nc}(x,y,E_\nu)$ is defined to be the fraction of neutral current events (at a particular neutrino energy and Bjorken x and y) which pass experimental cuts and if $P_{cc}(x,y,E_\nu)$ is defined similarly for charged current events, then the observed ratio of cross sections, including cuts, is given by:

$$R_p = \frac{\int \frac{d^2\sigma nc}{dxdy} P_{nc}(x,y,E_\nu)\, dxdy\, N(E_\nu) dE_\nu}{\int \frac{d^2\sigma cc}{dxdy} P_{cc}(x,y,E_\nu)\, dxdy\, N(E_\nu) dE_\nu} \tag{4.11}$$

In order to do this integration, a Monte Carlo technique is employed. In this method, the variables x, y and E_ν are thrown randomly according to:

x uniformly between 0 and 1

y uniformly between 0 and 1

E_ν with a probability proportional to $N(E_\nu)\, E_\nu$ (the event rate).

For a particular Monte Carlo event, one calculates the kinematic variables and then determines whether or not it passes the experimental cuts. If the same number of neutral and charged current events are thrown, then the cross section ratio after cuts is given by:

$$R_p = \frac{\sum_{\substack{\text{passing}\\ \text{events}}} \frac{1}{E_\nu}\left(u_L^2 \frac{d^2\sigma_1}{dxdy} + d_L^2 \frac{d^2\sigma_2}{dxdy} + u_R^2 \frac{d^2\sigma_3}{dxdy} + d_R^2 \frac{d^2\sigma_4}{dxdy}\right)}{\sum_{\substack{\text{passing}\\ \text{events}}} \frac{1}{E_\nu} \frac{d^2\sigma cc}{dxdy}} \qquad (4.12)$$

This can be written in terms of the coupling constants:

$$R_p = f_{1p}u_L^2 + f_{2p}d_L^2 + f_{3p}u_R^2 + f_{4p}d_R^2 \tag{4.13}$$

The f's are then numbers which are functions of the experimental cuts and which are calculated using the Monte Carlo. In their evaluation, the neutrino spectrum appears in both the numerator and denominator so that the overall magnitude cancels out and the detailed shape of the spectrum is not critical.

A point which may not be obvious is that the fraction of all of the neutral current events with zero and one charged outgoing track is important. Since the distribution of charged multiplicities is not well known in neutral current events, this introduces an uncertainty in the evaluation of the f's. An example is a good way to illustrate this point.

In this example, for calculating the f's for proton targets, the quark distributions are taken to be constant for simplicity. Assume that 1000 neutral current and 1000 charged current events are generated by the Monte Carlo. Take two different cases for the distribution in multiplicity:

		prongs=1	prongs>1	
Case 1:	Neutral currents	200	800	Before cuts
		0	600	After cuts
	Charged currents	-	1000	Before cuts
		-	900	After cuts
Case 2:	Neutral currents	40	960	Before cuts
		0	720	After cuts
	Charged currents	-	1000	Before cuts
		-	900	After cuts

In both cases, the charged currents are treated alike. Also the fraction of neutral currents which is lost in each category is taken to be the same, 100 percent of the one-prongs are lost and 75 percent of the three or more prongs are lost due to experimental cuts. The f's for this simplified example are just the ratio of the number of events passing cuts:

Case 1: $f = 600/900 = .67$

Case 2: f= 720/900 = .80

The example above is extreme. To obtain a more quantitative estimate of the uncertainty in 0 and 1-prong fractions, the Monte Carlo prediction was compared to charged current data. The 2-prong/even fraction from charged currents should be roughly the same as the 0-prong/even in neutral currents. Similarly, the 3-prong/odd fraction in charged currents should be comparable to the 1-prong/odd fraction in neutral currents. This comparison confirms the expectation that there are few 0 and 1-prong neutral current events. A systematic error of 5 percent is estimated in the f's due to the lack of precise knowledge of the fraction of events in the unseen topologies.

The parametrization of the quark structure functions used in this integration are primarily those of Buras and Gaemers (Reference 9). The quark sea is modified by making the overall strength of the strange sea equal to one half that of either u_s or d_s as suggested by dimuon data (Reference 37). The values for the f's with a cut on Evish of 5 GeV and a cut on P_t^H of 1.75 GeV/c are then:

	Neutron	Proton
f1=	0.47	1.91
f2=	1.02	0.96
f3=	0.16	0.60
f4=	0.34	0.35

(4.14)

The cut on P_t^H preferentially samples the large x part of the quark structure functions. The structure functions are not well known, especially at high values of x. This means that there is a systematic error associated with the evaluation of the f's. An uncertainty of ten percent is estimated on the numerical values of the f's which includes the estimated uncertainty on the number of unseen 0 and 1 prong events as discussed above.

Since this analysis is for incoming neutrinos, not antineutrinos, the ratio of cross sections is not very sensitive to the value of the right handed coupling constants. Using the ABCLOS (Reference 38) measurement of the right handed coupling constants:

$$u_R^2 + d_R^2 = .04 +/- .03 \qquad (4.15)$$

and the values for the f3, f4 given above, limits can be placed on

the size of the contribution from right handed couplings.

$$R_p^{rh} = .02 +/- .02 \qquad (4.16)$$
$$R_n^{rh} = .01 +/- .01$$

The experimental results are combined with the Monte Carlo calculation of the f's to form two equations:

$$R_p - R_p^{rh} = 0.48+/-.08 = 1.91\ u_L^2 + 0.96\ d_L^2 \qquad (4.17)$$
$$R_n - R_n^{rh} = 0.20+/-.03 = 0.47\ u_L^2 + 1.02\ d_L^2$$

These are equations for two straight lines, plotted in Figure 28. Also shown is a curve with the prediction of the Weinberg-Salam model. The Weinberg-Salam model has one free parameter, the Weinberg angle. In terms of this angle, the two coupling constants are given by:

$$u_L^2 = (1/2 - 2/3\ \sin^2\theta_W)^2 \qquad (4.18)$$
$$d_L^2 = (1/2 - 1/3\ \sin^2\theta_W)^2$$

As can be seen in the figure, the results of this experiment are consistent with the Weinberg-Salam model where the sine of the Weinberg angle is approximately 0.2 .

The equations 4.17 can be solved simultaneously to give a measurement of the coupling constants independent of a model. The results are:

$$u_L^2 = 0.20 \pm 0.08 \qquad (4.19)$$
$$d_L^2 = 0.11 \pm 0.07$$

Reference 34 reported results which were consistent with this experiment:

$$u_L^2 = 0.15 \pm 0.05 \quad \text{(Reference 34)} \qquad (4.20)$$
$$d_L^2 = 0.17 \pm 0.07$$

Table 1a

Neutral current analysis for $P_t^H > 1.75$ GeV/c, Evish > 5 GeV, deuterium target

Charged Current:

759	$P_{tr}^2 > 5\ (\mathrm{GeV/c})^2$
+10	EMI identified charged current
+ 5	Monte Carlo correction for charged current events with muon momentum below 5 GeV/c
---	
774	Number of charged current events

Neutral Current:

262	Raw neutral current signal
-23	EMI inefficiency and acceptance
- 5	Monte Carlo correction for charged current events with muon momentum below 5 GeV/c
- 8	Antineutrino neutral currents

226	Number of neutral current events

Table 1b

Neutral current analysis for $P_t^H > 1.75$ GeV/c, Evish > 5 GeV, neutron target

Charged Current:

541	$P_{tr}^2 > 5\ (\mathrm{GeV/c})^2$
+ 7	EMI identified charged current
+ 3	Monte Carlo correction for charged current events with muon momentum below 5 GeV/c
---	
551	Number of charged current events

Neutral Current:

135	Raw neutral current signal
-14	EMI inefficiency and acceptance
- 3	Monte Carlo correction for charged current events with muon momentum below 5 GeV/c
- 4	Antineutrino neutral currents

114	Number of neutral current events

Table 1c

Neutral current analysis for $P_t^H > 1.75$ GeV/c, Evish > 5 GeV, proton target

Charged Current:

218	$P_{tr}^2 > 5\ (\mathrm{GeV/c})^2$
+ 3	EMI identified charged current
+ 2	Monte Carlo correction for charged current events with muon momentum below 5 GeV/c
---	
223	Number of charged current events

Neutral Current:

127	Raw neutral current signal
- 9	EMI inefficiency and acceptance
- 2	Monte Carlo correction for charged current events with muon momentum below 5 GeV/c
- 4	Antineutrino neutral currents

112	Number of neutral current events

Table 2, Resolution in Kinematic Variables

Variable	Relative error	Rel. err.<0.25	Rel. err.<0.10
E_ν	0.15	0.85 percent	0.62 percent
Q^2	0.15	0.85 percent	0.62 percent
W	0.17	0.80 percent	0.49 percent
x	0.26	0.80 percent	0.57 percent
y	0.16	0.80 percent	0.55 percent
v	0.05	0.98 percent	0.89 percent

Relative error is < (delta variable)/(variable) >

A. External Muon Identifier and Internal Picket Fence

The External Muon Identifier (EMI) (Reference 39) consisted of 39 multiwire proportional chambers (MWPC) with delay line readout of coordinates. Each chamber had an active area of about one square meter, which was sensitive throughout the entire beam spill. There was no appreciable dead time that could cause failure to detect a muon. The EMI was configured in two planes with 21 chambers in the first plane and 18 chambers in the second plane. Figure 29 shows the location of the EMI and Internal Picket Fence (IPF) with respect to the bubble chamber. Between the bubble chamber liquid and the first plane of the EMI, there were approximately four interaction lengths of hadron absorber. The absorber was placed between the inner and outer walls of the bubble chamber. An additional five interaction lengths of absorber were located between the first and second EMI planes.

A.1 Electronic Construction of Chambers

A 28 MHz clock furnished the time base for the EMI. Signals from the delay lines were digitized with respect to that

standard. Using a PDP11 online computer and a CAMAC data buss, the digital times were stored on magnetic tape after each accelerator cycle. In the relatively long period between incoming neutrinos, the online computer program allowed gates to be active so that cosmic ray signals could be recorded from the MWPC's. This furnished a means of monitoring the performance of individual chambers throughout the experiment. To keep down noise and to maintain proper gain, voltages and discriminator settings were varied when necessary.

Figure 30 is a schematic diagram of the internal construction of a single MWPC. For economy, the MWPC's used four delay lines for each chamber instead of an amplifier for each wire. Most chambers, 21 out of 39, had nine amplifier outputs. The remaining 18 which were located away from the highest concentration of muons, were seven channel chambers. In addition to the delayed signals, there was an amplifier on the cathode return strip of one of the delay lines. This furnished a prompt signal, the undelayed time that the particle passed through. The nine channel chambers produced at most seven signals (the U channel was divided into two mutually exclusive sections) when a particle passed through the chamber. Since the seven channel chambers had one fewer amplifier for each U delay line, there

could be only six encodings at best.

The propagation velocity of a signal down a delay line was a function of the signal's position along the delay line. This dependence was approximately described by a quadratic function. Delay line velocities tended to be functions of time, temperature and other factors. The program CALB written by J. Marriner (Reference 40) was used to find velocity values for each delay line at regular intervals in the experiment.

To specify a signal's location, or hit, on a MWPC, three quantities were needed: two positions and a time. Since there may have been up to seven signals present, a constrained determination of the location was possible. By requiring a highly constrained location, very few false solutions are formed. Spurious solutions increased the background rate in the MWPC and made identification of muons more difficult, especially when using only the first plane of the EMI.

Unfortunately, by requiring a high constraint solution, the overall efficiency of the MWPC was decreased. Often one or more channels of a MWPC had a signal of insufficient amplitude to be distinguished from background noise. For different analyses, therefore, different minimum constraint classes are chosen.

A.2 Calibration of MWPC Locations

In using a hybrid electronic and photographic dectection system, it was important to be able to accurately connect particle trajectories from one medium to the other. The coarse locations of the MWPC's was known from previous experiments. An optical survey was made which verified the relative chamber to chamber position. At this point, the positions of the MWPC's were known in the bubble chamber coordinate system to within a systematic error of a few centimeters.

For the identification of muons in the presence of background hits in the MWPC's, the positional uncertainty had to be decreased to approximately one centimeter. This was done by using measured tracks. A sample of negative noninteracting through-going tracks was used to do this adjustment. They were withing 2.5 degrees of the beam direction and had a momentum of at least 10 GeV/c. As discussed in Reference 39, the sample was composed of approximately 99 percent muons. By matching the extrapolated bubble chamber trajectories to hits in the MWPC's, the positions of the individual chambers were adjusted for the best fit.

A.3 EMI Acceptance

The acceptance of the EMI for muons from neutrino charged-current events was far from complete. The primary deficiency was due to the inability of tracks which were slow or at wide angles to reach the EMI at all. This made the EMI unreliable below a momentum of about 3 GeV/c. Muons lose, on the average, 1.0 GeV/c and 1.5 GeV/c of momentum going through the first and second plane absorbers respectively. Coulomb multiple scattering of slow tracks leads to large uncertainty in extrapolation, the EMI is therefore not used for tracks slower than 4 GeV/c for the first plane and 5 GeV/c for the second plane.

Above these minimum momenta, the EMI acceptance was well behaved, but still not 100 percent. The acceptance versus momentum is shown in Figure 31a. This graph is an average over primary interaction locations throughout the bubble chamber and over the outgoing track's direction. Similarly, Figures 31b through 31d show the EMI acceptance versus Bjorken x and y, and versus the variable P_{tr} respectively. For convenience, the acceptance was parameterized as a function of two variables; momentum, and angle with respect to the beam direction. The acceptance for the first and second EMI planes is then given by:

Momentum range		First plane acceptance-Negative tracks (A.1)
5-10	(GeV/c)	$A = 1.00 + .18*\sin(\theta) - 2.53*\sin^2(\theta)$
10-20	(GeV/c)	$A = 1.00 + .05*\sin(\theta) - 1.40*\sin^2(\theta)$
over 20	(GeV/c)	$A = 1.00$

Momentum range		Second plane acceptance-Negative tracks
5-10	(GeV/c)	$A = 0.96 + .12*\sin(\theta) - 6.52*\sin^2(\theta)$
10-20	(GeV/c)	$A = 0.99 + .38*\sin(\theta) - 8.04*\sin^2(\theta)$
over 20	(GeV/c)	$A = 1.00$

Momentum range		Second plane acceptance-Positive tracks
5-7.5	(GeV/c)	$A = 0.69 - 1.01*\sin(\theta)$
7.5-10	(GeV/c)	$A = 0.92 - 1.66*\sin(\theta)$
10-15	(GeV/c)	$A = 0.99 - 1.22*\sin(\theta)$
15-20	(GeV/c)	$A = 1.00 - 0.63*\sin(\theta)$
over 20	(GeV/c)	$A = 1.00$

A.4 Efficiency and Background in the EMI

The efficiency of the EMI to detect a muon was not a simple number. If a muon passed through the EMI, the fraction of the time that a hit is recognized at analysis time depends upon the detail of the analysis. An example of this would be comparing the efficiencies for detecting a muon with one plane to detecting a muon with both planes. Obviously, a single plane is more efficient.

Estimates must be made of the background. A detector which identifies 100 percent of the muons correctly but misidentifies a large number of hadrons is not useful. One technique for estimating background is to use bubble chamber measurements from one accelerator cycle and EMI data from another cycle. The frequency that such switched information caused a track to be tagged as a muon is a direct estimate of that background which does not take into account the times that hadrons passed through the absorber without interacting. This was typically a few percent for the first plane and was negligible for the second.

Both the efficiency and the background depend upon the minimum constraint class (for delay line solutions) used in the analysis. A sample of 2136 (acceptance corrected) tracks with

P_{tr}^2 above 15 $(GeV/c)^2$ was used to determine the two plane efficiency. Tracks which pass this requirement should be muons with a negligible background. Using the muon selection criteria described in the next section, the following values are typical for the EMI efficiency and background (with the minimum constraint class set at OC):

Efficiency	Background	
0.76	0.01	Combined first and second planes

The statistical error on the efficiency is small, less than +/- 0.01, but a systematic error of +/- 0.05 is estimated because of an observed variation of efficiency between the laboratories which did the measurement of the bubble chamber film and because of a small variation with time. Throughout this analysis, only one value, 0.76, was used for the two plane efficiency. No results presented here are sensitive to small errors in this efficiency.

For the first plane alone, the efficiency is higher, approximately 0.90 with an accidental background of 0.03. The background for the single first plane needs further study. While this background was small for momenta above 10 GeV/c, slower tracks tended to have a larger error in extrapolation and a correspondingly larger background. Between 5 and 10 GeV/c, the background could be as much as 10 percent. Only the two plane combination is used in this work.

A.5 Muon Selection Criteria

In the hybrid detection system, a simple concept is used to detect muons. Hadrons originating in the bubble chamber pass through its wall and undergo strong interactons in the absorber material. The secondary products are usually stopped before reaching the EMI. Even if the hadrons scatter elasticaly, they may undergo large angular deflections. Hadrons or hadronic byproducts that reach the EMI are, in general, not along the particle's trajectory seen in the bubble chamber.

A muon, on the other hand, undergoes electromagnetic interactions. The hadron absorber only slows it down, not seriously deflecting it. Upon reaching the EMI, it passes through

one of the MWPC's causing it to fire.

To identify a muon candidate, the track's position and momentum were extrapolated from bubble chamber measurements. The extrapolation process took into account the varying magnetic field and also the energy loss due to ionization. At the extrapolated position on an EMI plane, a MWPC was then searched to check for a hit nearby. Depending upon the muon selection criteria being used, that track could be tagged as a muon if the hit was close enough.

A charged pion or kaon could be a muon candidate. There was a chance that somewhere along its path the meson decayed into a muon. This is a possible source of contamination in event muon identification. Using experimental hadron distributions, however, this contamination was found to be small, less than one percent. Charmed particles have been detected by the observation of dilepton final states in neutrino interactions (Reference 42). Some decay modes of charmed mesons have muons in the final state. But, the observed rate for this was small, again less than one percent. Both of these backgrounds are neglected in the present analysis.

For muon selection, the EMI can be used either as a single plane or as a double plane device. Both ways have advantages and disadvantages. When using the single first plane of the EMI, the geometrical acceptance is much better than when two planes are

used. In addition, by requiring only one plane to detect the particle, the efficiency was higher than if both planes must simultaneously register hits. Background, however, is a problem. There were many interactions in the walls of the bubble chamber and in the absorber material creating charged particles which passed through the first plane. The precise time that a track exited the bubble chamber is not known. Since it is not possible to measure a track's trajectory between the bubble chamber and the first EMI plane, background hits may form an accidental match with the extrapolated track and cause it to be mistakenly called a muon.

The problem with accidental matches would be even more severe if the second plane had been used alone. Similarly, there would be a high accidental match rate if the two planes were logically or'ed together. In this experiment, both EMI planes are used together by requiring detection of a particle in the two planes simultaneously. The chance that a background track would match the complete trajectory of a candidate muon through both planes of the EMI is very small, therefore a track detected in both EMI planes is almost certainly a muon.

The muon selection algorithm for double plane analysis in this experiment is simple. There must be hits in the first and second plane which are in time coincidence (within 0.3 microseconds) of each other. The nearness of the hits to the

extrapolated position used in conjunction with the error on the extrapolation process can be used to form a chi-squared probability that the track matches those hits. The chi-squared probability takes into account the correlation between the errors in extrapolating to the first and second EMI planes:

$$\chi^2 = \frac{\sigma_{2x}^2\Delta_{1x}^2 - 2C_x\Delta_{1x}\Delta_{2x}\sigma_{1x}\sigma_{2x} + \sigma_{1x}^2\Delta_{2x}^2}{\sigma_{1x}^2\sigma_{2x}^2 - (C_x\sigma_{1x}\sigma_{2x})^2} + \frac{\sigma_{2y}^2\Delta_{1y}^2 - 2C_y\Delta_{1y}\Delta_{2y}\sigma_{1y}\sigma_{2y} + \sigma_{1y}^2\Delta_{2y}^2}{\sigma_{1y}^2\sigma_{2y}^2 - (C_y\sigma_{1y}\sigma_{2y})^2} \tag{A.2}$$

where:

1,2 refers to either first or second EMI plane

x,y is one of the two PWC coordinates

Δ is distance between PWC solution and extrapolated track

σ is error in extrapolation of the track

C_x and C_y are numbers between -1 and 1 which represent the amount of correlation between the x and y errors of the two planes. A minor modification of the formula arises because the distribution of errors, for a particular coordinate, is more closely described by the sum of two gaussians rather than one. The selection of muons requires only a cut on the chi-squared probability. Cutting at a probability of 0.001 allows negligible background into the muon sample and at the same time accepts most of the muons which can be found with the combined planes.

For the first plane of the EMI, a chi-squared probability can be defined. But since there is a background problem, modified criteria are used. A formalism incorporating inefficiency and background was developed by the Hawaii-Berkeley collaboration and is described in Reference 39. Two quantities Prom and Proh are defined, corresponding to muon and hadron confidence levels. Muons tend to have low Proh while hadrons have low Prom. The definition of the two quantities is:

$$\text{Prom} = (1-\varepsilon)e^{-\frac{\chi^2}{2}} e^{-\rho\pi\sigma_x\sigma_y\chi^2} + \varepsilon e^{-\rho\pi\sigma_x\sigma_y\chi^2} \qquad (A.3)$$

$$1 - \text{Proh} = (1-e^{-\frac{L}{\lambda}})e^{-\rho\pi\sigma_x\sigma_y\chi^2} + e^{-\frac{L}{\lambda}} \text{Prom}$$

The variables are defined as:

ε = EMI inefficiency

$\chi^2 = (\Delta_x / \sigma_x)^2 + (\Delta_y / \sigma_y)^2$

ρ = Background in EMI, number of hits/cm

Δ_x = distance between x coordinate of extrapolated track and PWC solution

Δ_y = same for y coordinate

$\sigma_{x,y}$ = Error in extrapolation to EMI

L/λ = Number of absorbtion lengths traversed by the track.

For selecting a sample of muons, a cut is made on Proh by requiring it to be less than 0.07. This gives a sample which is unbiased in rejection of hadrons.

Since background is a large problem when using the first plane by itself, this work uses only the two plane method described above. Comparisons of corrected differential distributions from single and double plane analysis do not, however, show significant difference.

A.6 Internal Picket Fence

The IPF (Reference 41) consists of 18 drift chambers installed in the vacuum jacket of the bubble chamber to reduce out of time background in the EMI. These devices have poor spatial resolution and are used for timing only. All 18 pickets are OR'ed together to increase efficiency, but still have only a small amount of background.

The IPF works as designed in giving event timing information. However, as Figure 42 shows, the efficiency for the IPF to fire on a charged current event is a function of the charged primary multiplicity. To avoid this bias, the IPF information is not used.

B. Monte Carlo

In this experiment, an incoming neutrino of unknown energy struck a moving nucleon. Some of the outgoing hadrons were not charged and therefore, unseen. This means that many of the kinematic variables could only be measured approximately. To simulate experimental resolution and to check for biases, a Monte Carlo program is used to generate events according to specified distributions. Events with known kinematic quantities were subjected to experimental resolution, biases and cuts. Systematic effects can then be conveniently studied.

The Monte Carlo program is logically divided into two sections. The first section deals with the incoming neutrino, outgoing lepton and the target, while the second section deals with generation of the final state hadrons.

B.1 Beam, Outgoing Lepton and Target

The incoming neutrino flux (shown in Figure 2) was calculated by S. Mori (Reference 45). It was observed that at low neutrino energies, the calculated flux was significantly lower than experimentally seen. An explanation for this discrepancy may be that secondary interactions inside the beryllium oxide target produced pions and kaons of lower energy that decayed into neutrinos of correspondingly lower energy. For use in the Monte Carlo, the low energy portion of the neutrino spectrum was increased to represent the observed neutrino event distribution.

The target is chosen to be either a free neutron or a free proton. The target's Fermi momentum is represented by the Hulthen wave function. This motion has several consequences. A flux factor must be calculated to transform the flux in the laboratory into that of the target rest frame. In addition, since the neutrino-nucleon cross section is a function of energy, the cross section for an event must also be calculated in the target rest frame.

The target, incoming neutrino, outgoing lepton and outgoing hadrons are chosen according to a distribution. The event distribution can be written for charged-current interactions on protons with the assumption of Bjorken scaling, including sea:

$$N_{pevents} \propto \left[(E_t+P_t\cos\theta_t)^2\phi^2(P_t)P_t^{\,2}\ N(E_\nu)E_\nu x\right] \qquad \text{(B.1)}$$

$$\left\{\left[\cos^2\theta_c(d_v+d_s) + \sin^2\theta_c(s_s) + (1-y)^2(u_s)\right] + \Theta(W-W_c)\sqrt{\frac{W^2-W_c^2}{W^2}}\left[\sin^2\theta_c(d_v+d_s)+\cos^2\theta_c(s_s)+(1-y)^2c_s\right]\right\}$$

where:

d,u,s,c are the quark structure functions,

$E_\nu N(E_\nu)$ is the event energy distribution,

Θ is the step function,

W is the mass of the outgoing hadrons,

W_c = 2.5 GeV/c,

θ_c is the Cabbibo angle, approximately 0.2,

E_t, P_t , $\cos\theta_t$ are the energy, momentum, and direction of the target nucleon,

$\phi(P_t)$is the deuteron wave function.

For neutron targets:

$$N_{nevents} \propto \left[(E_t+P_t\cos\theta_t)^2\phi^2(P_t)P_t^{\,2}\ N(E_\nu)E_\nu x\right] \left\{\left[\cos^2\theta_c(u_v+u_s) + \sin^2\theta_c(s_s) + (1-y)^2(d_s)\right] + \Theta(W-W_c)\sqrt{\frac{W^2-W_c^2}{W^2}}\left[\sin^2\theta_c(u_v+u_s)+\cos^2\theta(s_s)+(1-y)^2c_s\right]\right\} \quad (B.2)$$

Here N is the number of events at a given x, y, E_ν, and target momentum. The square root multiplying the step function comes from the fact that in some events, the mass of the outgoing hadronic system is too small to allow charmed particles to be produced. When this occurs, some quark transitions are totally forbidden, such as D-quark to C-quark, while others, such as S-quark to U-quark, are suppressed by the square of the sine of the Cabbibo angle.

The momentum of the outgoing lepton is determined by the values of x,y,E_ν and target momentum chosen. The azimuthal angle of the muon is chosen at random. Some care must be used since the x and y variables were generated in the target rest frame, while

in the experiment the outgoing lepton is detected in the laboratory system. There are some combinations of x,y and E_ν which are not kinematically allowed. If such a combination is generated in the Monte Carlo, the event is discarded immediately.

B.2 Outgoing Hadrons

The four-momentum of the final hadronic state is specified since the beam, target and outgoing lepton were already generated. The question is then how to obtain particles which are seen in the laboratory.

The average charged multiplicity is chosen to be (Reference 46) a logarithmic function of the mass, W, of the hadronic final state:

$$N_c = 0.68 + 1.29 * \ln(W^2) \qquad (B.3)$$

The average total multiplicity is generated as:

$$\langle N \rangle = 1.5 * N_c - .5 \qquad (B.4)$$

The factor of 1.5 comes from the assumption that one-third of the outgoing pions are neutral as observed in hadronic interactions. For a particular event, the average total multiplicity $\langle N \rangle$ is calculated, then the total multiplicity for that event is formed according to (Reference 47):

$$P_N = \frac{0.176}{\langle N \rangle} \frac{(1.8)^{3.6t + 6.48}}{\Gamma(1.8t + 4.24)} \quad ; \; t = 2.5\left(\frac{N - \langle N \rangle}{\langle N \rangle}\right) \qquad (B.5)$$

The outgoing baryon is chosen to be a neutron or proton with equal probabilty. The remaining hadrons are chosen to be pions with equal probability for positive, negative and neutral pions except that charge is forced to be conserved.

After all particle masses and charges are chosen, the program GENIS from the standard SAGE (Reference 48) Monte Carlo package is used to generate the momenta of the outgoing hadrons according to transverse momentum damped phase space.

B.3 Resolution in Kinematical Variables

The Monte Carlo can be used to study the effects of the neutrino energy estimation on resolution of variables in charged current interactions. No attempt is made to measure kinematic variables in neutral current events since a large part, as much as half, of the outgoing energy is contained in neutral particles.

Several methods of estimating the neutrino energy were studied. The so-called Bonn method (Reference 12) was chosen for this experiment. Other commonly used estimations (Reference 49) give roughly the same results.

Figure 33 shows the variables used to discuss the neutrino energy estimation. Conservation of momentum implies that the neutrino energy is just the sum of the longitudinal muon and hadronic momentum. This muon can be identified either by

kinematic (Chapter III) or by EMI (Appendix A) methods. The total hadronic momentum is usually not seen, only charged hadrons are observed. The transverse momentum of the hadrons $P_t h$ must balance the muon transverse momentum $P_t u$. In the Bonn method, the assumption is made that the components of the visible and total hadronic momenta are proportional:

$$\frac{P_t c}{P_l c} = \frac{P_t tot}{P_l tot} \qquad (B.6)$$

This gives an estimate for the longitudinal hadronic momentum and, therefore, an estimate for the neutrino energy:

$$E_\nu = P_l \mu + P_l c \cdot (1 + P_t n / P_t c) \qquad (B.7)$$

Using Monte Carlo generated events with known energy, the neutrino energy estimation can be checked. Figure 34 shows a distribution of E_ν(calculated)/E_ν(generated) for charged current neutrino events which would be identified by the kinematic

selection technique of Chapter III. A small part of the uncertainty in the neutrino energy estimate is due to the Fermi motion of the target.

Table 2 gives quantitative information on the size of the relative error in kinematic variables. These errors are, in general, not independent, as can be seen by considering the variable v defined as:

$$v = xy \tag{B.8}$$

In the absence of target motion, v can be expressed in terms of measured muon variables:

$$v = E_{\mu} \; (1-\cos\theta)/M \tag{B.9}$$

With good muon identification, the resolution in v is limited only by the accuracy of a single track's momentum measurement. The error in v is, in general, less than 5 percent, which implies a correlation in the errors for x and y since:

$$\Delta v = y\ \Delta x + x\ \Delta y = \text{about } 0. \qquad (B.10)$$

B.4 Comparison of Monte Carlo Features with Data

If the Monte Carlo is to supply corrections, it is important that the Monte Carlo reproduce the main features of the data. Charged current data can be compared with Monte Carlo predictions, as has been shown in several places in this thesis. In Figure 2, the incoming neutrino flux is shown to be parameterized correctly. Quasielastic events (Chapter 3) verified the flux. The x and y distribution of Chapter three are in agreement with the parameterizations (Reference 9) used in the Monte Carlo. The neutral current analysis of Chapter 4 showed that the generated P_{tr} shape agreed with that observed experimentally.

The dependence of the multiplicity on the mass of the hadronic final state, W, has been checked for neutron and proton targets separately using data. The logarithmic rise is compatible with that observed in previous neutrino experiments (Reference 46).

Distributions in hadronic variables are not studied in this thesis. General features of the data are observed to agree with the Monte Carlo. As Figure 35 (from the data sample of Section III.4) shows, the P_t -damped phase space reproduces the z (fraction of total hadronic energy carried by a single hadron) distribution for the bulk of the data, but, high values of z deviate slightly. The transverse momentum of the individual hadrons with respect to the total hadronic direction (not to be confused with P_t^H) is shown in Figure 36. Agreement between data and Monte Carlo is adequate, but not as good as in the preceeding figure. In general, simple P_t -damped phase space reproduces most longitudinal distributions, while transverse distributions are described more poorly. At higher energies, the outgoing hadrons might be modelled on the basis of a jet structure.

References

1 F. Reines and C. Cowan, Phys. Rev. 113, 273 (1959).

2 S. Weinberg, Phys. Rev. Lett. 19 1264 (1967) ; A. Salam, in Elementary Particle Physics, ed. N. Svartholm (Almqvist and Wiksells, 1968).

3 F. J. Hasert, et al, Phys. Lett. B46, 138 (1973) A. Benvenuti, et al, Phys. Rev. Lett. 32, 800 (1974).

4 C. Callan and D. Gross, Phys. Rev. Lett., 22, 156 (1969).

5 J. D. Bjorken, Phys. Rev. 179, 1547 (1969).

6 P.Bosetti, et al, Nucl. Phys. B142, 1 (1978).

7 R. P. Feynman, Photon Hadron Interactions, (W.A. Benjamin,Inc. 1972)

8 M. Gell-Mann, Phys. Lett. 8, 214 (1964).

9 R.D. Field and R.P. Feynman, Phys. Rev. D15 2590 (1977) A.J. Buras and K.J.F. Gaemers, Nucl. Phys. B132 249 (1978).

10 S. L. Glashow, J. Iliopoulous and L. Maiani, Phys. Rev. D2 1285 (1970)

11 S. Mori, "Wide Band Single Horn System", Fermilab TM-663, (May 1976)

12 R. Heilmann, University of Bonn BEBC neutrino-hydrogen collaboration, WA21-int-1 (1978).

13 F.T. Solmitz, A.D. Johnson, T.B. Day, "Three View Geometry Program", 2nd. Ed., Alvarez Group Programming Note P-117, University of California - Lawrence Radiation Laboratory (1966).

14 J. Hanlon et al., Phys. Rev. D19, 49 (1979). J.E.A. Lys et al., Phys. Rev. D16, 3127 (1977). T. Dombeck et al., Phys. Rev. D18, 86 (1978). S. Dado et al., Fermilab-Pub-78/83-EXP. R. E. Ansorge et al., Nucl. Phys. B109, 197 (1976). K. Dziunikowska et al., Phys. Lett. 61B, 316 (1976). K. Moriyasu et al., VTL-PUB-49 (1978).

15 R.Engelmann,"Double Scattering in 5.5 GeV gamma-deuterium interactions", E545 internal report, SUNY-SB (April 1980).

16 V.P. Gupta, et al, Phys. Rev. D14, 42 (1976).

17 S.J. Barish, et al, ANL-HEP-PR-78-30

18 N.Samios in "Proceedings of the 1975 International Symposium of Lepton and Photon Interactions at High Energy," Stanford, 527 (1975).

19 W.Lerche, et al, Nucl. Phys. B135, 45 (1978).

20 N. Armenise, et al, submitted to the 1979 Lepton and Photon Symposium at Fermilab.

21 J. Bell, et al, Michigan preprint UMBC 78-8 (1978), W.Lerche, et al, Phys. Lett. 78B, 510 (1978).

22 A. Bodek, et al, Phys. Rev. D20, 1471 (1979).

23 E. Fernandez, Ph.D. Thesis, unpublised, Purdue (1979).

24 J. Bell,et al, Phys. Rev. D19, 1 (1979).

25 E.D. Bloom and F.J. Gilman, Phys. Rev. Lett. 25, 1140 (1970). R. Carlitz, Phys. Lett. 58B, 345 (1975). G.R. Farrar and D.R. Jackson, Phys. Rev. Lett. 35, 1416 (1975).

26 D.B. Lichtenberg and L.J. Tassie, Phys. Rev. 155, 1601 (1967). W.A. Mann, E-545 Internal Memo, Tufts Univ. (May 1980).

27 A. DeRujula, et al, Nucl. Phys. B154, 394 (1979).

28 P.C. Bosetti, et al, Nucl. Phys. B149, 13 (1979).

29 M. Jonker et al, CERN-EP/79-122 (October 1979).

30 C. Baltay, private communication, recent compilation of neutrino and antineutrino experiments (unpublished).

31 S. Mori, Fermilab TM-888 (July 1979).

32 R. Loveless, private communication.

33 F.A. Harris et al, Phys. Rev. Lett. 39, 437 (1977).

34 J. Blietshau et al, Phys. Lett. 88B, 381 (1979).

35 J. Marriner, thesis (unpublished), LBL-6438 (1977).

36 L.M. Sehgal, Phys. Lett. 71B, 99 (1977).

37 M. Holder et al, Phys. Lett. 72B, 254 (1977).

38 H. Deden et al, Nucl. Phys. B149, 1 (1979).

39 R. J. Cence et al., Nucl. Instrum. Methods 138, 245 (1976).

40 J. Marriner, Group A Programming note, LBL P-251 (1978).

41 S. Sommars, "An Introduction to EMI Programming", E545 Internal Report SUSB-Sept-78.

42 P.C. Bosetti, et al, Phys. Lett., 73B, 380,(1978).

43 M.L. Stevenson, "The Internal Picket Fence: A Device that Could Reduce the Background in the Phase 1 External Muon Identifier," LBL Physics Note 809 (Oct 1975).

44 S. Sommars and J. Hanlon, " Performance Characteristics of the Internal Picket Fence for E545," E545 Internal report (Oct 1979).

45 S. Mori, private communication. The results for flux calculations for 400 GeV/c incident protons are given in a memo by J. Grimson and S. Mori, Fermilab TM-824, 2941.0 (1978).

46 H. Saarikko reporting at Neutrino '79 for the ABCMO collaboration, CERN/EP 79-92 (Aug 1979).

47 O. Czyzewski and K. Rybicki, Nucl. Phy. B47, 633 (1972).

48 J. Friedman, LRL Group A programming note No. P-189, revised (1971).

49 G. Myant, CERN/ECFA/72-4 Vol. II., p. 117. S.J. Barish et al, Phys. Rev. D18, 2205 (1978). A. Grant, Nucl. Inst. Meth., 127, 335 (1975).

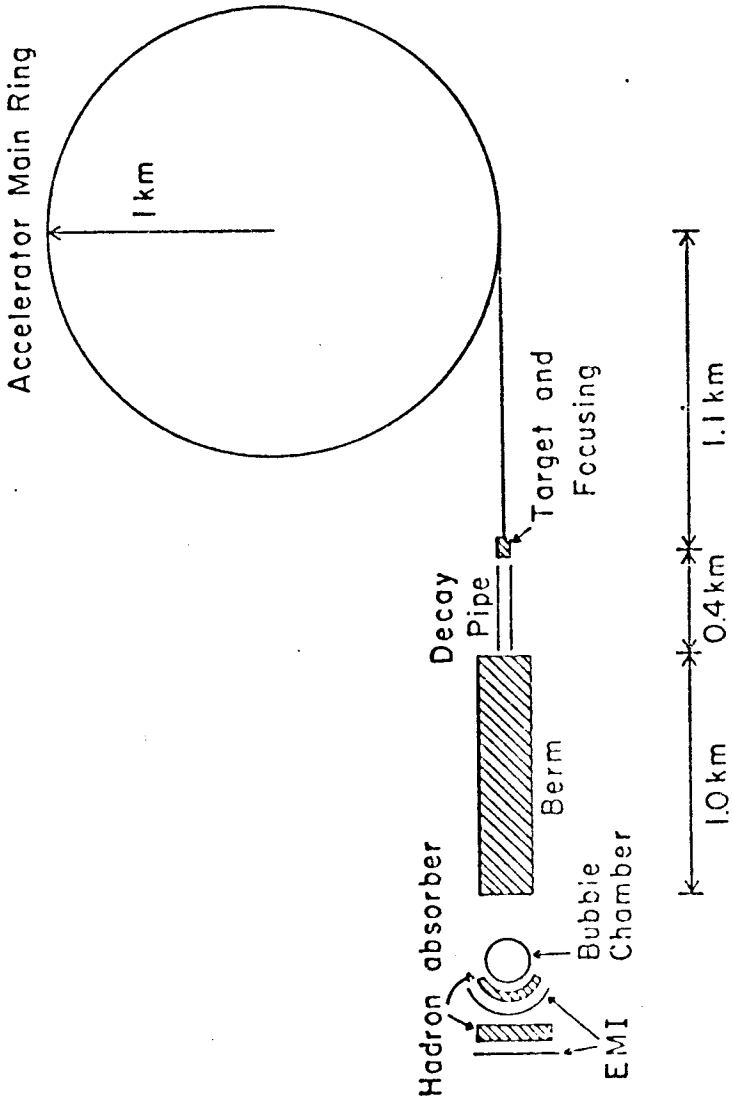

Fig. 1 Fermilab accelerator and neutrino beam line.

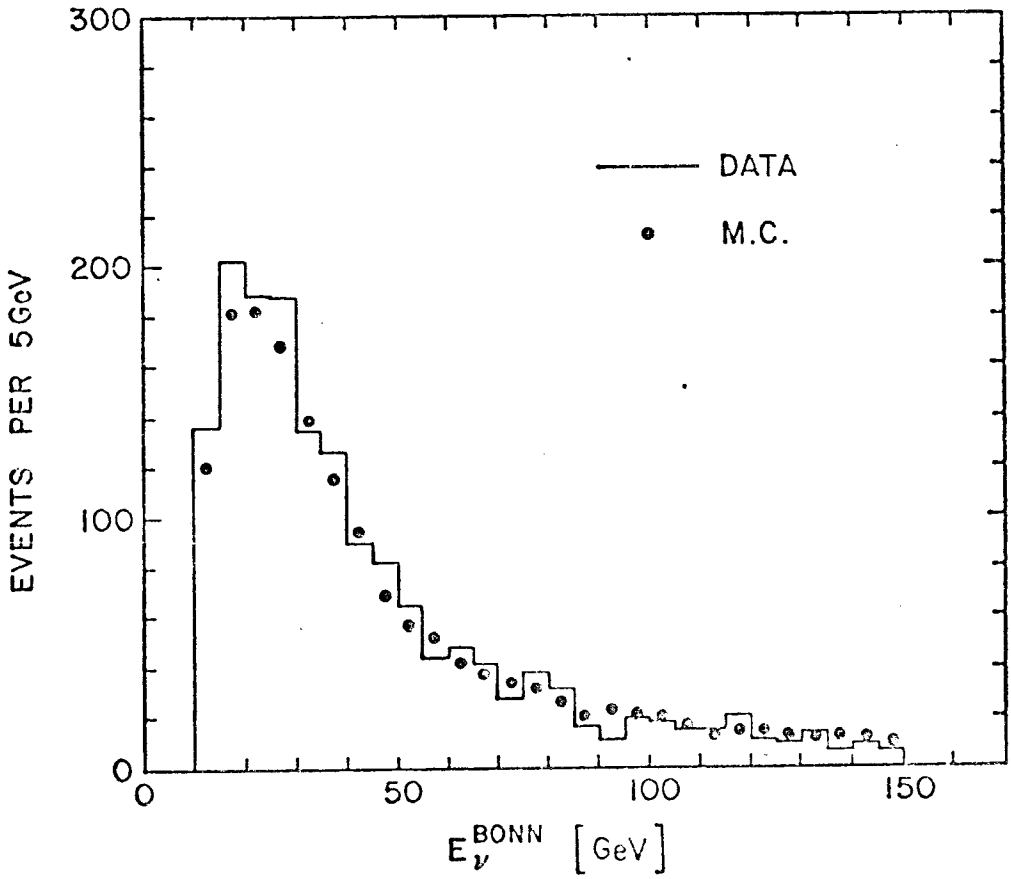

Fig. 2 Neutrino event energy spectrum. The solid histogram is the spectrum observed from charged current data (Chapter 3), while the dots are Monte Carlo predictions.

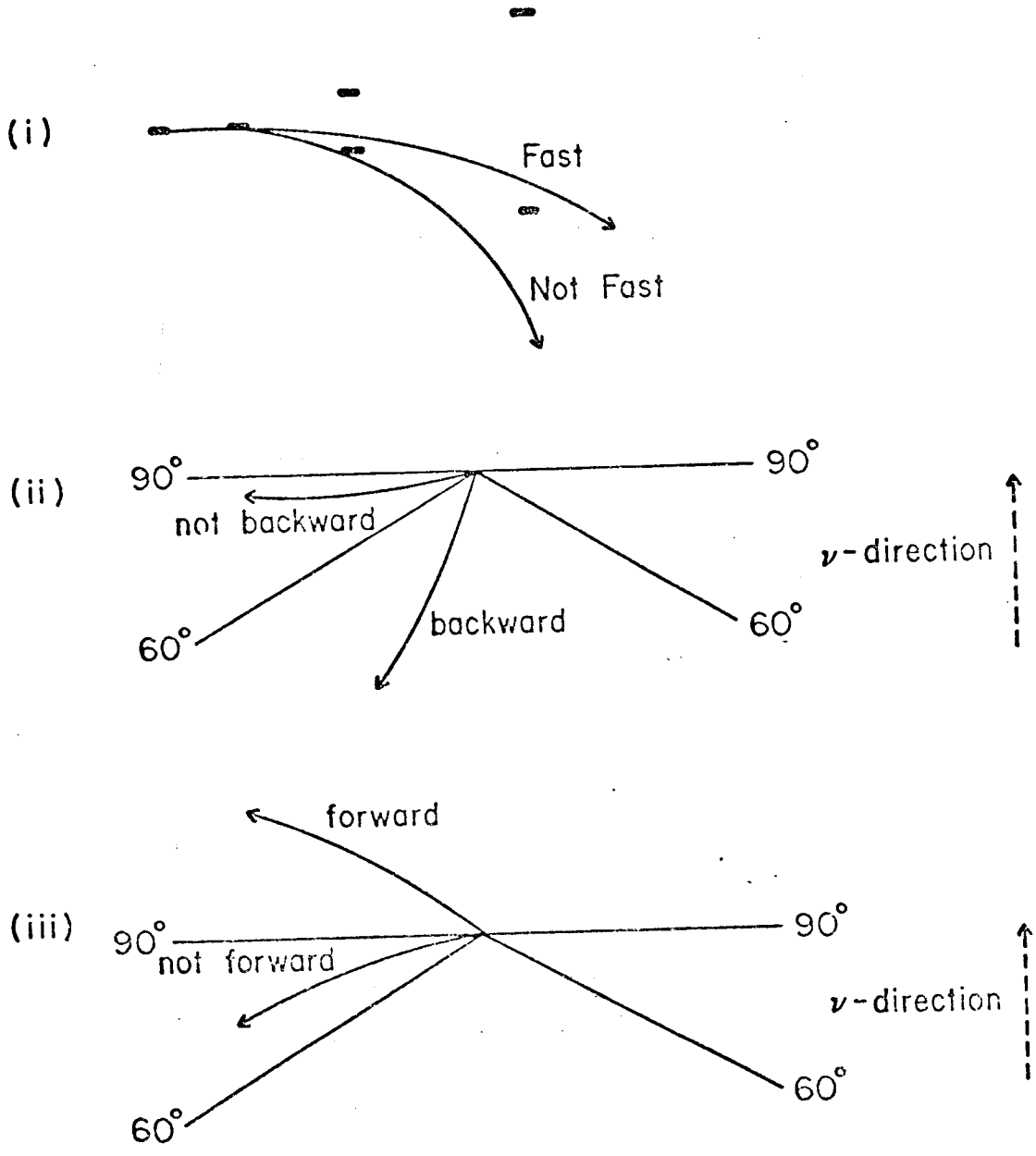

Fig. 3 Template used for selecting neutrino candidates. (i)Curvature template to determine whether a track is fast. (ii)Sixty degree template used to determine if a track is backward. (iii)Ninety degree template used to determine if a track is forward.

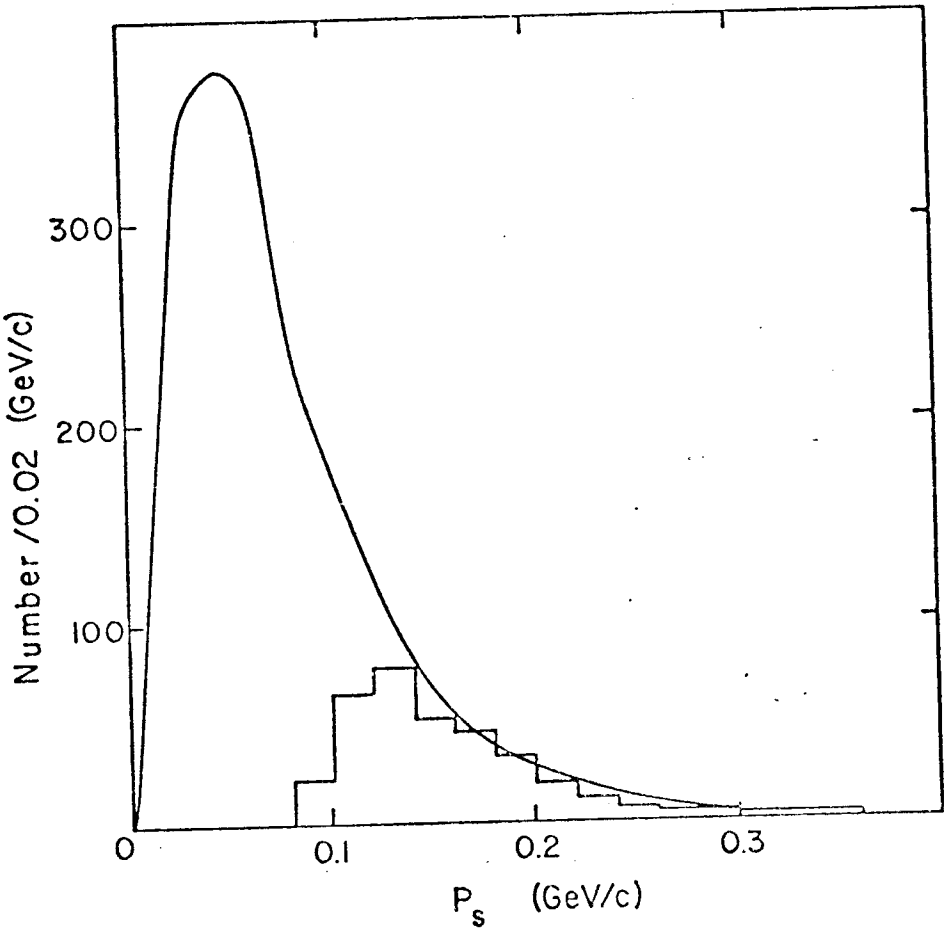

Fig. 4 Momentum distribution of backward, stopping protons. The curve represents the expected distribution from the deuteron wave function.

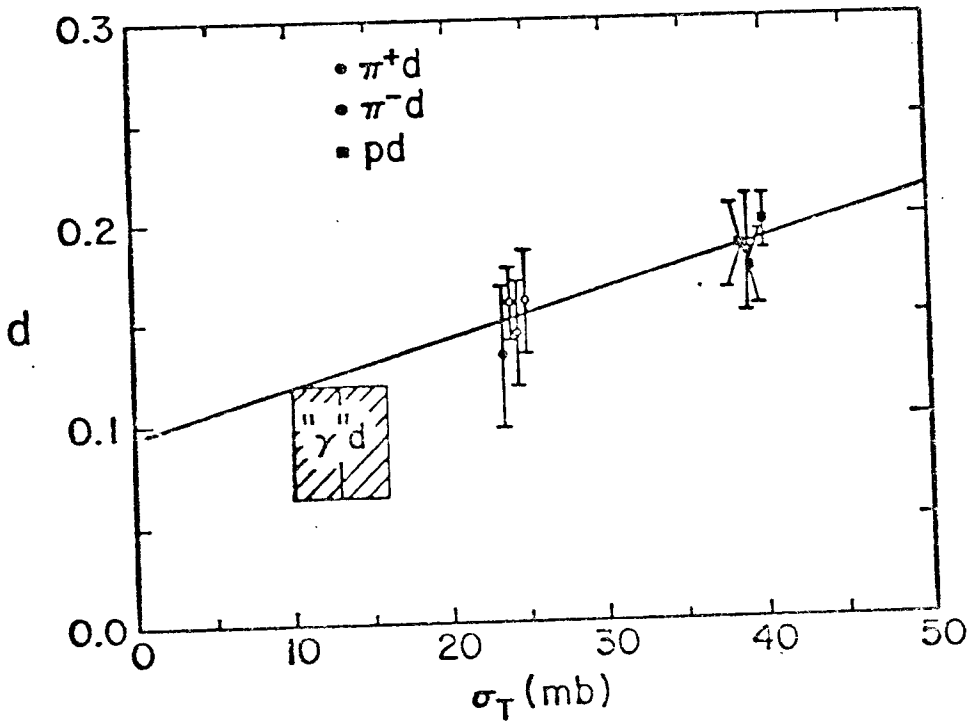

Fig. 5 Rescattering in deuterium as a function of total beam-nucleon cross section. The data proton and pion beam data are from Reference 14, while the box represents the rescattering fraction from the analysis (Reference 15) of a photon-deuterium experiment.

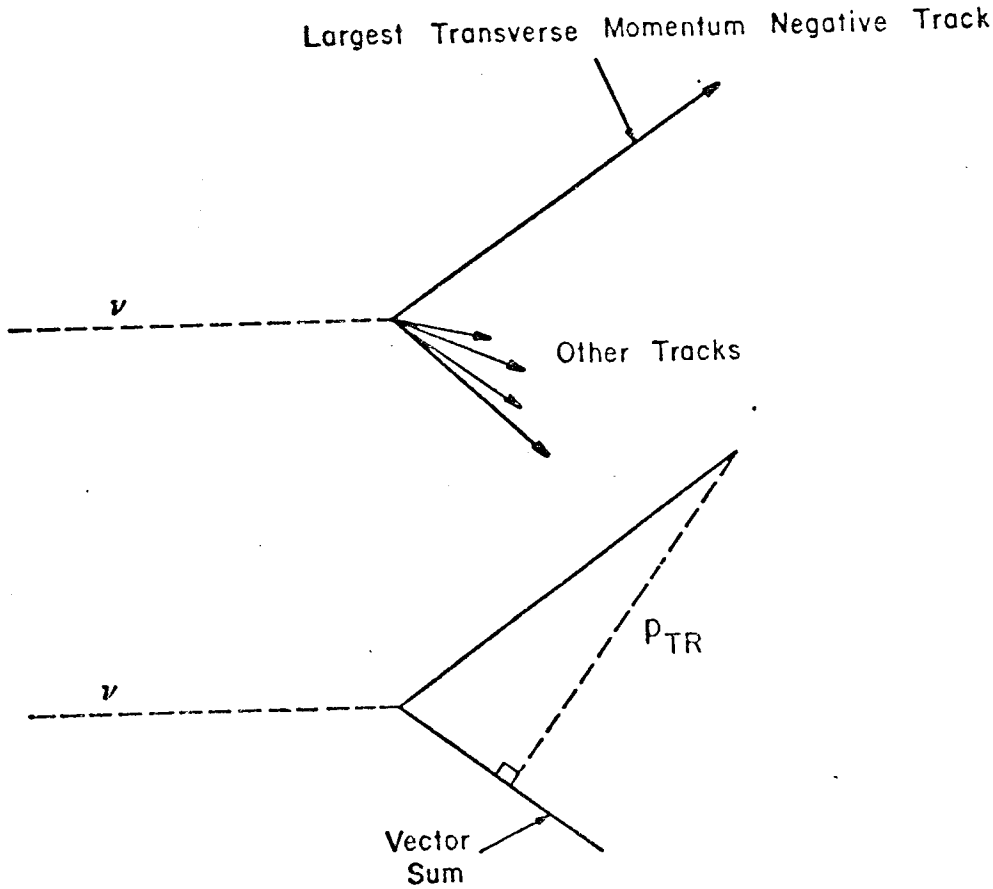

Fig. 6 Definition of P_{tr}.

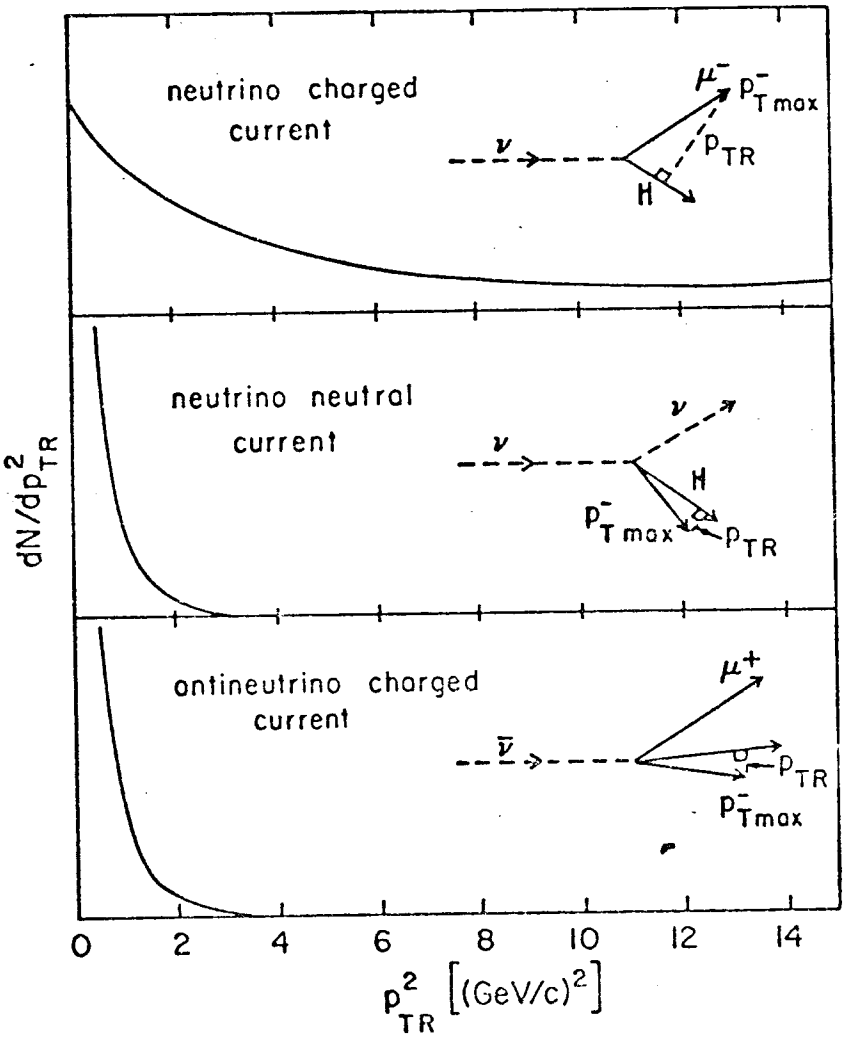

Fig. 7 P_{tr} distribution for (i) neutrino charged current interactions, (ii) neutral current interactions, and (iii) antineutrino charged current interactions as predicted by the Monte Carlo. Here H represents the vector sum of all particles other than the negative track with the highest transverse momentum. In (i), P_{tr} extends to much larger values than (ii) or (iii).

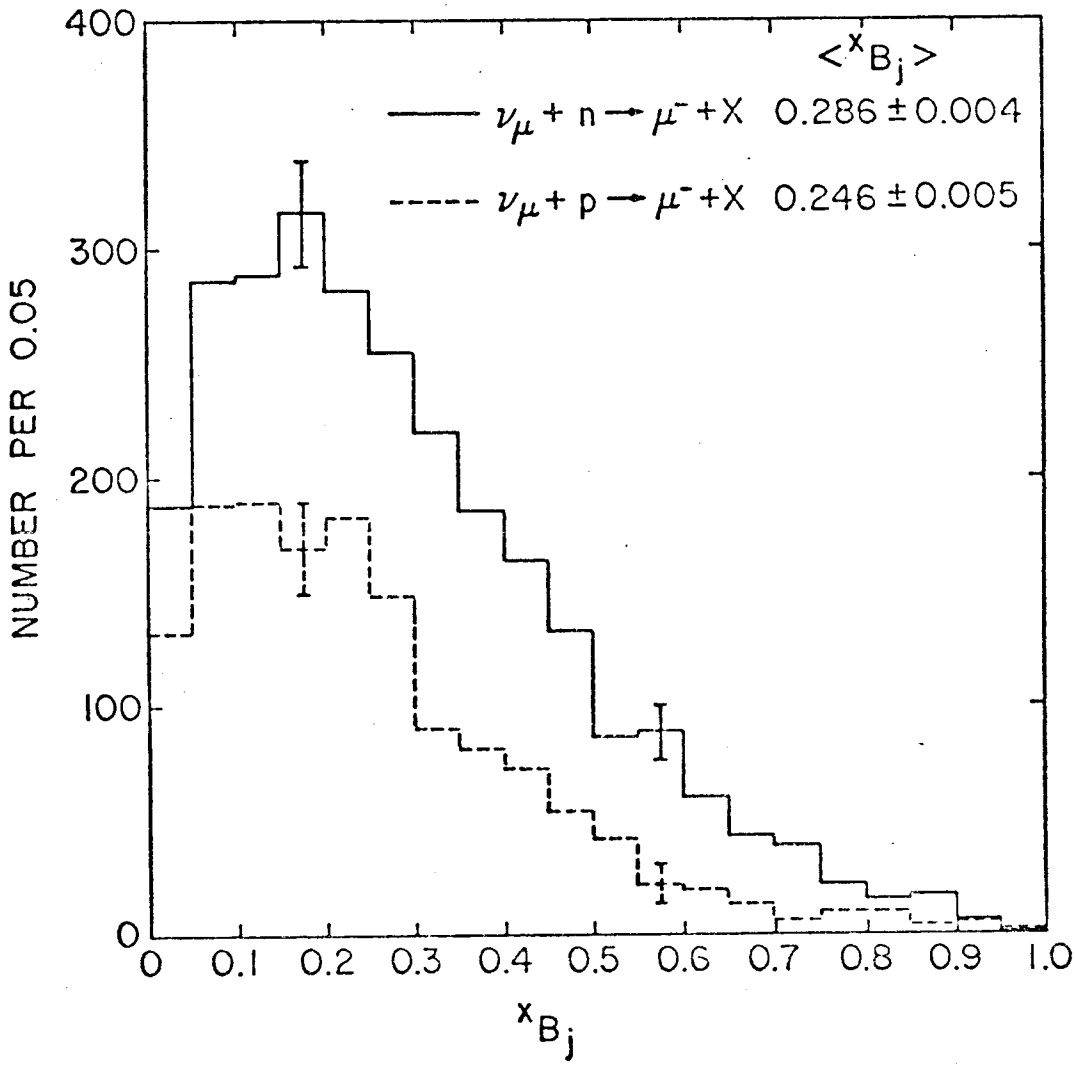

Fig. 8a Distribution in the Bjorken x variable from neutron and from proton target events (uncorrected), for events with $P_{tr} > 1.0$ GeV/c and Evis > 10 GeV.

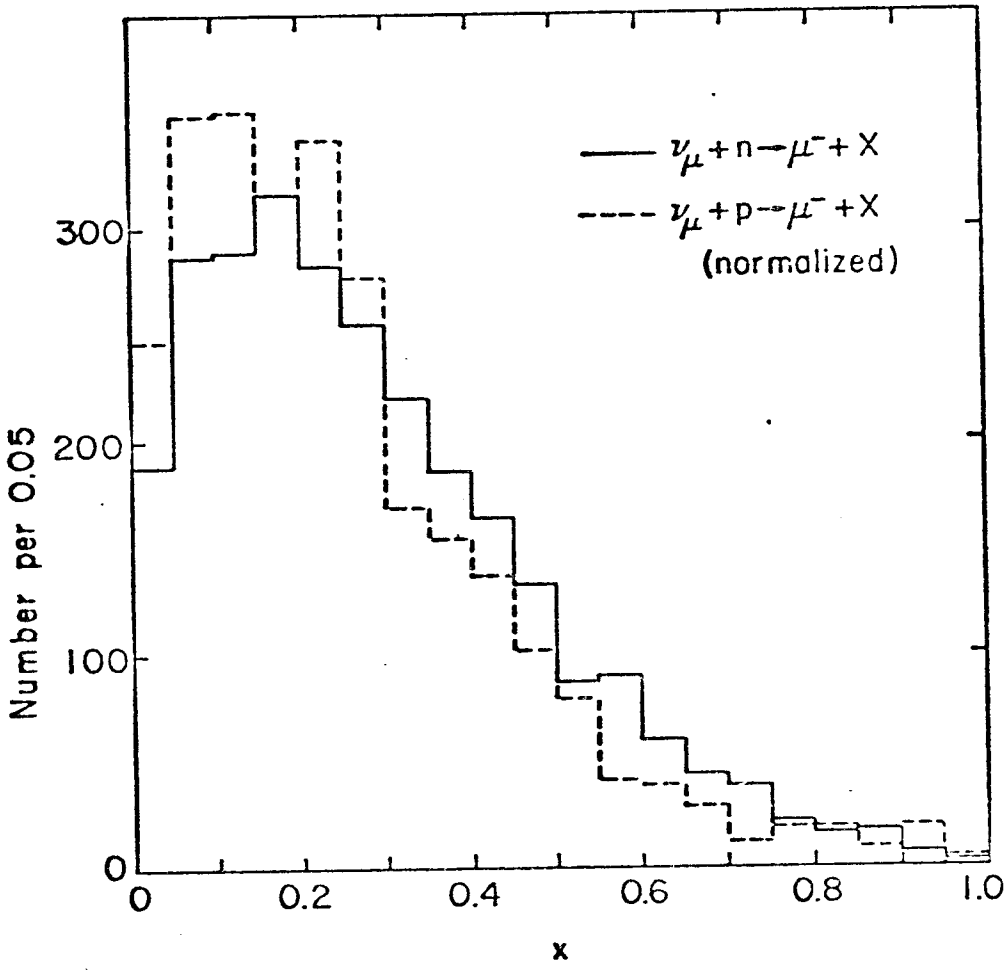

Fig. 8b The data of Figure 8a are shown again, but the proton distribution is normalized to the area of the neutron distribution.

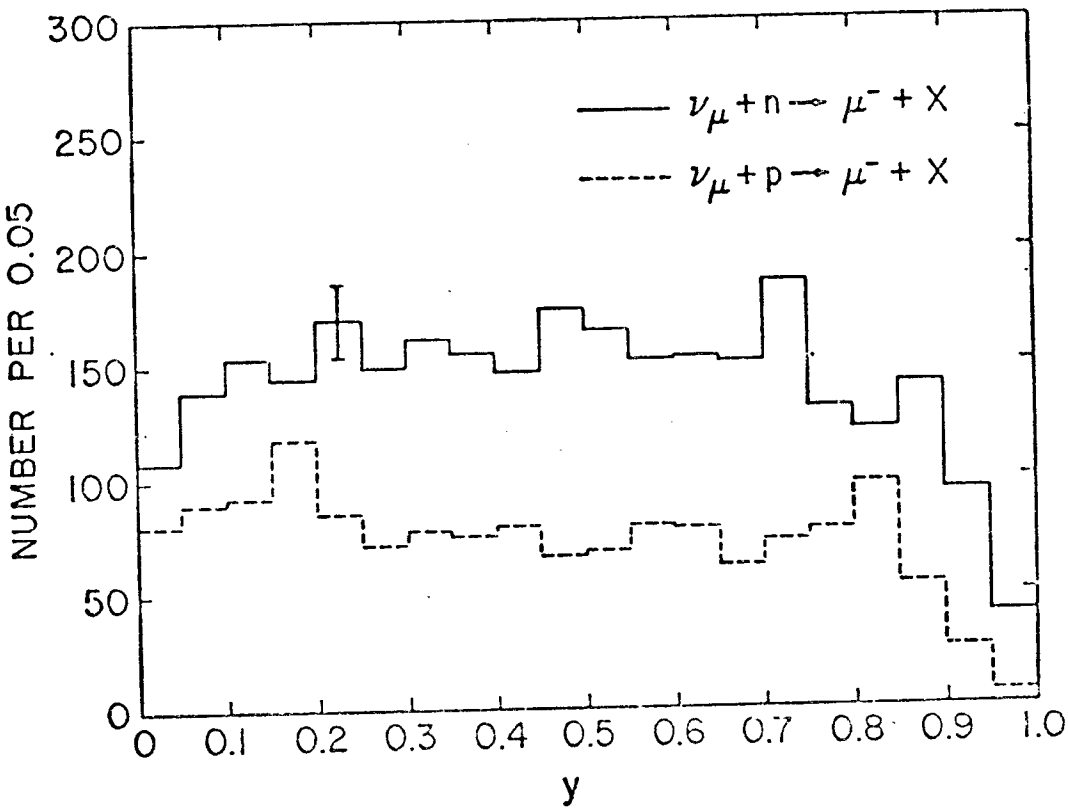

Fig. 9 Distribution in the Bjorken y variable from neutron and from proton target events (uncorrected), for the same data sample as Figure 8.

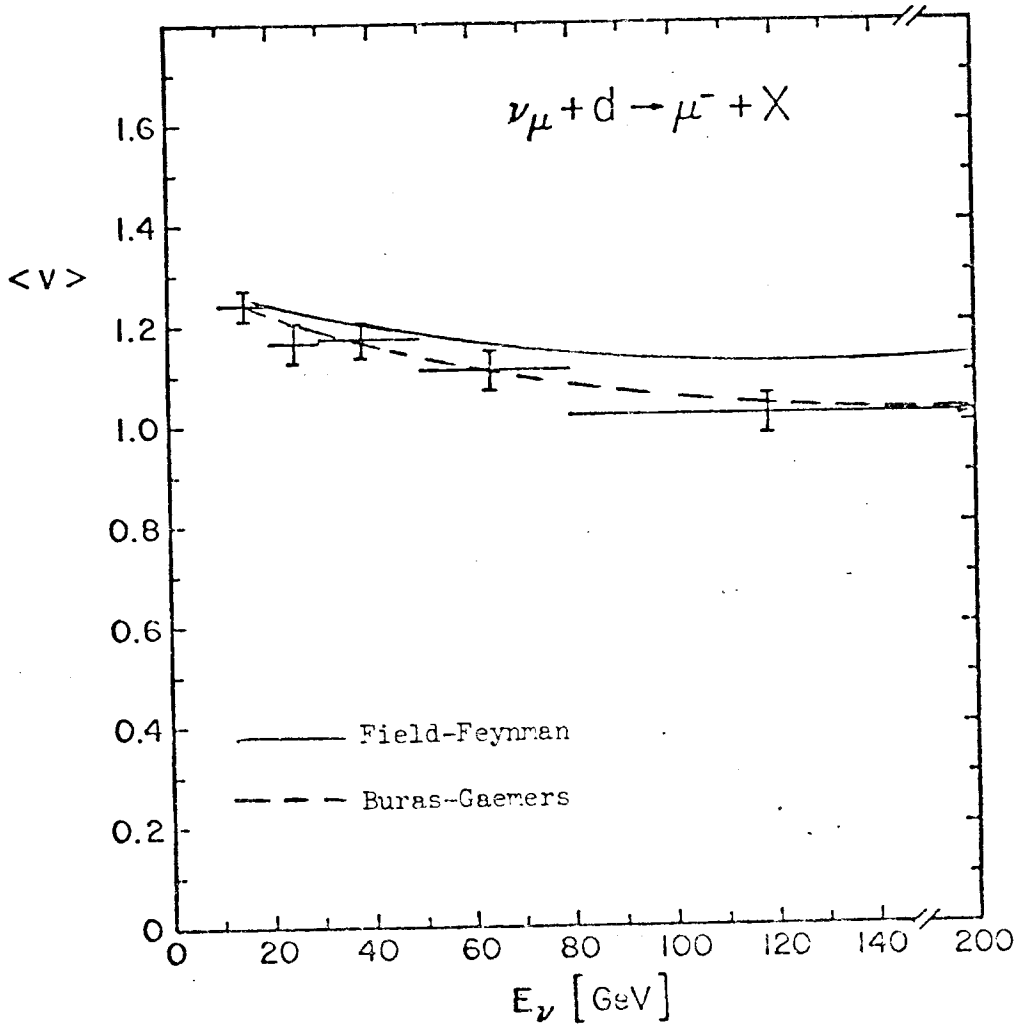

Fig. 10 Average v as a function of neutrino energy, for the same data sample as Figure 8. The lines represent the predictions of the Field-Feynman and Buras-Gaemers structure functions.

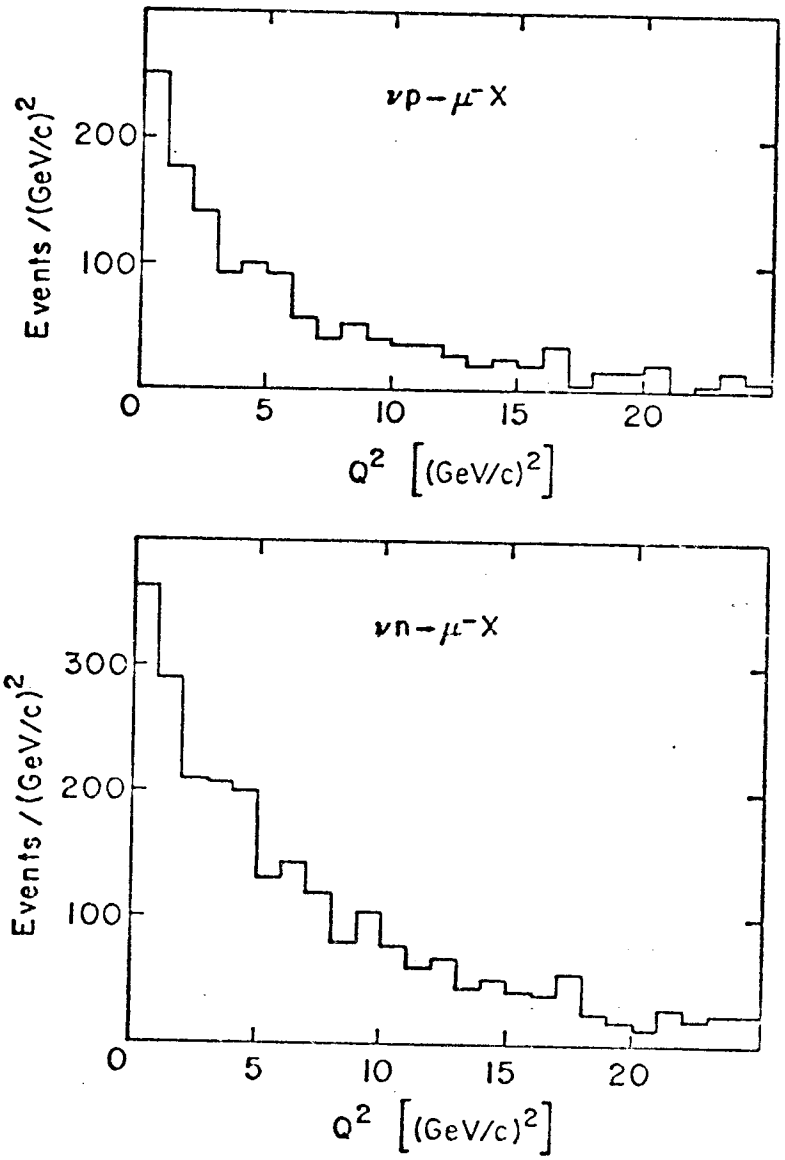

Figure 11a

Fig. 11 a)Q^2 and b)W distributions, for the data sample of Figure 8. The peaks in the W distributions are due to quasielastic reactions $\nu n \rightarrow \mu^- p$, and $\nu p \rightarrow \mu^- \Delta^{++}$. The shaded region contains those events where the missing transverse momentum is less than 200 MeV/c.

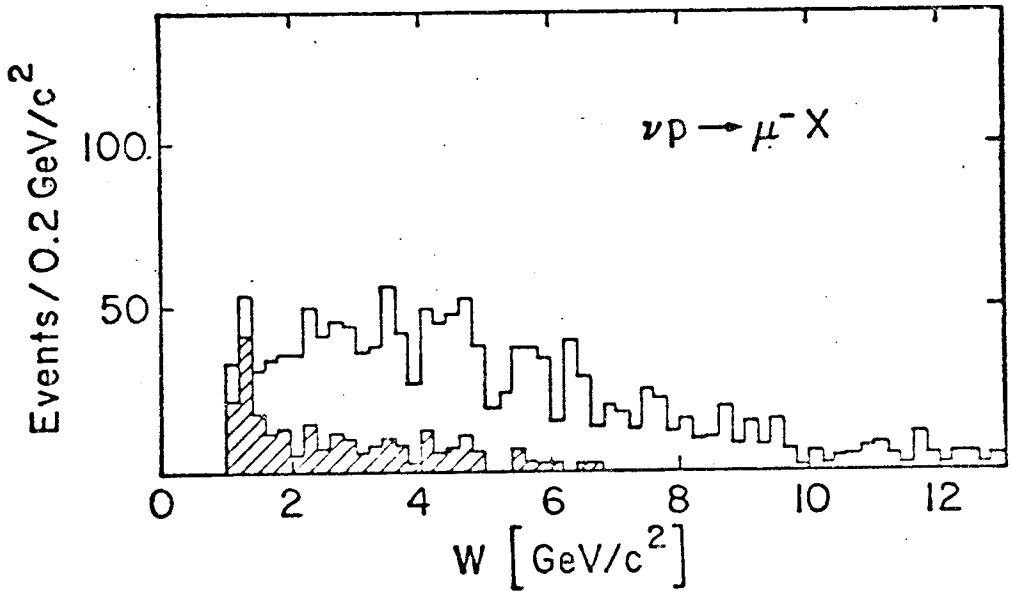
Events / 0.2 GeV/c²
100
50
νp → μ⁻X
0
2
4
6
8
10
12
W [GeV/c²]

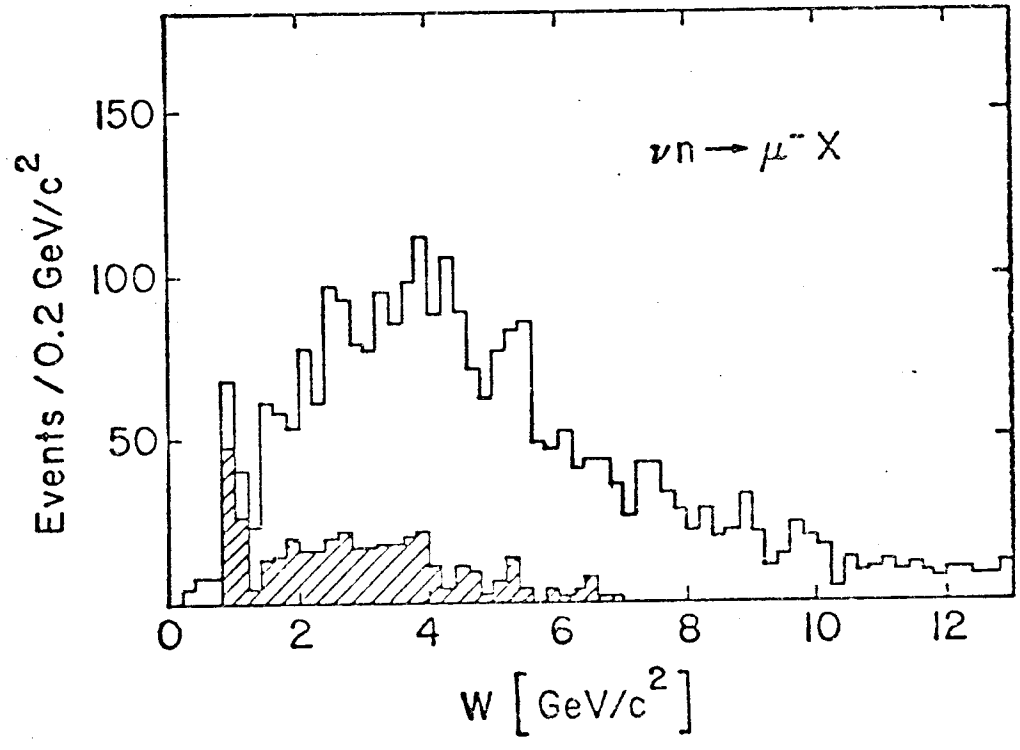
Events / 0.2 GeV/c²
150
100
50
νn → μ⁻X
0
2
4
6
8
10
12
W [GeV/c²]

Figure 11b

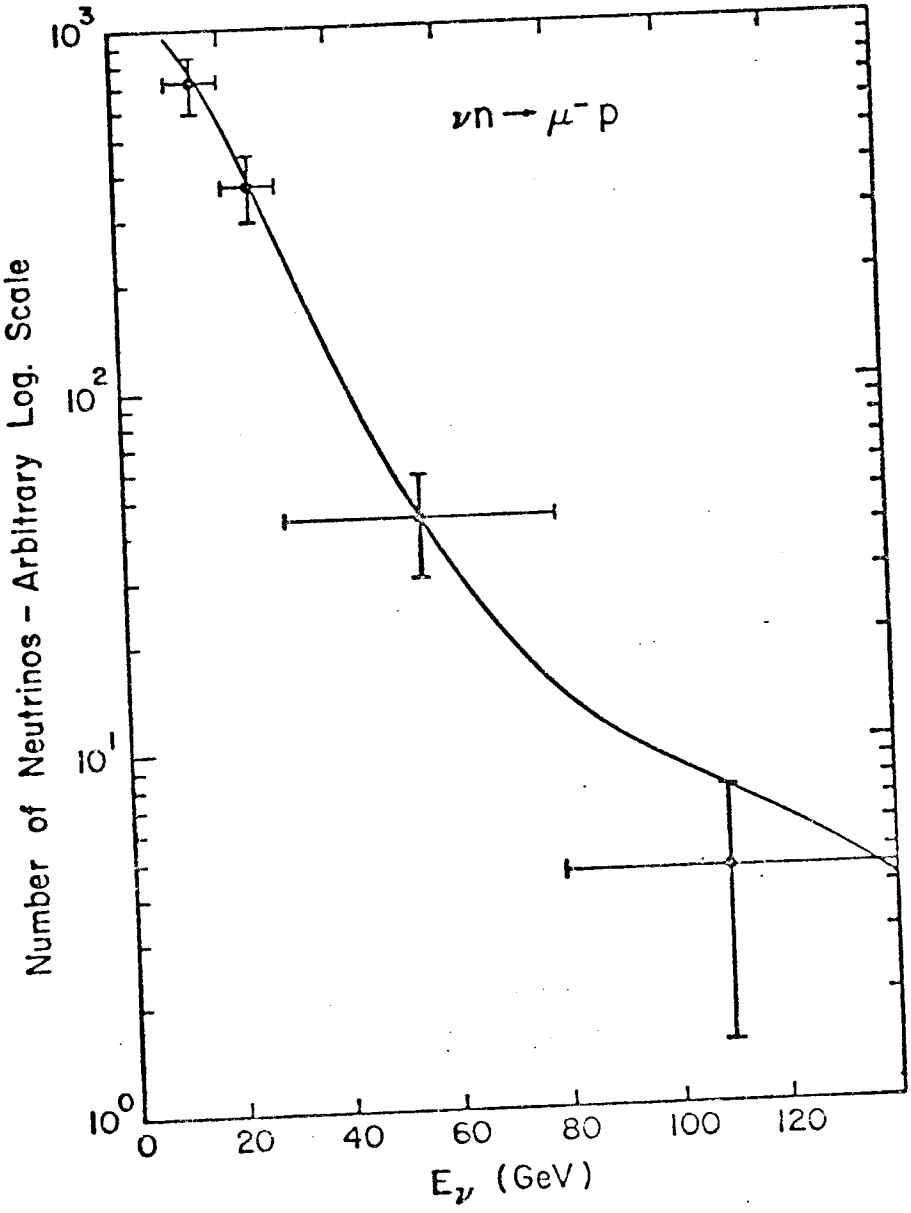

Fig. 12 Energy distribution of events coming from $\nu n \rightarrow \mu^- p$. The curve is the neutrino energy spectrum.

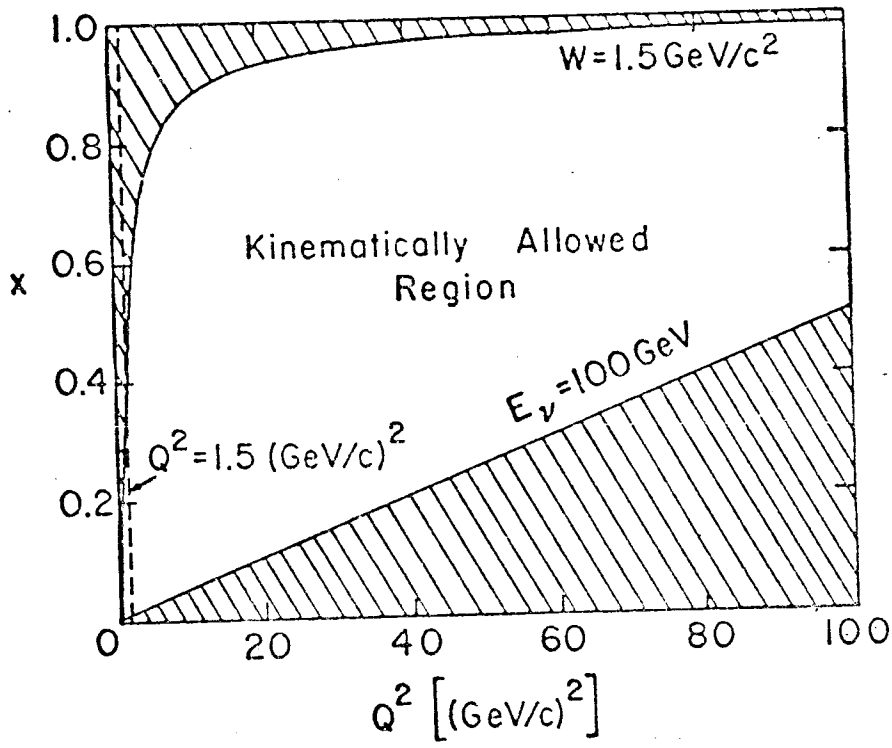

Fig. 13 Kinematically allowed region after making Q^2, W cuts. A line is drawn at E_ν=100 GeV since few neutrino events have a higher energy.

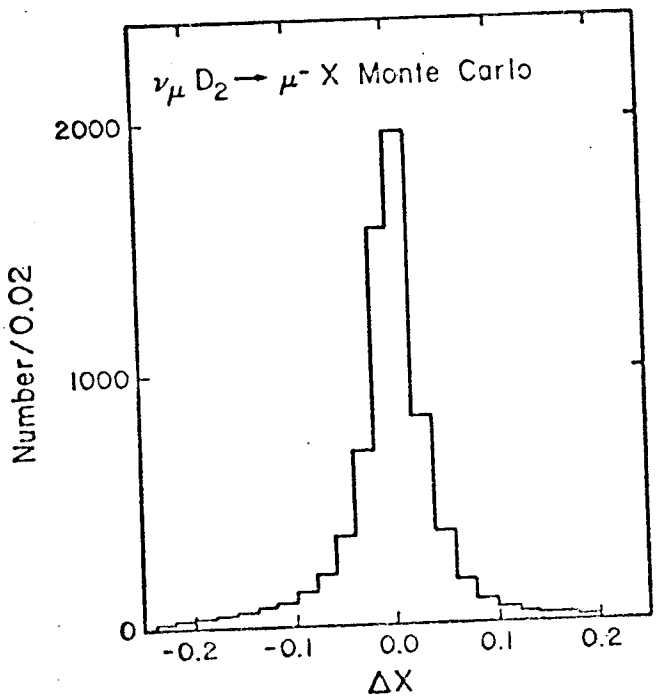

Fig. 14 Delta x, error in estimatation of Bjorken x, from Monte Carlo.

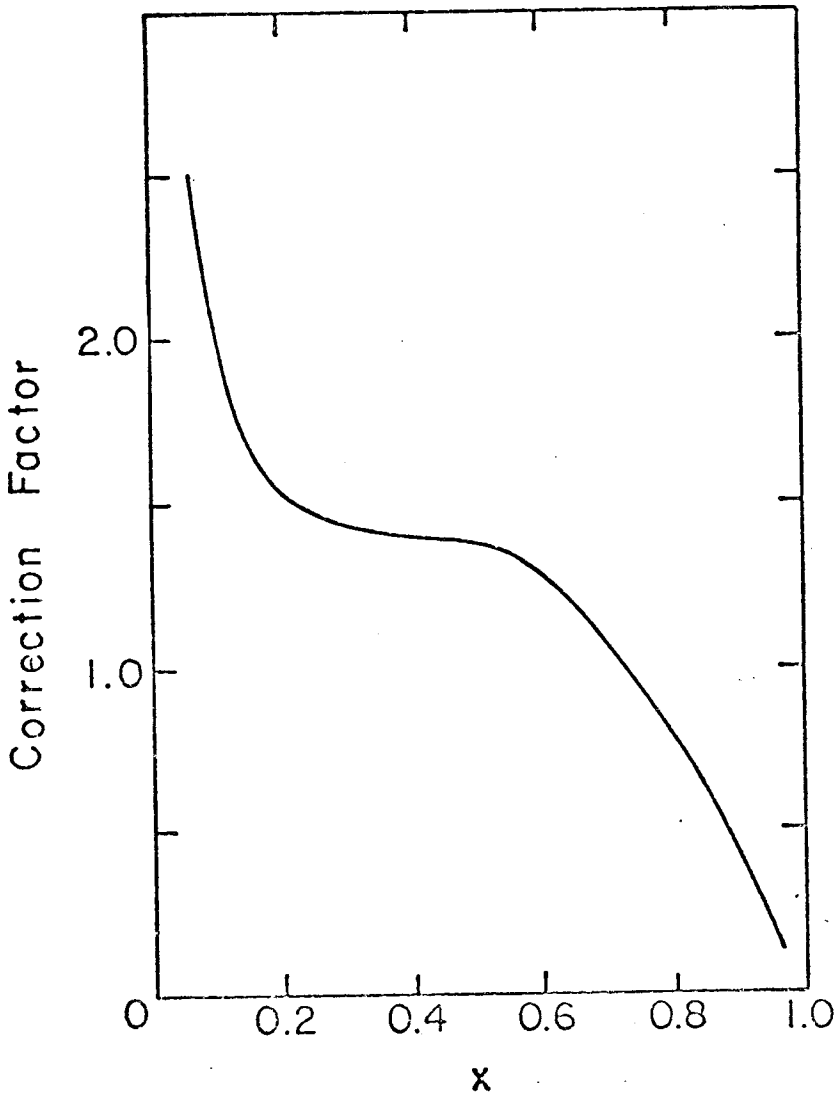

Fig. 15 Differential correction curve for Bjorken x distribution. This particular curve is for the set of cuts: $E_{vis}>10$ GeV, $P_{tr}>1$ GeV/c, $Q^2>1.5$ $(GeV/c)^2$, $W>1.5$ GeV/c^2, $x>0.05$, $y<0.90$.

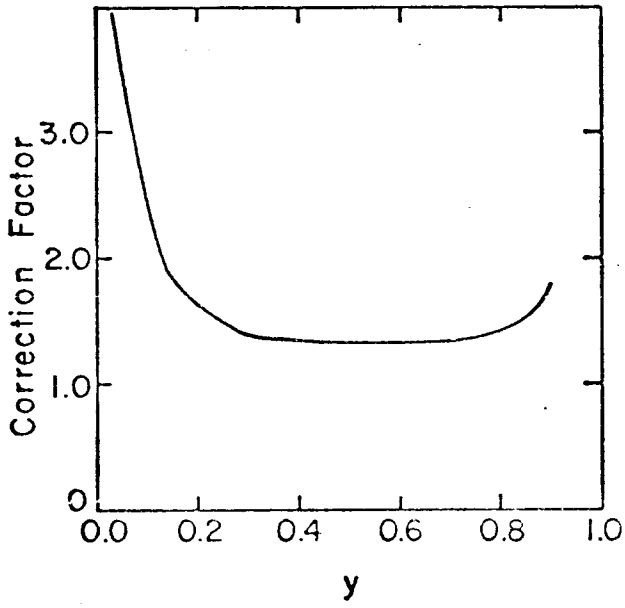

Fig. 16 Differential correction curve for the Bjorken y distribution. This curve is for the same cuts as the previous figure.

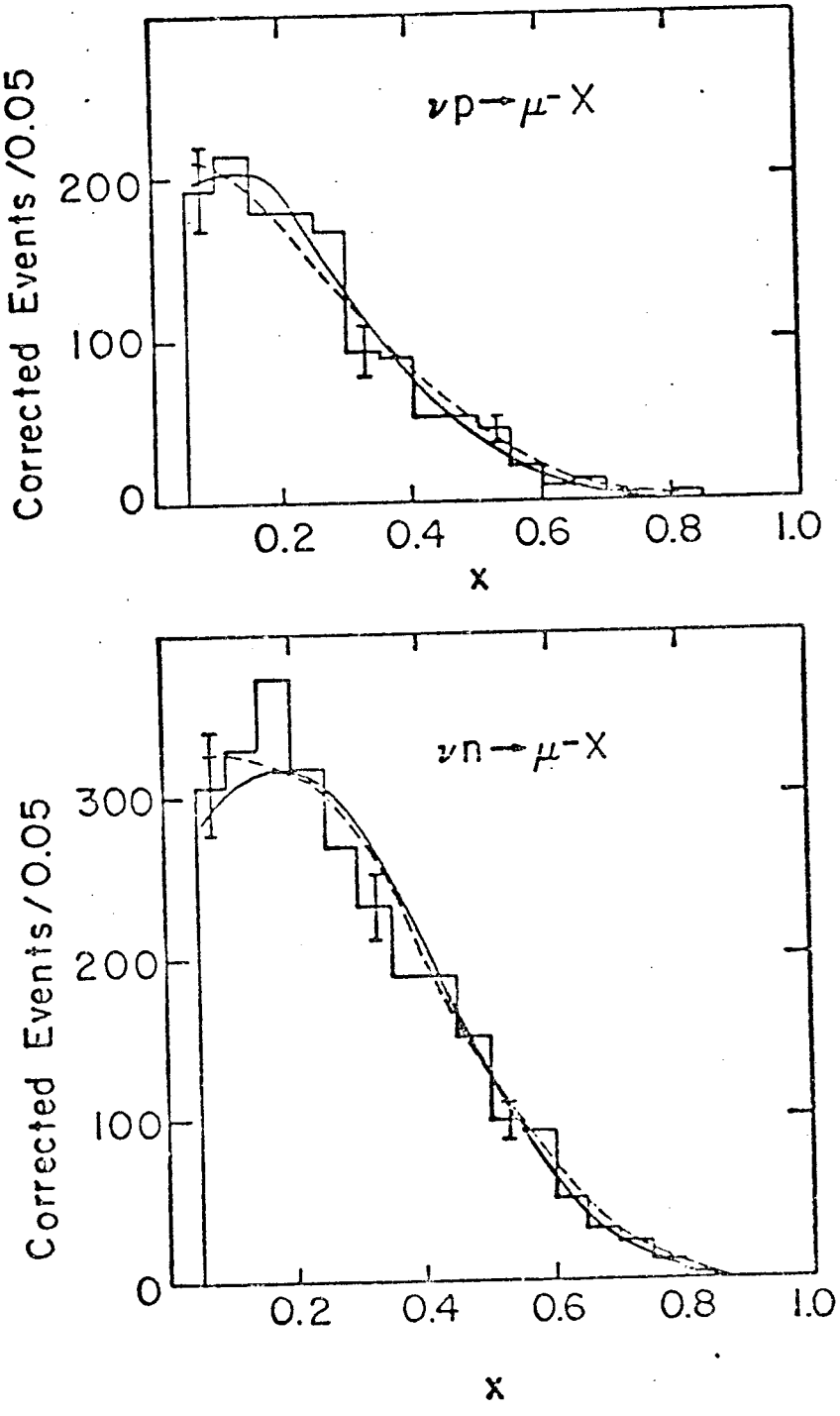

Fig. 17 Corrected distributions in the Bjorken x variable for deep inelastic neutrino interactions. The data is subject to the cuts of Figure 15. The curves are predictions from the quark parton model. The solid curve comes from using the Field-Feynman parameterizations, the dashed curve comes from using Buras-Gaemers.

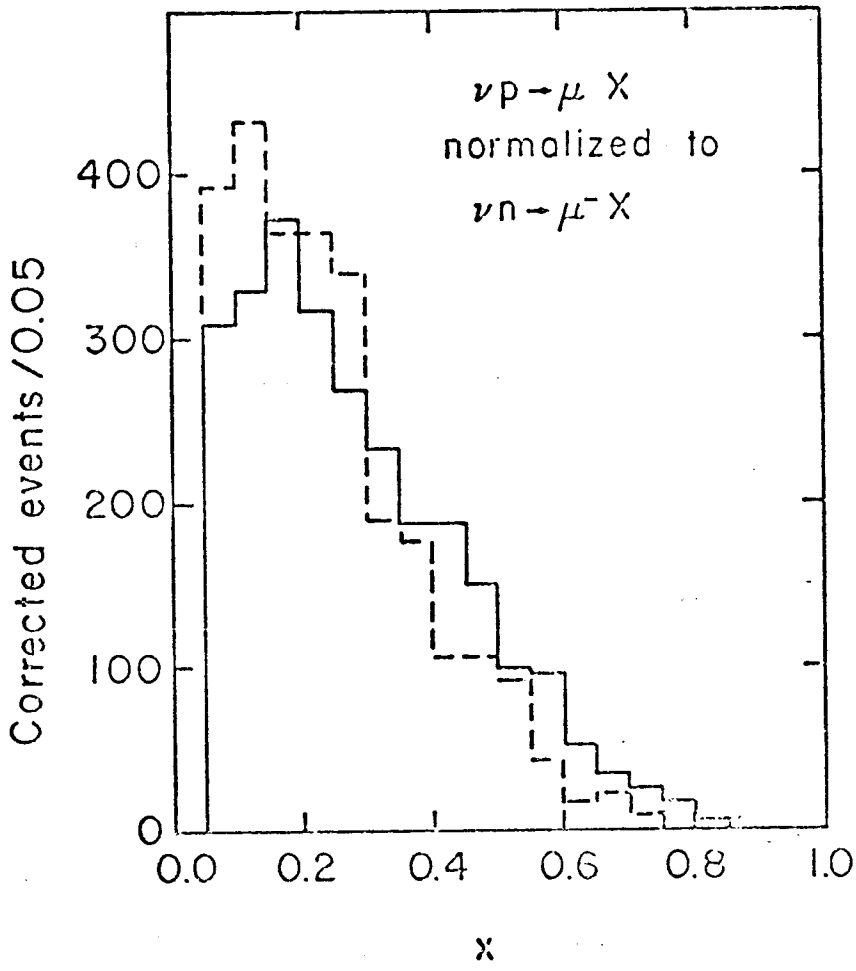

Fig. 18 Corrected distributions in x. The data of the previous figure are replotted to show that the neutron (solid line) distribution is wider than the proton (dashed line) distribution.

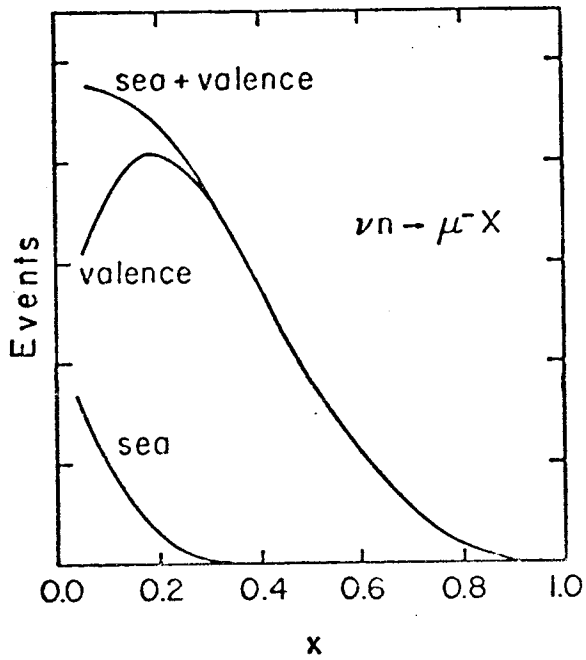

Fig. 19 The Monte Carlo prediction of Figure 17 (Buras + Gaemers), is reploted to show sea and valence quark contributions separately.

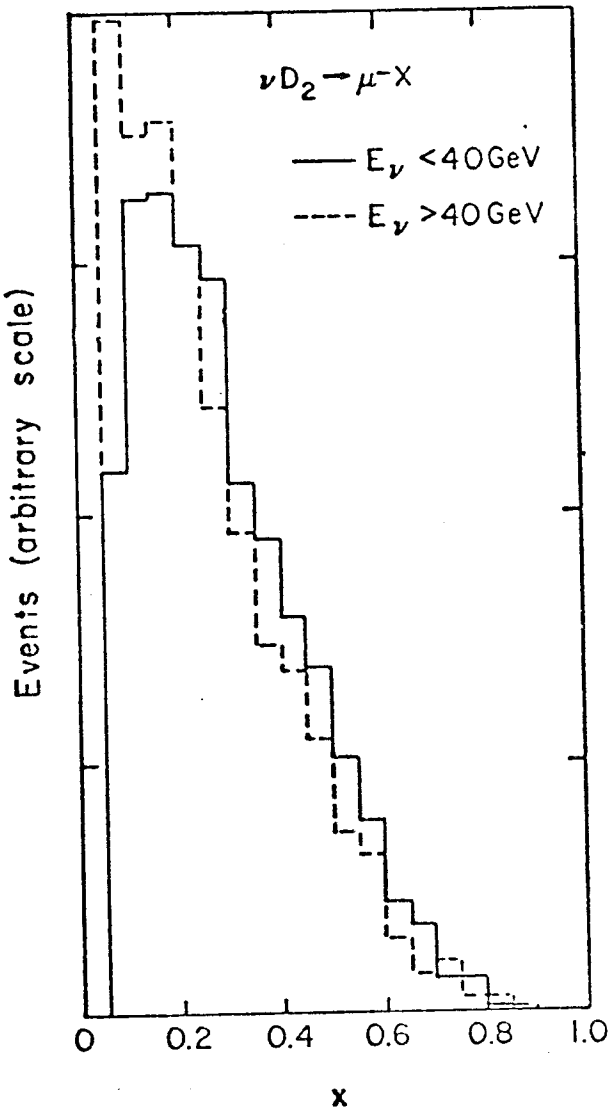

Fig. 20 Corrected x distributions for two different neutrino energy ranges. The data is subject to the cuts of Figure 15.

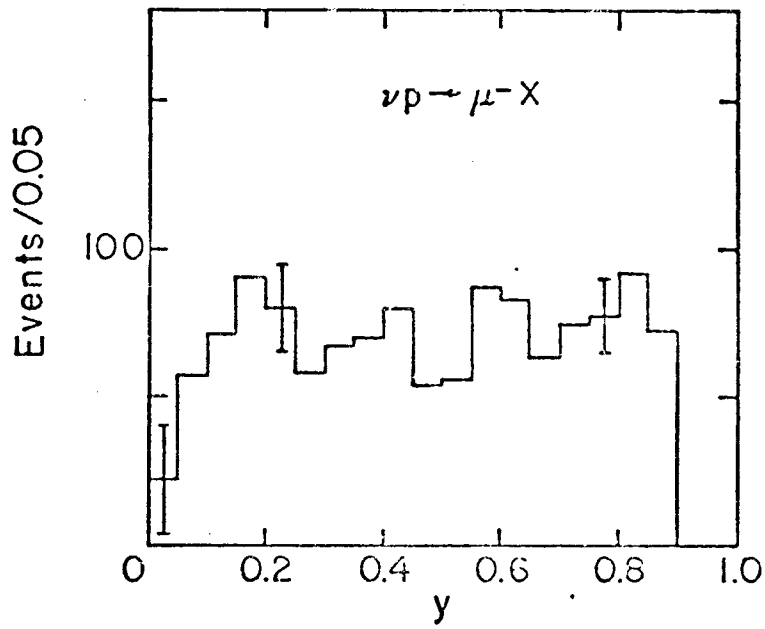

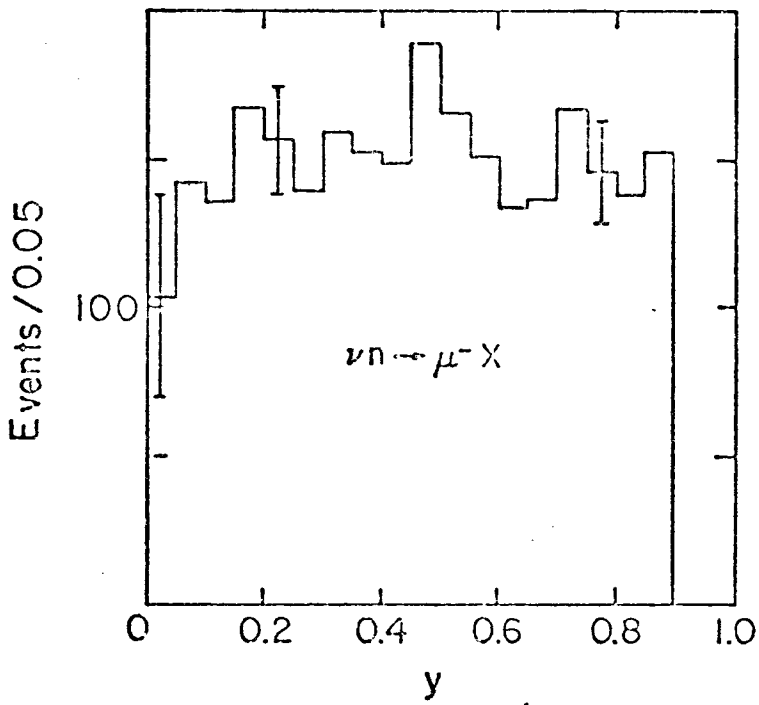

Fig. 21 Corrected distributions in the Bjorken y variable for deep inelastic neutrino interactions. The data is subject to the cuts of Figure 15.

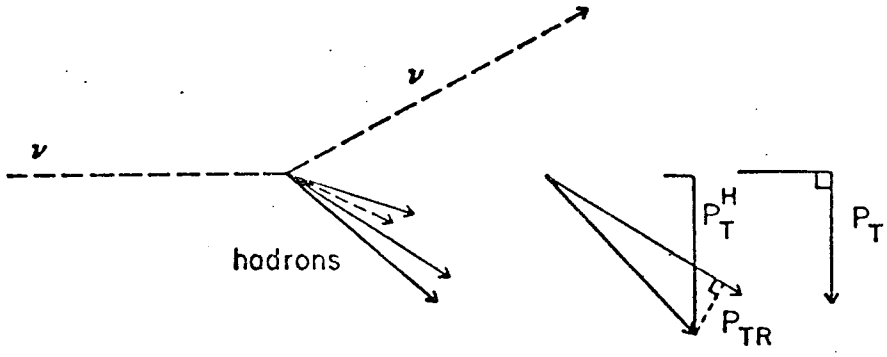

a) neutral current

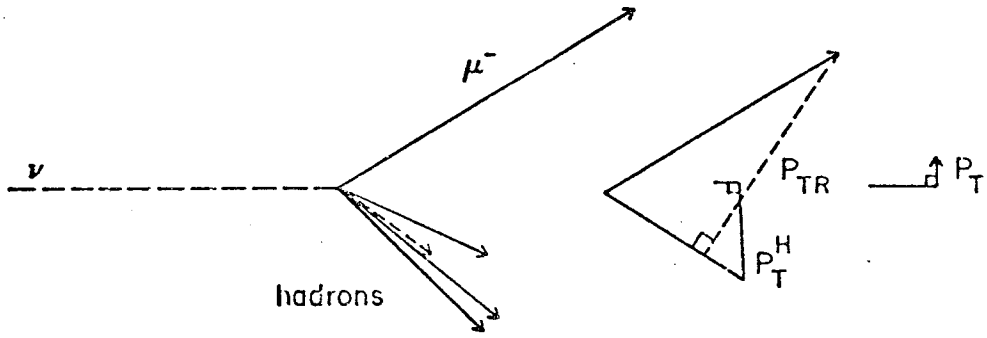

b) charged current

Fig. 22 Transverse momentum of the visible hadrons (P_t^H) in typical neutral and charged current events. P_{tr} can be seen to be typically large in charged current events and much smaller in neutral current events. The total visible momentum P_t transverse to the neutrino direction is also shown.

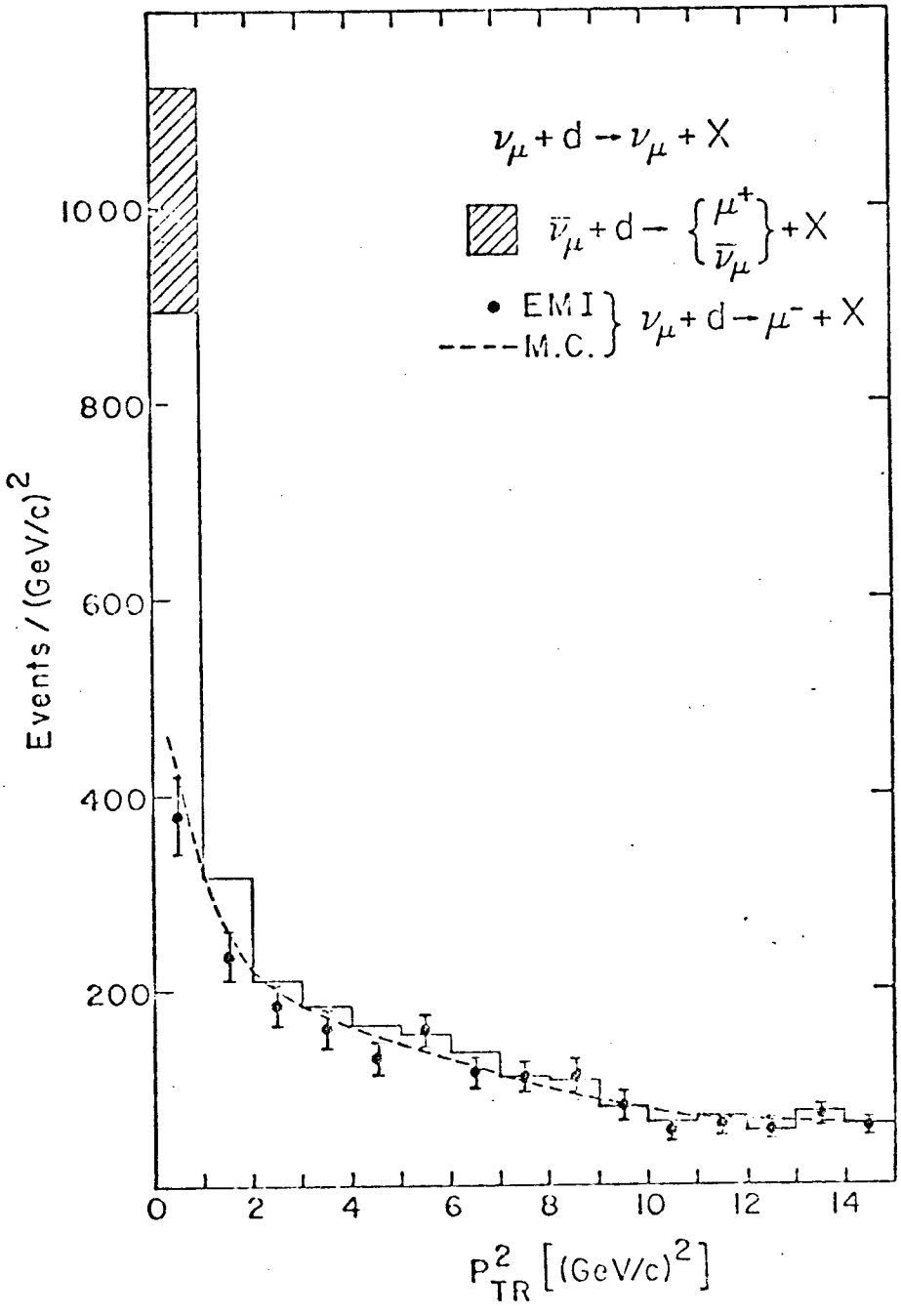

Fig. 23 P_{tr} distribution for deuterium target events. Only the cuts of Chapter 2 are applied to the data.

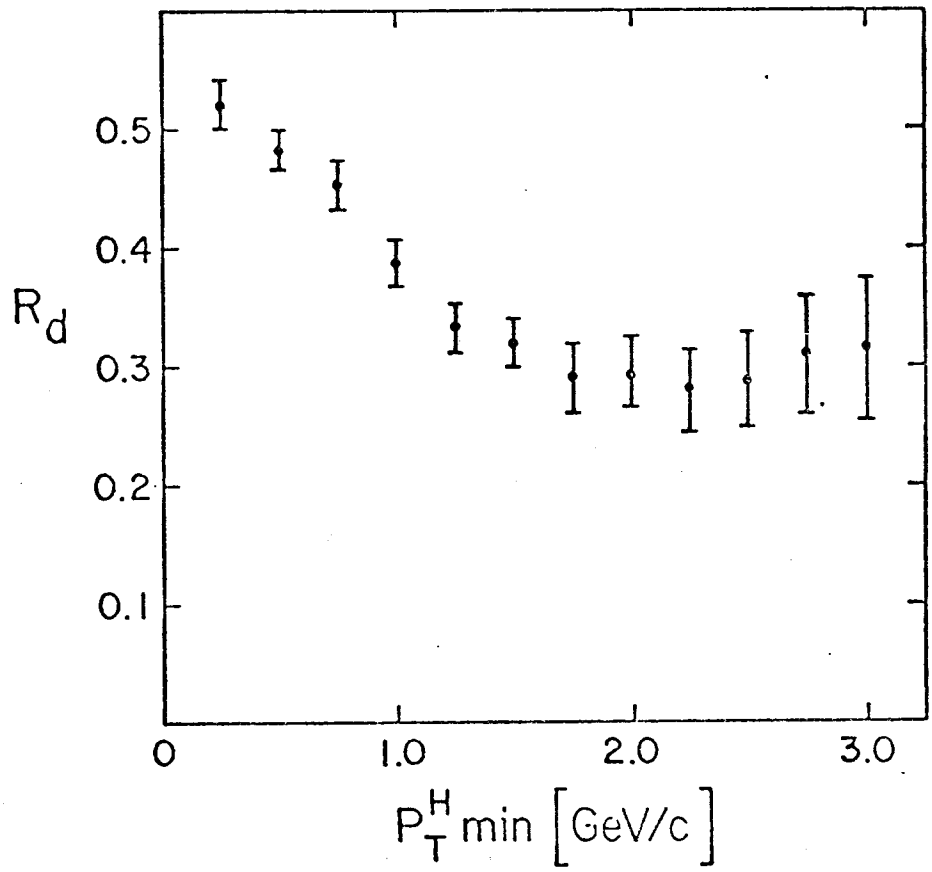

Fig. 24 Apparent neutral to charged current cross section ratios as a function of P_τ^H cut for deuterium target events.

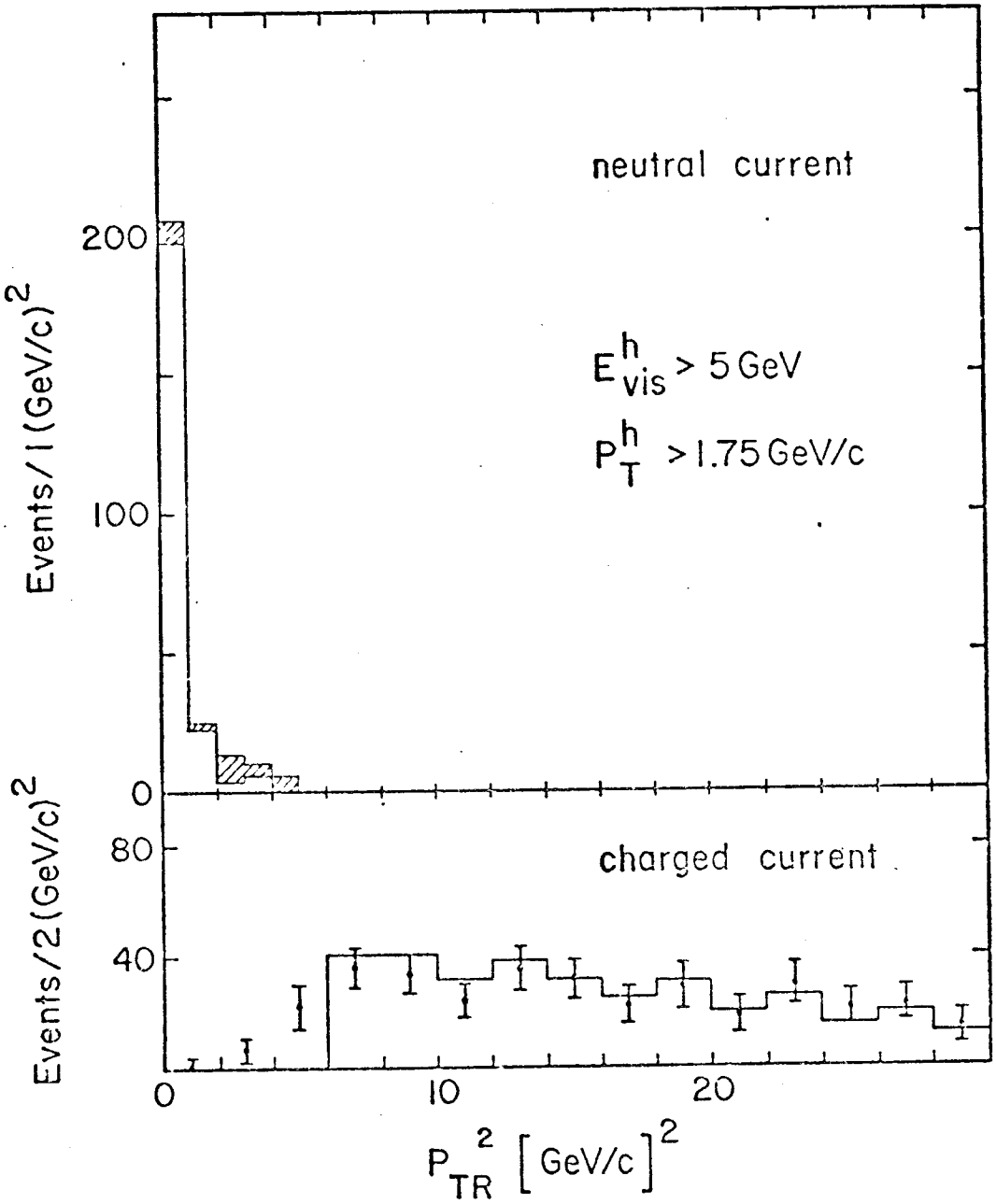

Fig. 25 P_{tr} distribution after making P_t^H cut for deuterium target events.

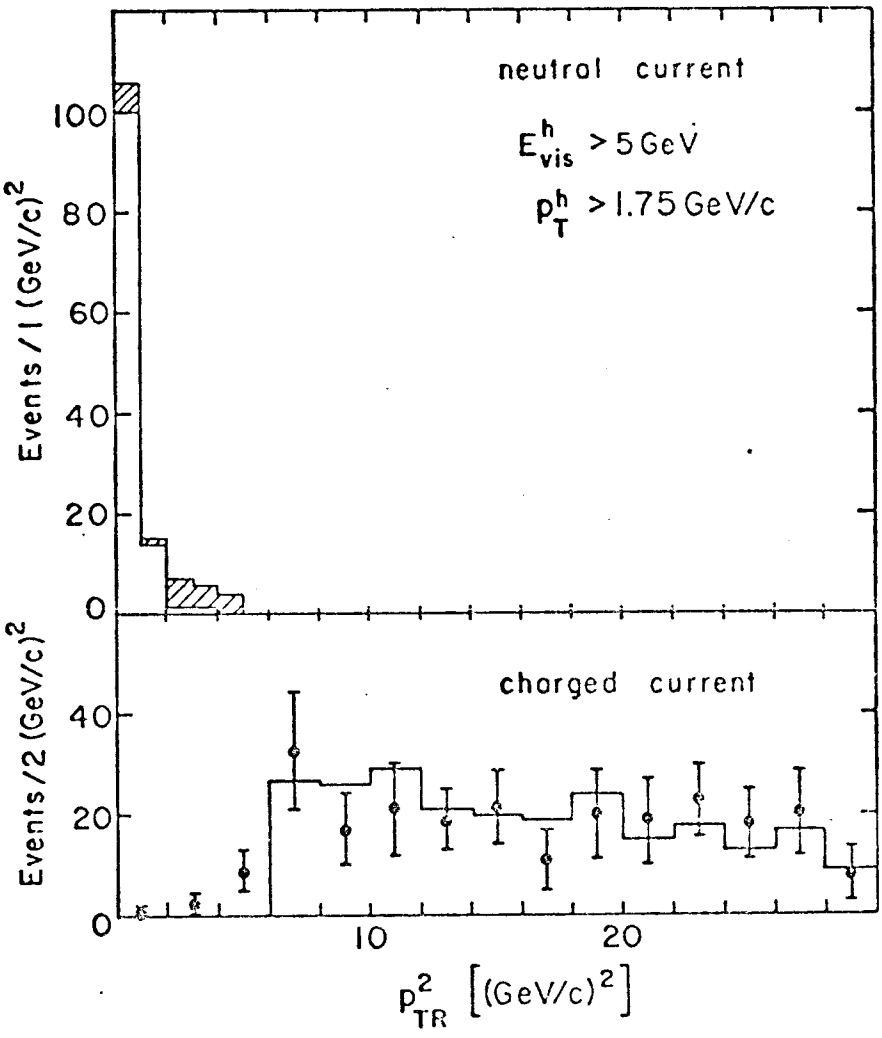

Fig. 26 P_{tr} distribution after making P_t^{H} cut for neutron target events.

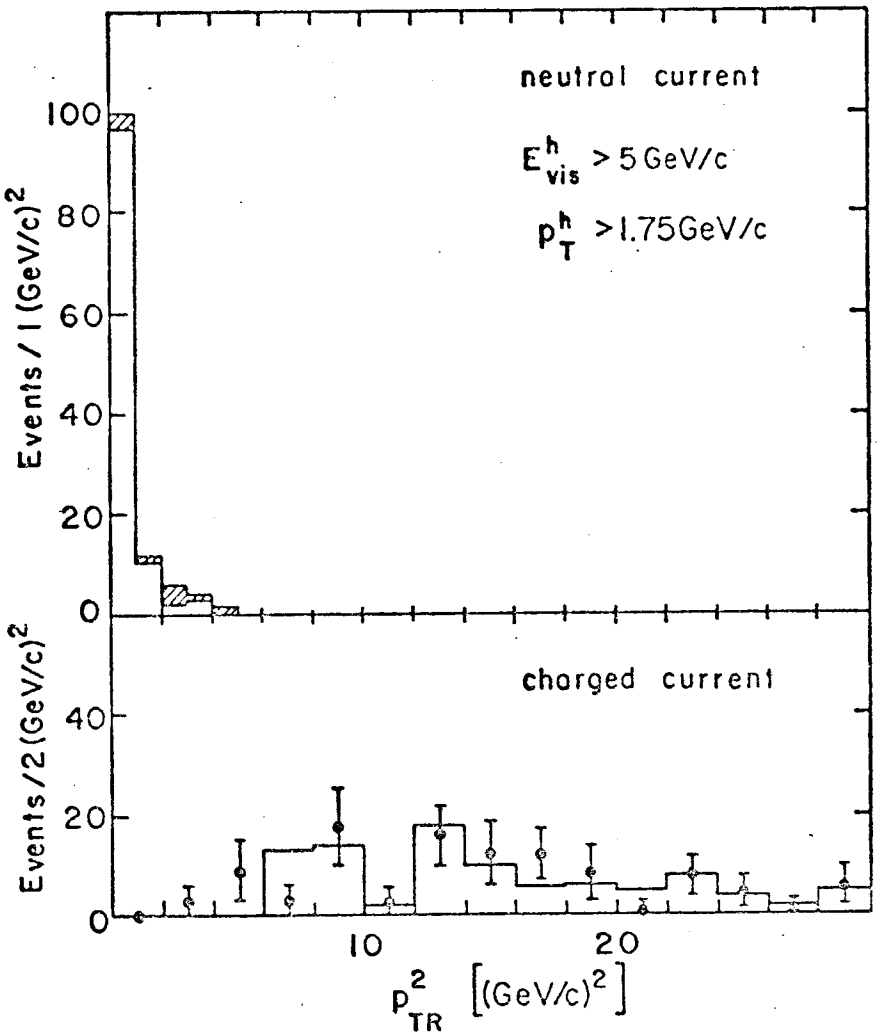

Fig. 27 P_{tr} distribution after making $P_t^{\parallel}$ cut for proton target events.

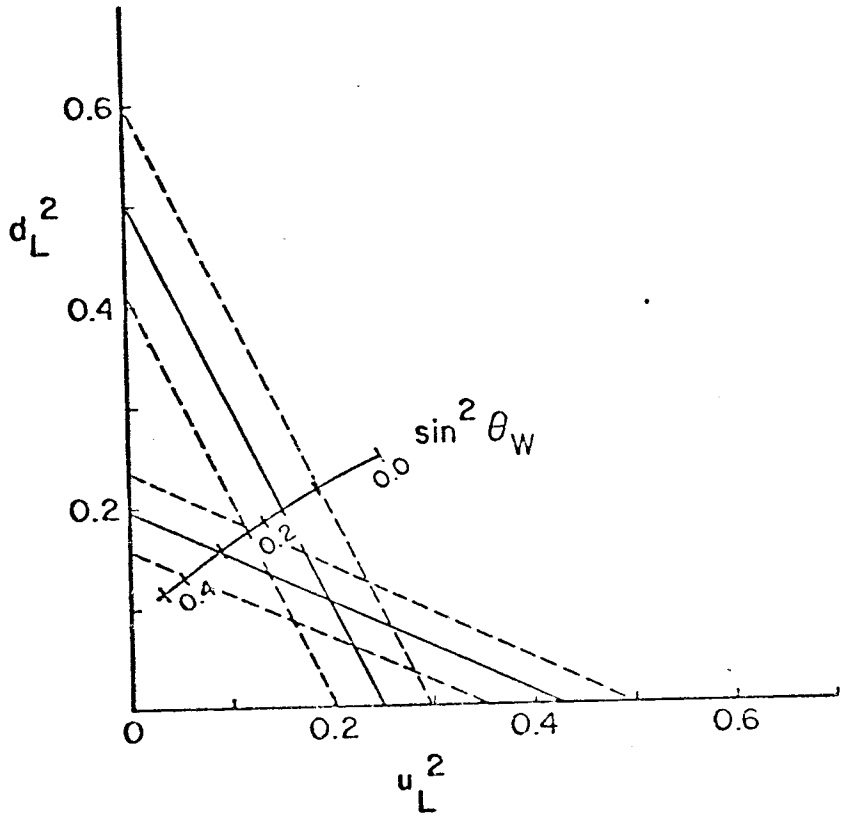

Fig. 28 u_L^2 vs d_L^2 as determined in this experiment. Also shown in the prediction of the Weinberg-Salam model.

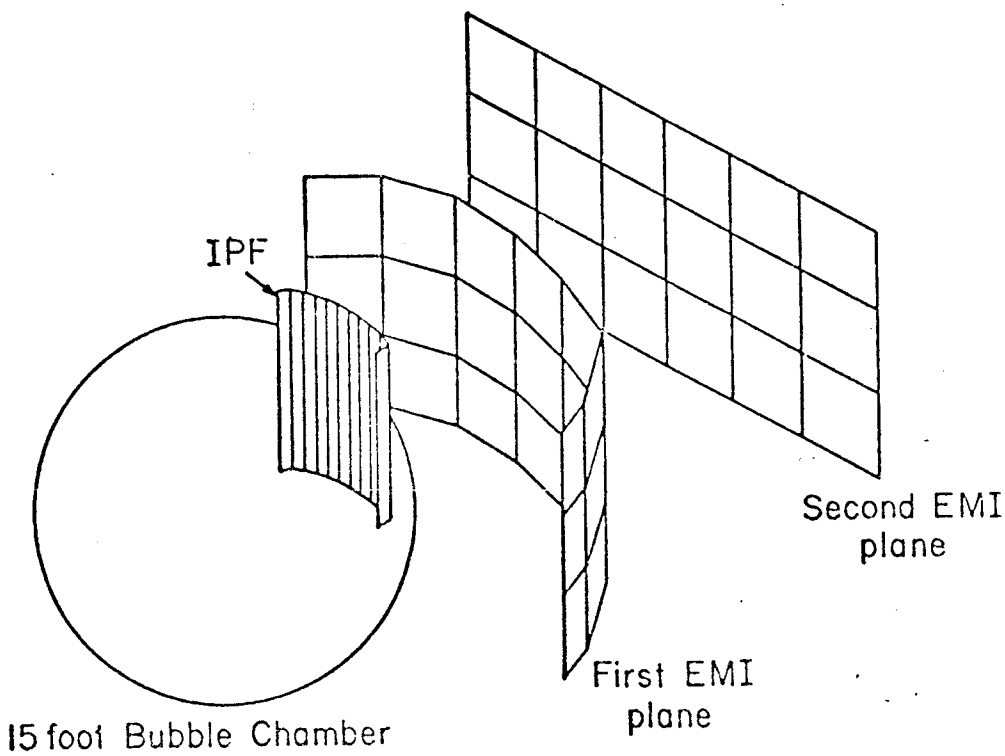

Fig. 29 Bubble chamber and external muon identifier.

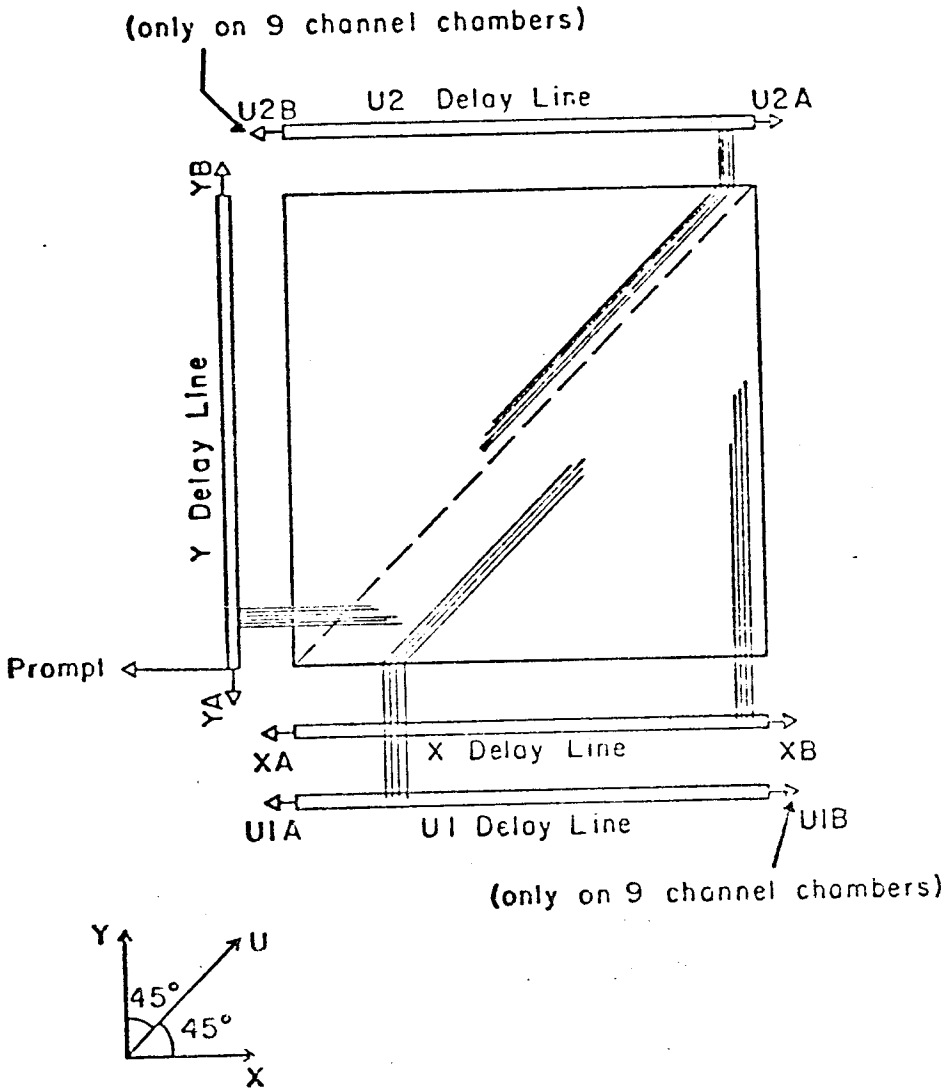

Fig. 30 Sketch of the internal construction of a single EMI proportional wire chamber.

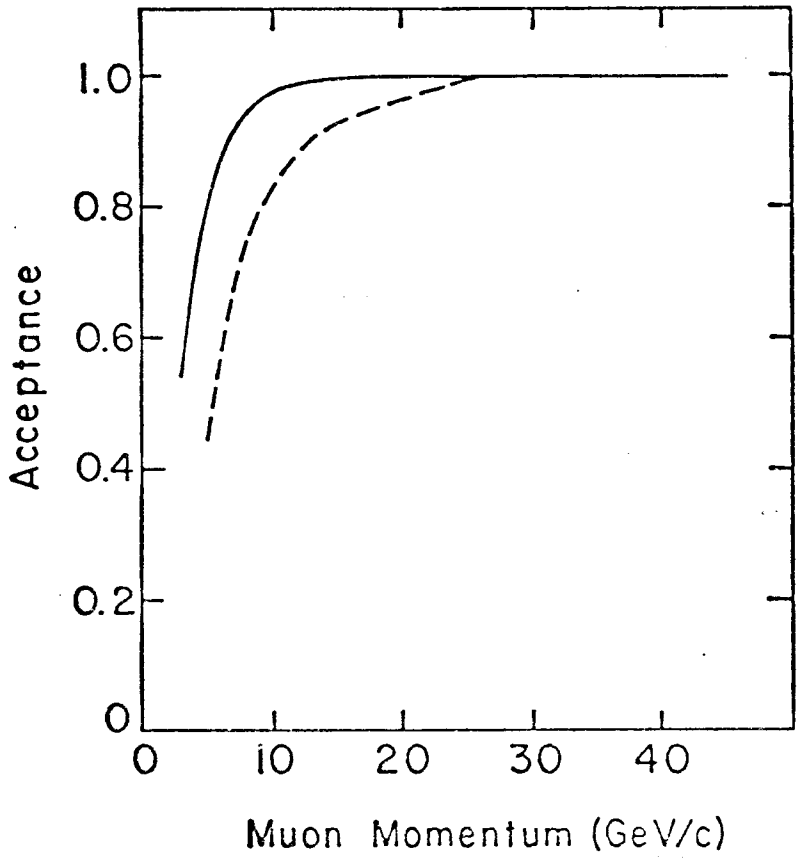

Figure 31a

Fig. 31 EMI acceptance vs a)momentum, b)Bjorken x, c)Bjorken y, d)P_{tr}. In each figure, the upper solid line is the first plane acceptance while the lower dotted line is the geometrical acceptance for the combined two planes.

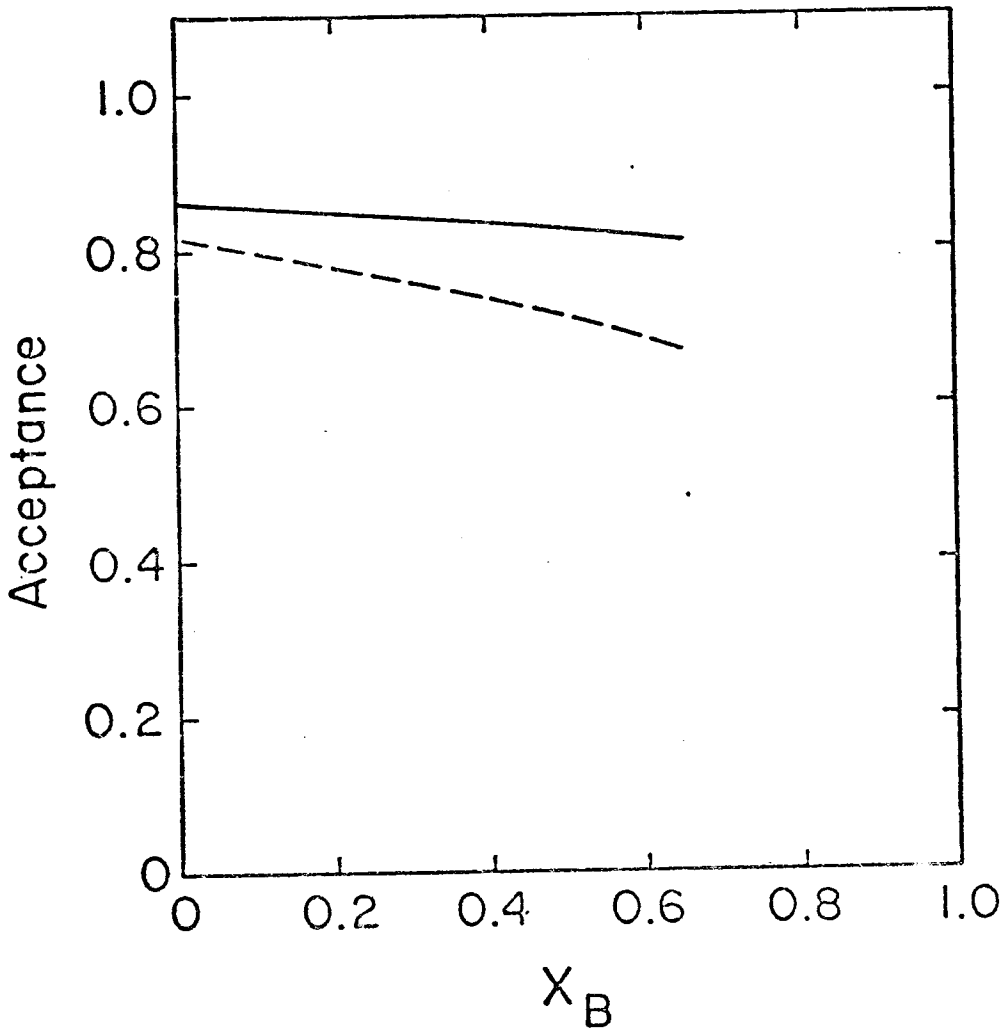

Figure 31b

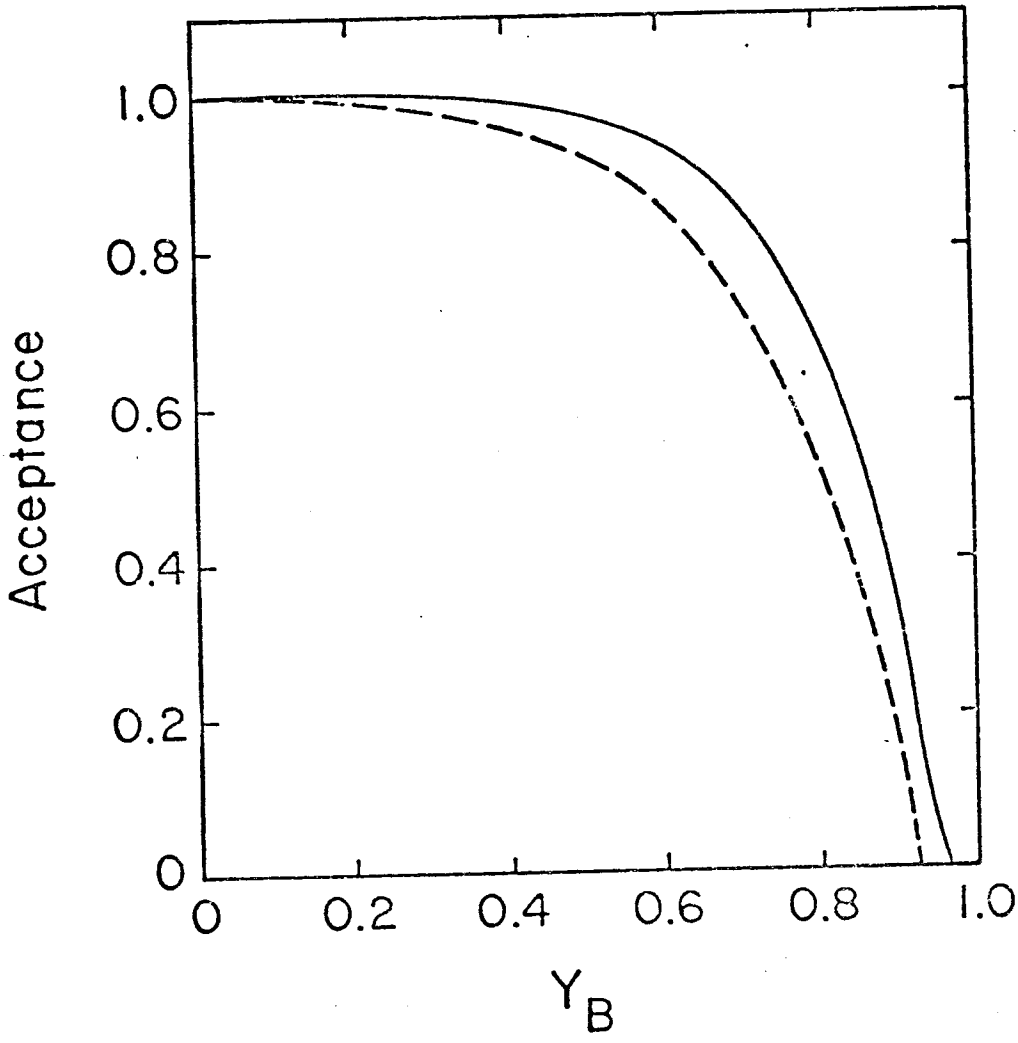

Figure 31c

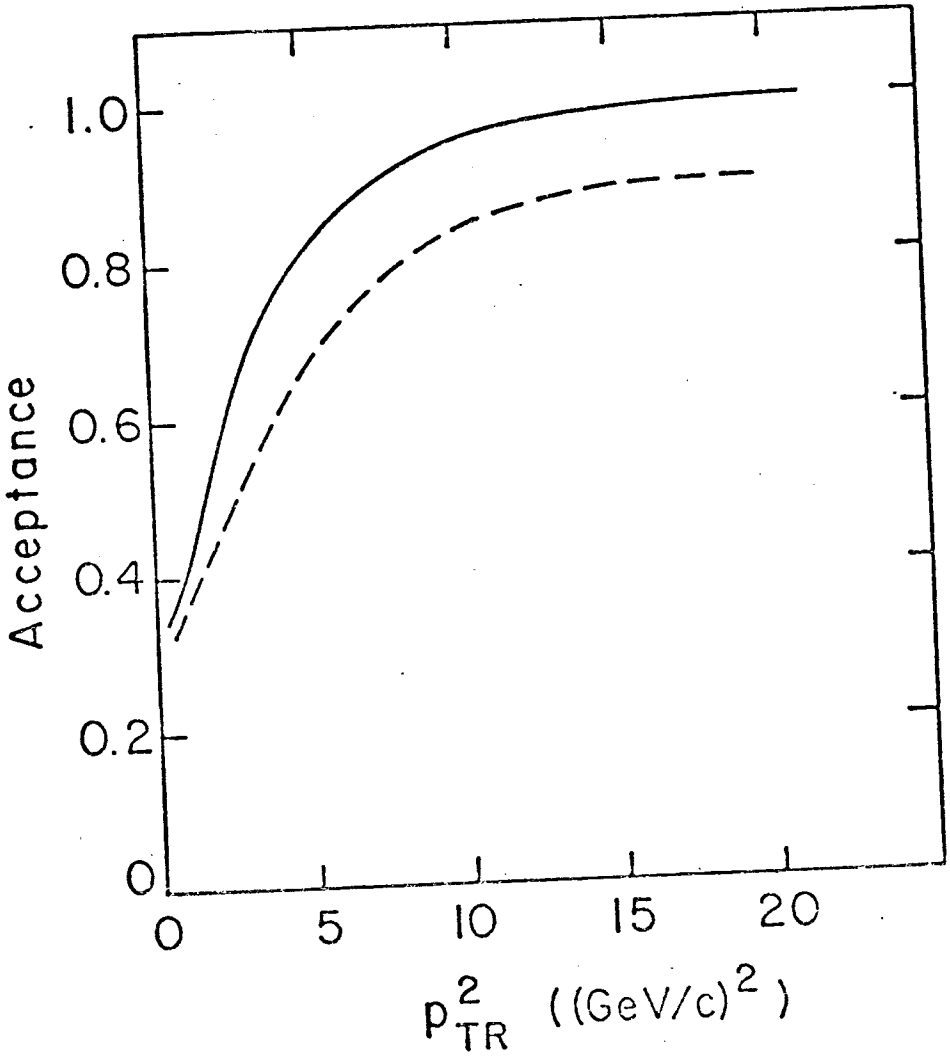

Figure 31d

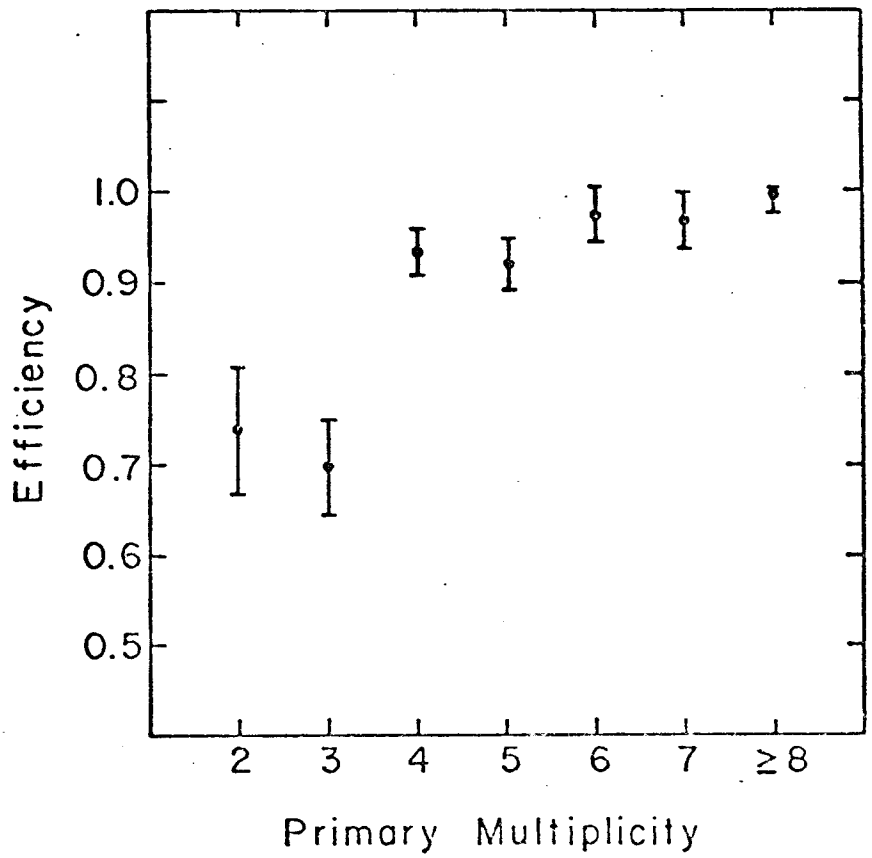

Fig. 32 IPF efficiency versus charged multiplicity of the charged current event.

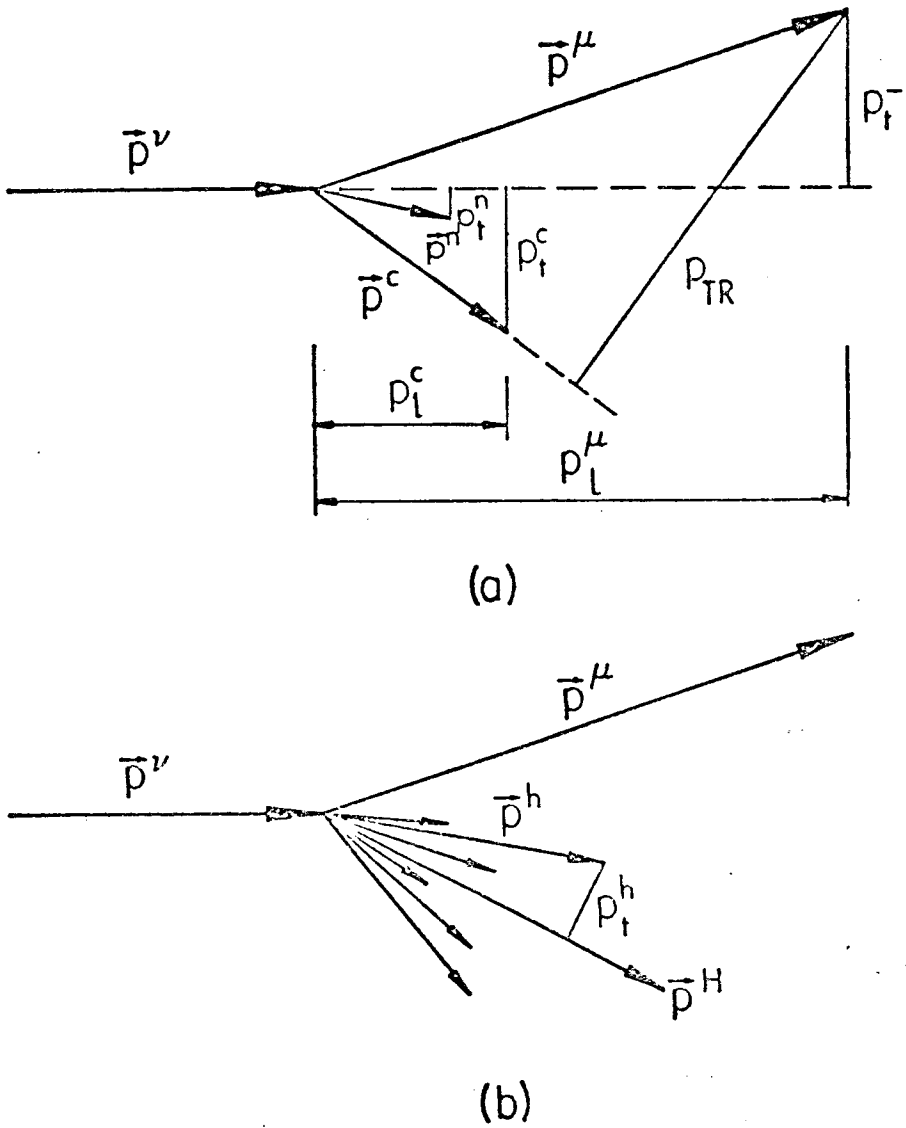

Fig. 33 Definition of variables used in neutrino energy estimate.

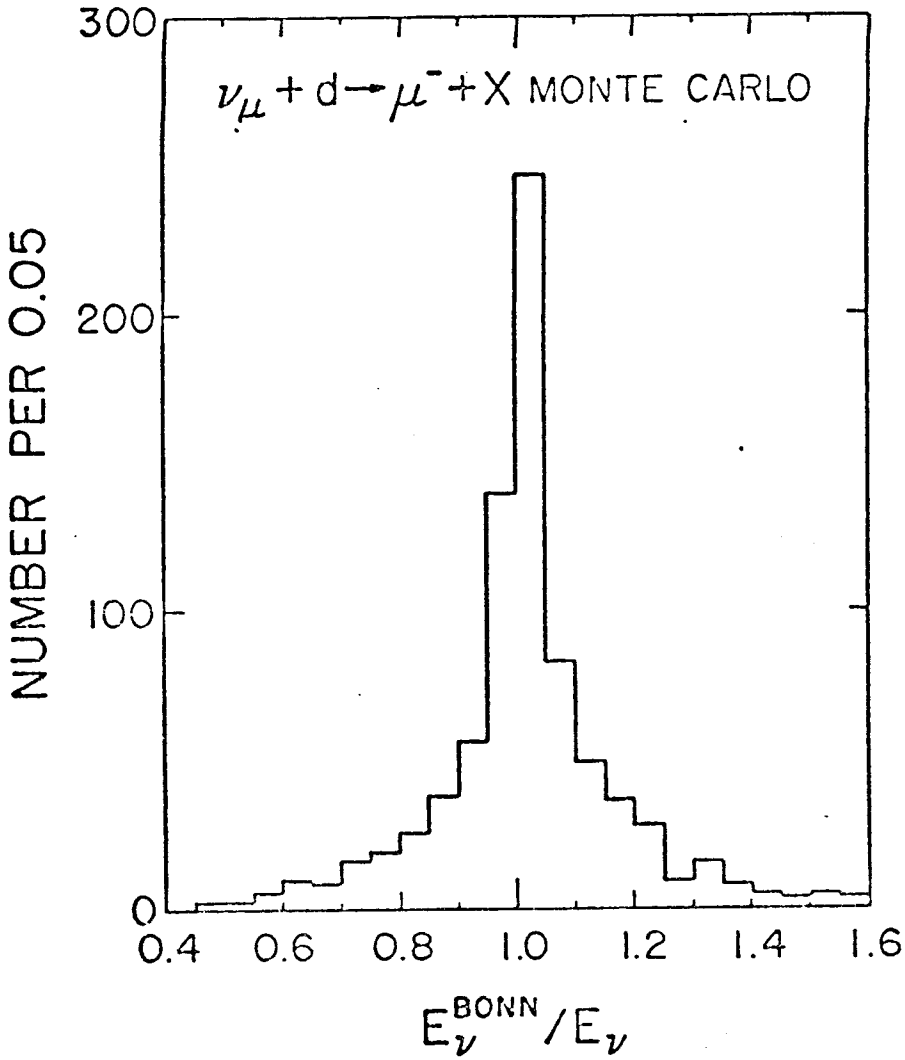

Fig. 34 Resolution in neutrino energy, E_ν(calc.)/E_ν(gen.).

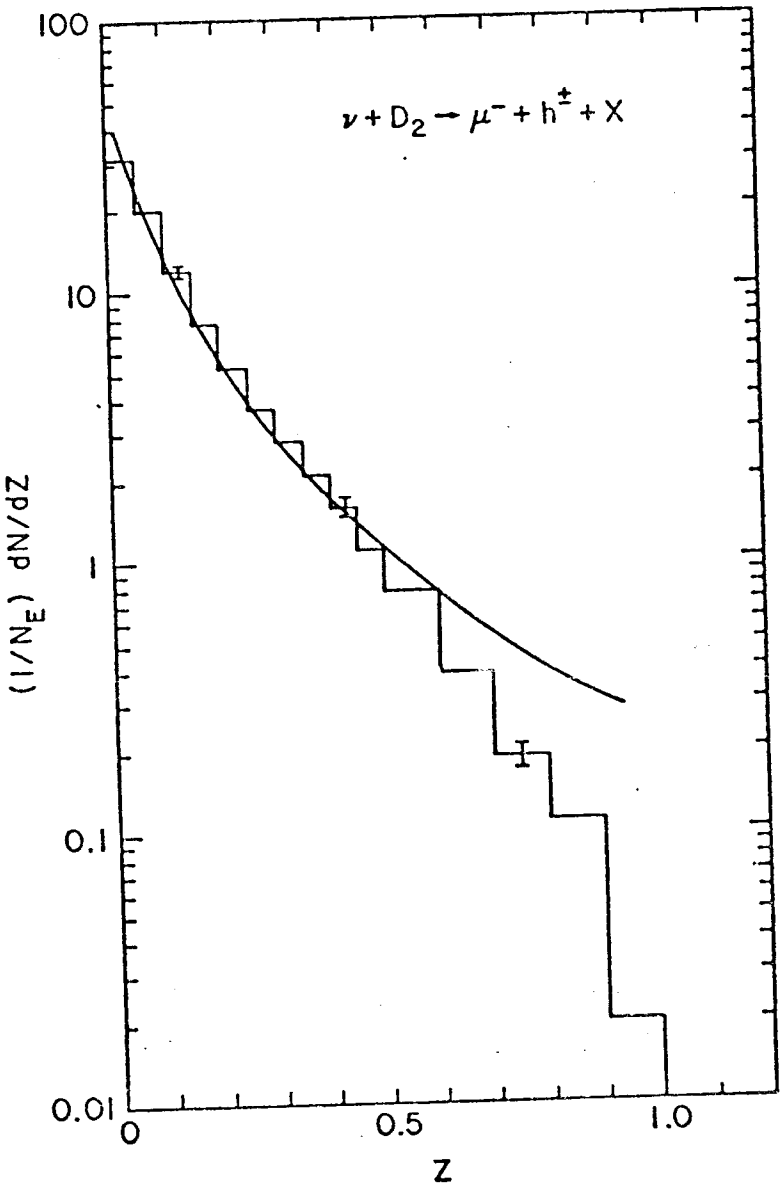

Fig. 35 Distribution of longitudinal momentum of the outgoing hadrons in charged current interactions. The variable z= (energy of individual hadron)/(total hadronic energy) is used. The solid curve represents the z distribution predicted by the Monte Carlo.

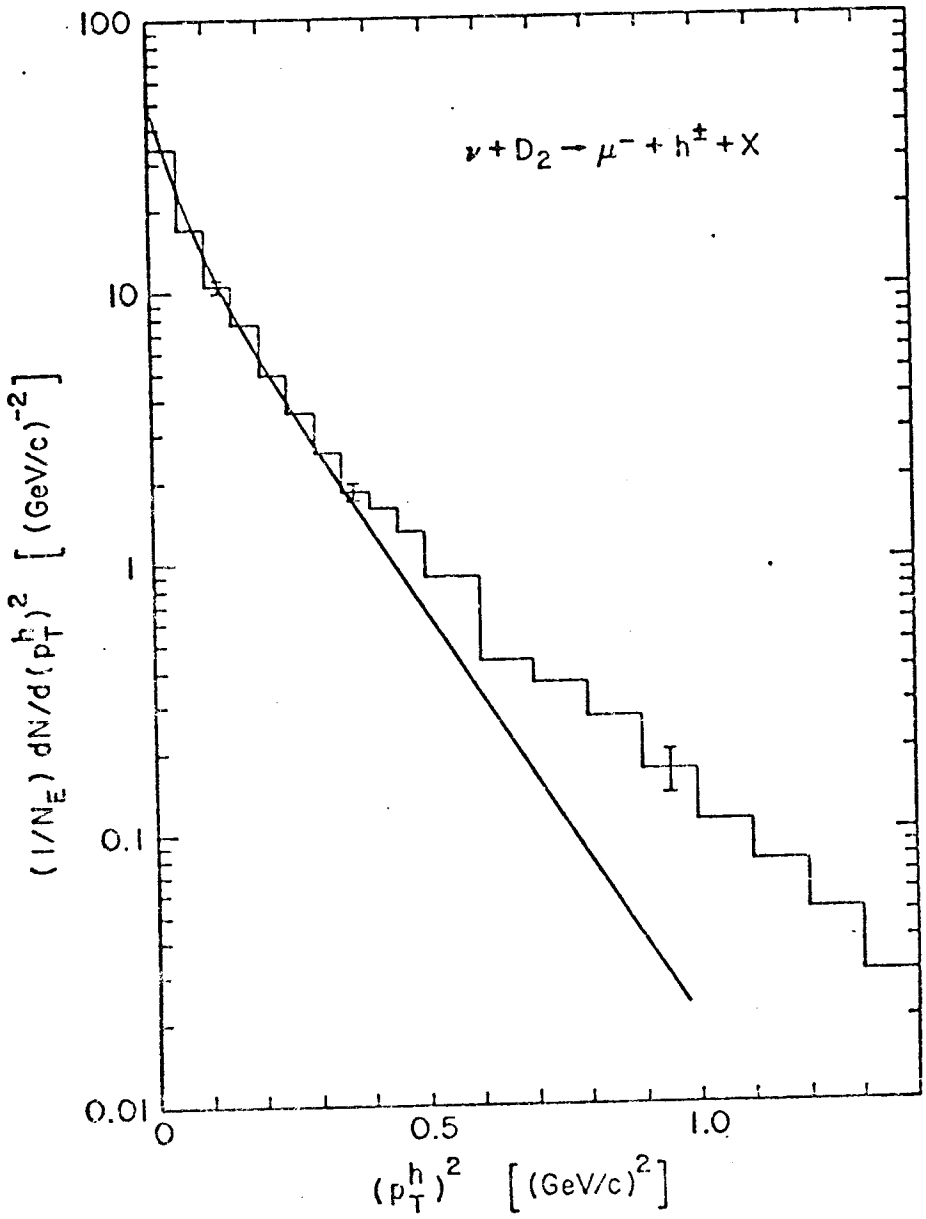

Fig. 35 Distribution of transverse momentum of individual hadrons with respect to the total hadronic direction for charged current interactions. The solid curve is the distribution generated by the Monte Carlo program.